To the Graduate Council:

I am submitting herewith a dissertation written by Jaime R. Taylor entitled "**The Electromagnetic Armature Force in Railguns**." I have examined the final copy of this dissertation for the form and content and recommend that it be accepted in partial fulfillment of the requirements for the degree of **Doctor of Philosophy**, with a major in **Engineering Science**.

Dennis Keefer

Dennis R. Keefer, Major Professor

We have read this dissertation
and recommend its acceptance:

Roger Crawford

L Montgomery Smith

R. Engels

Accepted for the Council:

Cwminkel

Associate Vice Chancellor
and Dean of The Graduate School

THE ELECTROMAGNETIC ARMATURE FORCE IN RAILGUNS

A Dissertation

Presented for the

Doctor of Philosophy

Degree

The University of Tennessee, Knoxville

Jaime R. Taylor

May 1995

To my Wife

ACKNOWLEDGEMENTS

I would like to express my sincere appreciation to several individuals without whom this dissertation would not have been possible. Thanks is given to Dr. Dennis Keefer and Dr. Roger Crawford for their continued support and overall guidance for the past five years. Special thanks is given to Dr. Keefer for his insights and advice which made this work possible. I would also like to thank him for having me as a student, it has been both a pleasure and a honor.

Thanks is given to Dr. Monty Smith for the many hours he spent listening to the ideas of Dr. Keefer and myself, pointing out errors and helping to formulate the problem. I would also like to thank Dr. Remi Engels for agreeing to review this work, and all the members of the committee for their time and effort in assuring that this document met their high academic standards.

I would like to acknowledge the efforts of and to thank Dimitri Kondrashov and Paul Leonard for their contributions to the numerical aspects of this dissertation. Their patience in listening to and answering my sometimes trivial numerical questions has been appreciated. I would also like to thank Newt Wright and Bruce Hill for their work on the UTSI railgun experiments.

I would like to thank my parents, brothers and sister for their continued support of my education over the years. A special thanks is given to the Ropers for the uncountable things they have done for me and my family during the course of this dissertation. I would especially like to thank my wife, Stacy, for her love and understanding. Words alone cannot express my appreciation for the sacrifices she has made to help me with this work.

The research reported in this dissertation was funded by SDIO/IST and managed by U.S. Army/SDC under Grant No. DASG60-90-C-0015.

ABSTRACT

Plasma armature transaugmented and muzzle-fed railgun experiments were performed in the UTSI 2.4 m, 1 cm bore diameter railgun. These experiments were evaluated with a performance model that included the simple electromagnetic force equation for the particular railgun, viscous and ablation armature drag, and the compression of bore gas ahead of the projectile. This evaluation revealed that at least one of the force or drag models was incorrect. The simple electromagnetic force equations for a "real railgun", one with a finite rail thickness, were derived using the conservation of power at the breech. Strain energy due to the transverse component of current density in the rails and losses from eddy current generation from field diffusion and armature motion were neglected in this derivation.

Three-dimensional (3-D) electromagnetic simulations were performed on a generic square bore railgun configuration with the codes MEGA and MAP3 to determine the seriousness of the losses not included in the derivation. These simulations showed that only a fraction of the force predicted by the simple electromagnetic force model was exerted on the armature. For example, a force of 510 N was predicted for the muzzle-fed railgun at steady-state while a calculated armature force of -170 N was found from the 3-D simulation with a stationary armature. This showed that the simple electromagnetic force model could not be used to predict railgun performance for the muzzle-fed railgun.

A modification to the simple electromagnetic force equation is proposed,

$$F = \pm \frac{1}{2} \alpha L' I_1^2 + \beta M' I_1 I_2 ,$$

where the positive sign gives the force for the transaugmented railgun and the negative sign gives the force for the muzzle-fed railgun. The parameters α and β represent the fraction of force exerted on the armature from the inner and outer rails respectively. 3-D simulations are required to find values for α and β.

Evaluation of the transaugmented and muzzle-fed railgun experiments using the modified electromagnetic force equation in the performance model showed that one of the drag models was still in error. Further evaluation of the experiments, and published results of 3-D MHD simulations suggested two possibilities that could explain the further deficit in performance. The value of C_f (the viscous drag coefficient found from turbulent pipe flow) could be in error by an order of magnitude due to the increased velocity gradient at the rail surface produced by the **J** x **B** forces in the plasma armature. Another possibility is that material trapped in the "cold" region between the armature and projectile (which was not included in the performance model) reached a mass an order of magnitude greater than the mass of the armature itself.

TABLE OF CONTENTS

CHAPTER **PAGE**

I. INTRODUCTION 1

1.1. Plasma Armature Drag Mechanisms 2

1.2. Experimental Attempts to Improve Railgun Performance 6

1.3. Non-U.S. Plasma Armature Studies 9

1.4. Overview of Dissertation 12

II. WHY QUESTION THE SIMPLE ELECTROMAGNETIC FORCE MODEL? . 15

2.1. The UTSI Transaugmented Railgun Experiments 16

2.1.1. Experimental Setup 16

2.1.2. Experimental Results 19

2.1.3. Conclusions from the Transaugmented Railgun Experiments . . . 23

2.2. The UTSI Muzzle-Fed Railgun Experiments 23

2.2.1. Experimental Setup 25

2.2.2. Experimental Results 26

2.2.3. Conclusions from the Muzzle-Fed Railgun Experiments 30

2.3. Derivation of the Simple Electromagnetic Force Equations 30

2.3.1. Filament Circuit Wire Method 31

2.3.2. Conservation of Power Method 32

2.3.3. Invalid Assumptions 35

III. WHAT ARE L' AND M'? 39

IV. 2-D RAILGUN SIMULATIONS 52

4.1. 2-D Railgun Investigation Using MEGA's 2D H Model 53

4.2. Evaluation of MEGA's and MAP3's 3D Formulations 61

V. INVESTIGATION OF A GENERIC SQUARE BORE RAILGUN WITH MEGA AND MAP3 71

5.1 Differences Between 2-D and 3-D Railguns. 72

5.2. Description of the 3-D Generic Square Bore Railgun 73

5.3. The 3-D Generic Square Bore Simulations 76

5.4. Conclusions 87

5.5. Modification of the Simple Electromagnetic Force Equations 96

VI. ANALYSIS OF THE UTSI RAILGUN EXPERIMENTS USING THE MODIFIED ELECTROMAGNETIC FORCE MODEL 101

6.1 Analysis of the UTSI Transaugmented Railgun Experiments 101

6.2 Analysis of the UTSI Muzzle-Fed Railgun Experiments 103

VII. SUMMARY AND CONCLUSIONS 117

7.1 Summary 117

7.2 Conclusions 122

BIBLIOGRAPHY 125

APPENDICES 130

Appendix A: Simple Electromagnetic Force Models for the Transaugmented and Muzzle-Fed Railguns 131

Appendix B: The Generic Square Bore Railgun Grid 136

VITA 139

LIST OF TABLES

TABLES		PAGE
2.1	Summary of UTSI 2.4 m transaugmented railgun experiments	20
2.2	Summary of UTSI 2.4 m muzzle-fed railgun experiments	27
5.1	Summary of electromagnetic armature and total forces	78
B.1	Nodal coordinates for generic square bore railgun	138

LIST OF FIGURES

FIGURES **PAGE**

1.1 Transaugmented railgun configuration with current paths 7

2.1 Cross section of the UTSI low inductance transaugmented railgun 17

2.2 Comparison between experimentally observed velocity increase and performance model predictions for augmented railgun 22

2.3 Muzzle-fed railgun configuration with current paths 24

2.4 Comparison of conventional and muzzle-fed railgun shots with 70 kA peak current 29

2.5 Comparison of conventional and muzzle-fed railgun shots with 100 kA peak current 29

2.6 Filament wire circuit model of railgun 32

2.7 Induced eddy currents in the yz-plane due to armature motion 37

2.8 Induced eddy currents in the xz-plane due to armature motion 37

3.1 Cross section of two rectangular conductors 43

3.2 Model used in MEGA calculations of two rectangular conductors 47

3.3 L' for two rectangular conductors as a function of the boundary location . . . 47

3.4 MEGA model of two rectangular conductors in a tube 48

3.5 Cross section of generic square bore model 50

3.6 Time dependence of L' and M' for the generic square bore model 50

3.7 Cross section of the UTSI high inductance gradient railgun 51

4.1 Diagram of a 2-D railgun 54

4.2 Equation 1.1 evaluated with time dependent value of L' 59

4.3 Equation 1.1 compared with the total force in the 2-D railgun 59

4.4 The 2-D railgun stationary armature force from the analytic expression, MEGA's **A**-ψ formulation, and MAP3's **AV** steady state formulation 67

4.5 The 2-D railgun armature force from the analytic expression, MEGA's **A**-ψ formulation, and MAP3's **AV** steady state formulation with an armature velocity of 500 m/s 69

4.6 Plot of current density for the 2-D railgun with moving armature using MEGA's 3D **A**-ψ formulation 70

4.7 Plot of current density for 2-D railgun with moving armature using MAP3's 3D AV formulation 70

5.1 Comparison of MEGA and MAP3's predictions for the armature and total railgun axial forces for a conventional railgun with a stationary armature . . . 79

5.2 Comparison of MEGA and MAP3's predictions for the armature and total railgun axial forces for a conventional railgun with an armature velocity of 500 m/s 81

5.3 Conventional railgun showing the plane for which the current densities are plotted 82

5.4 Current density for a conventional railgun at an armature velocity of 500 m/s at a time of 600 μs using a 3-D MEGA simulation 83

5.5 Current density for a conventional railgun at an armature velocity of 500 m/s at steady state using a 3-D MAP3 simulation 83

5.6 Armature and total railgun axial forces for a transaugmented railgun with a stationary armature using 3-D MEGA simulation 85

5.7 Armature and total railgun axial forces for a transaugmented railgun with an armature velocity of 1 km/s using 3-D MEGA simulation 85

5.8 Armature and total railgun axial forces for a muzzle-fed railgun with a stationary armature using 3-D MEGA simulation 86

5.9 Armature and total railgun axial forces for a muzzle-fed railgun with an armature velocity of 1 km/s using 3-D MEGA simulation 86

5.10 Current density for a muzzle-fed railgun with a stationary armature at a time of 10 μs using a 3-D MEGA simulation 89

5.11 Current density for a muzzle-fed railgun with a stationary armature at a time of 600 μs using a 3-D MEGA simulation 89

5.12 Magnetic induction at the center of the bore down the length of the gun 90

5.13 **J** x **B** at the center of the bore down the length of the armature 92

5.14 The average value of **J** x **B** in the xy-plane as a function of the axial distance in the armature 94

5.15 The axial force in the region from the rear of the armature to the axial distance in the armature indicated on the axis 94

5.16 Current density for a muzzle-fed railgun with an armature velocity of 1 km/s at time of 600 μs using a 3-D MEGA simulation 95

6.1 MEGA model of cross section of the UTSI transaugmented and muzzle-fed railgun 103

6.2 Comparison of I_1 = 70 kA transaugmented experimental series velocity profiles with that predicted by the performance model using the unmodified and modified simple electromagnetic force equation 106

6.3 Comparison of I_1 = 100 kA transaugmented experimental series velocity profiles with that predicted by the performance model using the unmodified and modified simple electromagnetic force equation 109

6.4 Modified performance model used to model shot 10/29 with increased armature mass and ablation drag coefficient 112

6.5 Experimentally observed velocity increase and performance model predictions using modified and unmodified simple electromagnetic force models 113

6.6 Comparison of experimental velocity with that predicted by the inductance gradients and MEGA for the muzzle-fed railgun 115

B.1 Cross section, xy-plane, of generic square bore model 137

B.2 Grid for generic square bore model in the yz-plane 137

I. INTRODUCTION

In 1978 Rashleigh and Marshall reported achieving a velocity of 5.9 km/s with a plasma armature railgun. They reported the "Lorentz force upon the arc" to be

$$F = \frac{1}{2} L' I^2 , \tag{1.1}$$

where L' is the inductance gradient per unit length of the rails and I is the driving current [1]. This report, along with this simple electromagnetic force model, spawned great enthusiasm for the development of a plasma armature railgun that could reach velocities of 20 to 30 km/s. Using Equation 1.1, it seemed that all that was needed was a stronger structure, longer barrels, and larger power supplies.

During more than a decade of heavily funded research, high velocity plasma armature experiments failed to achieve their predicted performance. Only three labs reported reaching velocities significantly greater than those reported by Rashleigh and Marshall in their original experiments [2].

Hawke conducted a series of experiments in a 5.2 m long railgun which showed a significant departure from the velocity predicted by Equation 1 in the experimental velocity range above 4 km/s [3]. These early experiments showed that Equation 1.1 alone could not accurately predict the experimental velocity. The discrepancy was attributed to armature fluid-dynamic loss effects [2,3,4].

1.1. Plasma Armature Drag Mechanisms.

Plasma arcs were primarily used for railgun armatures in the attempts to reach velocities in excess of 10 km/s. Associated with plasma armatures are fluid mechanical drag mechanisms. These drag mechanisms were estimated with simple lumped parameter models to explain why the expected performance was not obtained.

For turbulent flow, viscous drag on the armature is given by

$$F_v = \frac{C_f\, m_a\, v^2}{r} \ , \tag{1.2}$$

where C_f is a dimensionless friction coefficient, r is the radius of the bore, and m_a is the armature mass. The viscous drag is proportional to the velocity squared and linearly dependent on the armature mass. Assuming a constant armature density ρ, the armature mass is

$$m_a = \rho\, \pi\, r^2\, l \ , \tag{1.3}$$

where l is the armature length. Equation 1.2 in combination with Equation 1.3 shows the viscous drag's dependence on the armature length [4].

The value of C_f for plasmas in the presence of strong magnetic fields and significant wall heat transfer are unknown to an order of magnitude. Since the mass of material ablated from the insulators could be measured after each shot, an ablation drag model was developed to explain performance losses and C_f was assumed small. Ablation drag results from material that is thermally ablated from the rails and insulators, being accelerated by the armature. Material thermally ablated by the high energy flux at the surface of the armature was modeled as

$$\frac{dm_a}{dt} = \alpha_t I V_a \ , \tag{1.4}$$

where V_a is the armature voltage, I is the armature current, and α_t is the thermal ablation constant. A detailed discussion of the thermal ablation constant is found in Reference 4.

Thermal ablation predicts that most of the material ablated is from the insulators. Experiments have shown this is not the case [5]. By examination of the rails after a typical shot it was found that rail material was melted. The electrical contact at the rail and armature interface is not uniform. A fine structure of arcs exists where each arc makes contact with the rail in a small area. The arc roots dissipate more energy per unit surface area than would a uniform electrical contact, accounting for the rail melting. To account for this in Equation 1.4 the value of α_t would have to be modified.

The value of α_t used for modelling railgun performance is not the total material ablated in the railgun, but only the fraction of ablated material that gets trapped in the armature. Only a small percentage of the total material ablated may get trapped in the armature, the rest is deposited in the bore behind the primary arc. For this reason it is impossible to determine the value of α_t from the properties of the rail and insulator materials. The value of α_t is typically determined from fitting shot data of the particular railgun of interest. (i.e. the model is assumed to be correct and a value of α_t is found that makes the model work.)

The armature acceleration,

$$\frac{dv}{dt} = \left(\frac{1}{m_p + \alpha_t I V_a t}\right)\left(\frac{1}{2} L' I^2 - \alpha_t I V_a v - \frac{C_f \alpha_t I V_a t v^2}{r}\right), \tag{1.5}$$

was obtained by combining Equation 1.1 with the expressions for the viscous and ablation drag [2,3,4]. In Equation 1.5, m_p is the projectile mass and t the time. In the first set of parentheses the term in the denominator is the total mass of the projectile and armature. The second term in the second set of parentheses is the drag due to the changing mass of the armature and the third term is the viscous drag of the armature.

A parameter analysis of Equation 1.5 was given in Reference 3. The maximum velocity at which $dv/dt \rightarrow 0$ was plotted as a function of several of the parameters, each varying from a nominal case of $L' = 0.3$ μH/m, $I = 500$ kA, $\alpha_t = 10$ μg/J, $C_f = 0.001$, $v_o = 8$ km/s, $m_a = 3$ g, and $r = 12$ mm. The maximum velocity decreased from 12.7 km/s to 9.2 km/s as C_f went from 0.001 to 0.01. The maximum velocity decreased from 22.0 km/s to 12.2 km/s as α_t increased from 2 μg/J to 10 μg/J. Again, in the analysis α_t represented the ablated material that was trapped in the armature, not the total ablated material. Since C_f and α_t have not been experimentally validated, they may take on a large range of values and used to justify almost any experimental railgun data.

Secondary arc formation and primary arc separation significantly complicate the use and understanding of the simple models represented in Equation 1.5. Secondary arc formation occurs when the material behind the primary arc breaks down electrically giving the current an alternate path. The material behind the primary arc comes from ablated material that is deposited behind the primary arc and from the light gas gun injector, which was a feature of most of the early railguns.

Once a secondary arc forms, practically all the material ablated by the primary arc gets trapped in the region between the secondary and primary arc. This ablated material must be accelerated to the armature velocity reducing the accelerating force on the projectile. The ablated material also increases the armature mass which increases the viscous drag.

Primary separation occurs when the primary arc separates from the projectile. When the primary separates from the projectile, material becomes trapped in the region between the armature and the projectile causing a degradation in performance similar to that of a secondary arc. The cause of primary separation is not well understood.

When secondary arcs form or the armature separates from the projectile it becomes difficult to estimate the amount of ablated material that gets trapped in the armature. The use of the term armature here refers to all of the current-carrying bore material, primary and secondary arcs, and any material accelerated by these two arcs. This affects the estimate of both ablation drag and viscous drag.

The secondary arc causes further complications since it is not possible to determine the current split between the secondary and primary arcs. The secondary arc has a lower impedance due to the velocity skin effect [6]. The velocity skin effect is the reduction in skin depth in the region of the armature due its motion. The impedance of the secondary and primary arcs themselves also determine the current split. If it were possible to determine the current split, one would still need to model the complicated electromagnetic coupling between the secondary and primary arcs, and determine the amount of material that gets trapped and accelerated by each arc.

1.2. Experimental Attempts to Improve Railgun Performance.

To increase railgun performance Parker suggested the use of ablation resistant materials for the rails and insulators. Railguns with ablation resistant insulator materials failed to achieve their predicted performance except during periods of compact armature operation. The UTSI railgun and Thunderbolt were both used to test Boron Nitride, BN, insulators. BN has a thermal ablation threshold of 42 $MWs^{1/2}/m^2$ [7]. The conclusion from the experiments, which was unpublished, was that mechanical abrasion of the BN resulted in a significant amount of material being dumped in the bore behind the armature. Large secondaries developed early in each of the experimental shots using this insulating material.

Parker also suggested the use of novel railgun designs such as the transaugmented railgun [2,4]. The configuration of a transaugmented railgun is shown in Figure 1.1. The name transaugmentation comes from the transformer effect between the augmentation conductors and the main rails [7]. To increase the armature force in a conventional railgun (a railgun without augmentation), one must increase the current, which increases the armature voltage and power dissipation. Equation 1.4

shows that the ablated material is proportional to the armature power dissipation. A transaugmented railgun has a separately powered outer rail which makes it possible to vary the magnetic field, by adjusting the outer rail current, without varying the power dissipated in the armature. This makes it possible to increase the armature force without increasing the ablation rate.

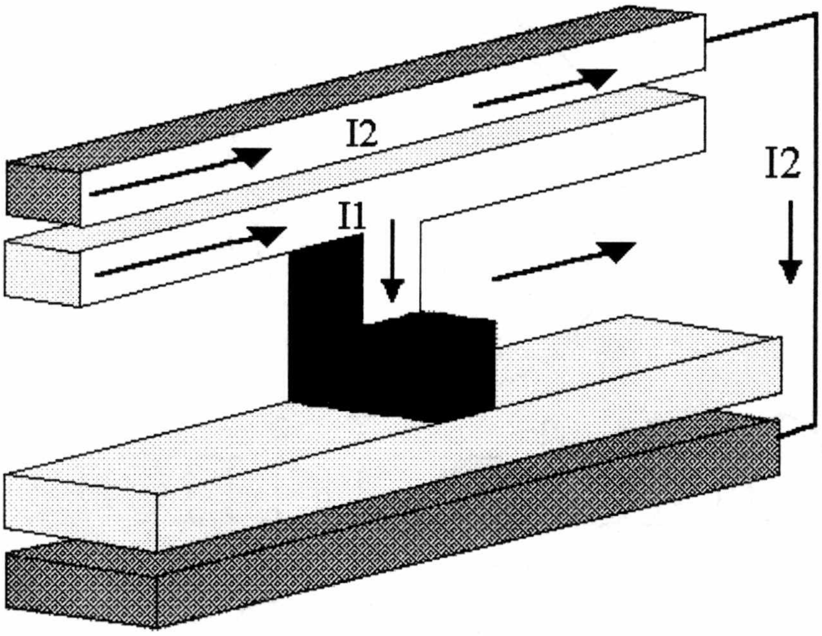

Figure 1.1. Transaugmented railgun configuration with current paths.

The HART I transaugmented railgun, which Stefani et al. referred to as an independently augmented railgun, used low ablation insulators, alumina, to do "zero-ablation" railgun experiments [7,8]. In these experiments Stefani et al. reported achieving results that were consistent with the electromagnetic armature force given by,

$$F = \frac{1}{2}L'I_1^2 + M'I_1I_2 \ , \tag{1.6}$$

where M' denotes the mutual inductance gradient per unit length, I_1 the inner rail current, and I_2 the outer (augmenting) rail current. A consistent feature of the low ablation augmented experiments was a long armature, 20 to 30 bore diameters as opposed to the typical 5 to 10 bore diameters in a conventional railgun. The conclusion that Equation 1.6 accurately predicted the electromagnetic force is questionable since there was a possibility for large error in determining the armature mass.

At the University of Tennessee Space Institute (UTSI) experiments were carried out on a transaugmented railgun [9]. In these experiments no secondaries developed and the armature remained compact, 3 to 5 bore diameters. The railgun models discussed thus far in conjunction with Equation 1.6 were not in agreement with experimental results. It was concluded that one or more of the simple lumped parameter models used was wrong.

1.3. Non-U.S. Plasma Armature Studies.

A significant amount of plasma armature railgun research was conducted in the former Soviet Union. These studies consisted of a combination of experimental and theoretical work. The Russian understanding of plasma armature behavior and the limiting velocity of railguns is somewhat consistent over several groups and is discussed here. The Japanese constructed and tested plasma armature railguns. The HYPAC gun, operated at the Institute of Space and Astronautical Science, consistently achieves over 7 km/s [10]. The Japanese are essentially using railgun technology, but do not offer any new insight into the behavior of the plasma armature. A comprehensive assessment of non-U.S. railgun research is found in Reference 11.

This Russian understanding offers a different viewpoint into why railguns fail to achieve predicted performance, but is not in direct conflict with the current views of researchers in the U.S. The Russian understanding rejects the idea that all of the ablated mass is trapped and accelerated by the plasma armature. The group at the Thermal Physics Institute state that "an impenetrable plasma piston (conductor) is valid in a very narrow range of independent parameters." The assumption that the density is zero behind the current carrying plasma is not correct [12]. This viewpoint has also been rejected by most U.S. researchers.

Zhelenznyy et al. discussed the fact that in most experiments the value of the electric field tended to be constant at about 300 to 400 V/cm. If the armature is operating as a compact plasma conductor then the electric field should rise since the magnetic pressure on the plasma rises with increased current. If this is not the case then the armature most be expanding and the mode of operation is similar to that of an electrothermal gun rather than an electromagnetic gun. They point out that the key to having a compact armature is in the initial dynamics of the formation of the armature. During these initial stages the magnetic pressure must exceed the gasdynamic pressure for the armature to operate in a compact mode. They conclude that the current must have a rapid rise at early time and a high armature current density must be maintained to operate as a compact armature [12].

A group at the High Temperature Institute in Moscow (Ostashev et al.) presented a similar view of the plasma armature [13]. They gave two regimes for which the armature could operate: the current sheath (CS), and the plasma dynamic discharge (PDD). In an earlier paper Protasov et al. performed a perturbation analysis of the 1-D MHD equations for the armature. It was concluded that the armature was susceptible to instabilities and the CS mode would always evolve into the PDD mode if plasma existed in the region between the breech of the gun and the trailing edge of the armature [11]. (The last statement shows the importance of not making the assumption that the density is zero behind the trailing edge of the armature.)

Ostashev et al. discussed the armature in terms of its plasma tail instability. They stated "to increase the reserve of PDD tail stability erosion should be intensified not decreased." They point out that "no positive results have been obtained from applying thermally strong railgun bores or from using various methods of thermal unloading." The increase in instability with increased current has to due with the decrease in density in the plasma tail due to a higher velocity and not the increase of erosion [11,13]. They also point out the case when the PDD is separated from the projectile by a currentless buffer zone. (i.e. primary separation discussed earlier in the chapter.) They state that in general the railgun is an "electro-gas dynamic energy transformer" because the projectile is accelerated by gas dynamic pressure only. They go on to give various processes which limit the velocity at which the armature gas can be directed against the projectile base. They conclude that the problem of stabilizing the CS, or eliminating destabilizing factors, is a hypothetical and unrealizable one [13].

Ostashev et al. also discussed the importance of breech voltage. They point out that if the breech voltage does not rise with velocity then the railgun is not operating as an electromagnetic accelerator. They note that at least one group reported achieving an agreement between muzzle velocity and railgun code prediction (i.e. velocity predicted by Equation 1), thus concluding the gun was operating as an electromagnetic accelerator, even though an essentially constant breech voltage was reported.

Drobyshevskiy et al. noted the problem of having a constant breech voltage, thus no electromagnetic acceleration. An analysis of experimental data revealed the cause to be a gradual expansion of the armature and the current distribution moving to the rear of the armature. Jerry Parker, in Reference 2, had suggested increasing the breakdown voltage behind the plasma armature by quenching and deionizing its rear section. This was implemented by Drobyshevskiy by the use of a mineral grease to cool the plasma. Using this grease produced a compact armature and significantly increased the efficiency of the shots [14].

The Russian understanding of the plasma armature came primarily from careful analysis of experiments and 1-D MHD simulations. This led to classifying the two modes of operation of the plasma armature as a compressed current sheath (CS) or a plasma dynamic discharge (PDD). The 1-D MHD equation perturbation analysis led to the fact that the CS would always evolve into the PDD mode. In the PDD mode if the muzzle and breech voltage do not increase in time with velocity and magnetic pressure, than the railgun is operating as an electrothermal gun and not an electromagnetic accelerator. The reasons given for this are armature expansion and the current distribution moving to the rear of the armature. It is noted that ablation is desirable to quench the rear of the armature and keep it compact. In "ablation free" experiments one of the noted problems has been long expanding armatures.

Secondary arcs are not mentioned specifically, but are a consequence of the instabilities of the plasma armature. Primary separation is pointed out specifically and it is noted that for this case momentum is transferred to the base of the projectile through gasdynamic momentum transfer. As more mass is added to this currentless buffer zone the transfer becomes less efficient.

1.4. Overview of Dissertation.

A detailed discussion of the UTSI transaugmented and muzzle-fed railgun experiments is given in Chapter II. The transaugmented and muzzle-fed railgun experiments, led to the questioning of the simple electromagnetic force models. A derivation of the simple electromagnetic force equation for a conventional railgun using the conservation of power at the breech is given at the end of Chapter II. The oversimplified assumptions which cause the model to be inaccurate are pointed out. In Chapter III a general discussion of L' and M' is given. It is necessary to understand what L' and M' are, and their dependencies in order to understand the inadequacies of the simple electromagnetic force model.

The question "how accurate are the assumptions?" is addressed in Chapters IV and V. In the first half of Chapter IV two 2-D railguns with different rail thicknesses are examined. The time dependent axial armature force predicted by the simple electromagnetic force model is compared to the actual armature force for each case. This shows how the inadequacies of the simple electromagnetic force model are related to the rail thickness. In the second half of Chapter IV a 2-D railgun is simulated with MAP3 and MEGA's 3-D formulations. This is done to examine the accuracy of each code.

In Chapter V 3-D simulations of a generic square bore railgun in the conventional, transaugmented and muzzle-fed configurations are performed. MAP3 and MEGA are both used to model the conventional railgun to test for agreement between the codes. The transaugmented and muzzle-fed configurations are used to show how the inadequacies of the simple electromagnetic force model vary with configurations. The results of the 3-D simulations suggest a modification to the simple electromagnetic force model to be used for experimental performance evaluation. Initial 3-D simulations are required to determine parameters used in the modification.

In Chapter VI the UTSI railgun experiments are analyzed with the modified electromagnetic force model. Further inadequacies of the fluid drag mechanisms in the performance model are pointed out. In Chapter VII a summary is given along with a discussion of the results.

II. WHY QUESTION THE SIMPLE ELECTROMAGNETIC FORCE MODEL?

The transaugmented railgun is an ideal experimental tool for investigating the forces in a railgun. It permits decoupling of the total electromagnetic force from the power dissipated in the armature, as discussed in the introduction. Transaugmentation allows one to keep the ablation rate constant, or the power dissipated in the armature constant, while increasing the armature force by increasing the external magnetic field.

Two series of experiments were conducted in a transaugmented railgun at UTSI in which the armature current waveform was held constant for each series and no secondary arcs formed. Comparison of experimentally observed velocities with a performance model suggested that one or more of the simple lumped parameter models was insufficient [9,15]. The fluid mechanical drag mechanisms discussed in the introduction, and the electromagnetic force model given by Equation 1.6 were included in the model. Other effects included in the performance model are discussed in this chapter.

A set of experiments was also carried out on a muzzle-fed railgun. A muzzle-fed railgun is a railgun in which the current is fed into the breech and along an outer rail to the muzzle, then back along an inner rail to the armature. A full description of a muzzle-fed railgun is given in Section 2.2. These experiments showed an even further deviation from simple railgun theory, and again suggested that one or more of the simple lumped parameter models was insufficient.

An examination of the derivation of the simple electromagnetic force equation, referring to Equations 1.1, 1.6, or similar expressions obtained for a particular railgun configuration, revealed some of the assumptions to be over-simplified for a "real railgun" (3-D railgun with finite rail thickness and width).

2.1. The UTSI Transaugmented Railgun Experiments.

2.1.1. Experimental Setup.

The UTSI transaugmented railgun was designed to function as either a conventional or augmented railgun with a 2.4 m long barrel and a 1.0 cm bore diameter. A 1.1 meter single stage helium gas injector provided pre-acceleration of the projectiles into the railgun with a velocity of approximately 1 km/s. The rails were made of copper and insulators of G-9, and were supported by a G-10 outer structure. A cross-section of the core of the gun is shown in Figure 2.1. The armature and augmenting turn were powered by separate 240 kJ capacitor discharge power supplies connected through separate, four-sectored, toroidal inductors. Lexan projectiles of approximately 1 g mass with flexible lip seals and an aluminum foil fuse were used to initiate the plasma armature [9,15].

Twenty-three B-dot probes located 100 mm apart measured changing rail current and were used to obtain accurate armature positions [16]. Two pressure transducers located 95 mm and 55 mm, directly before the breech of the rails, were

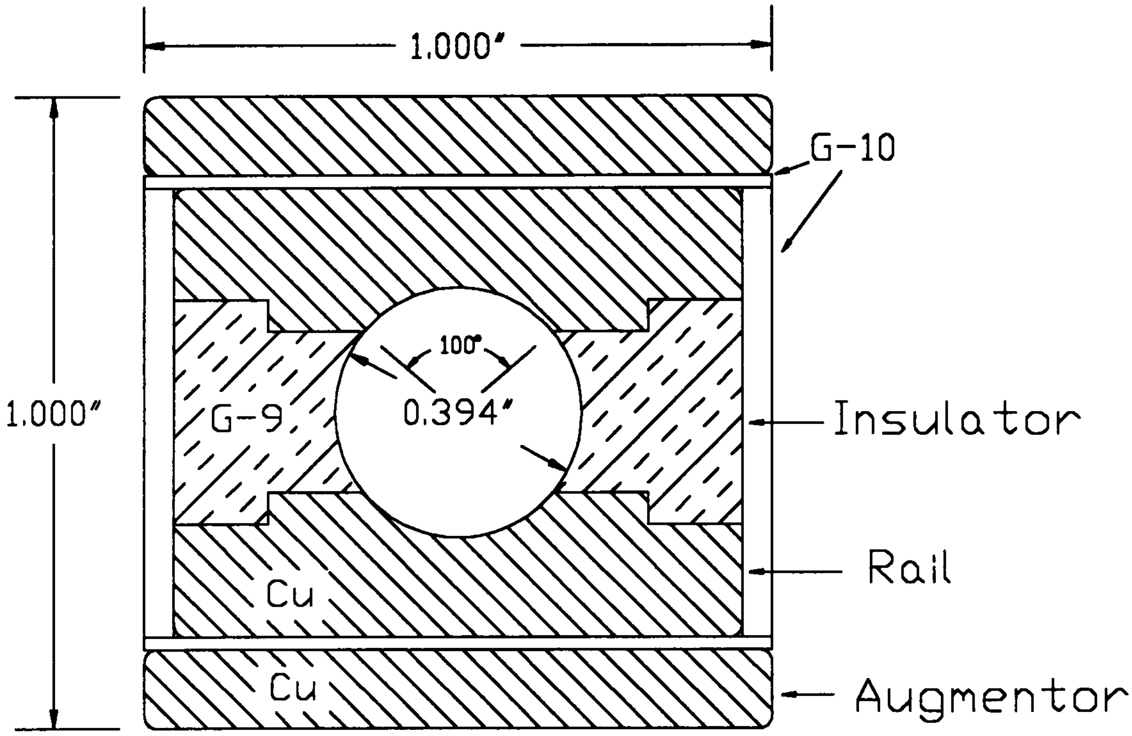

Figure 2.1. Cross section of the UTSI low inductance transaugmented railgun.

used to measure the entrance velocity of the projectile. A MAVIS electromagnetic transducer, placed in the enclosed flight range, was used to provide accurate muzzle velocity measurements [17].

Consistent bore quality for both conventional and augmented shots was maintained by lapping the entire railgun from the light gas gun to the muzzle before each shot. After lapping, acetone was circulated through the bore and dried under vacuum to remove all traces of lapping compound and hydrocarbon residue. This procedure was found to help eliminate the secondary arcs often observed when using plasma armatures.

Values of L' and M' were needed for performance evaluations. These values were calculated using the 2-D cross section of the UTSI railgun, Figure 2.1, at 10 kHz with MEGA, a 3-D electromagnetic finite element code developed at the University of Bath [18]. The value of 0.274 μH/m was obtained for L' and a value of 0.249 μH/m was obtained for M'.

Two series of experiments were performed, one using a nominal peak armature current of 70 kA and the second using a nominal peak armature current of 100 kA. Since the muzzle voltage was essentially the same at either value of armature current, this resulted in an increase of dissipated armature power of approximately 43% with 0 kA corresponding to a conventional railgun shot. This arrangement provided a factor of three range of total armature force for the 70 kA series and a factor of two range of total armature force for the 100 kA series [15].

2.1.2. Experimental Results.

A summary of the results of these experiments is given in Table 2.1. In the last column the experimental change in velocity was divided by the change in velocity predicted by,

$$v_{electromagnetic} = \frac{1}{m_p} \left(\frac{1}{2} L' \int_0^{t_m} I_1^2 \, dt + M' \int_0^{t_m} I_1 I_2 \, dt \right) , \tag{2.1}$$

where t_m is the muzzle exit time. Muzzle exit time was determined by subtracting the time the projectile was in flight from the time that the projectile entered MAVIS. The time the projectile was in flight was calculated from the MAVIS muzzle exit velocity measurement and the distance MAVIS was located from the muzzle. This assumes there was no change in velocity while the projectile was in flight [9].

The values in the last column of Table 2.1 can be referred to as momentum efficiencies. The electromagnetic impulse is defined as $mv_{electromagnetic}$ where m is the projectile mass which remained relatively constant at about 1 g. At low values of electromagnetic impulse, the experimentally observed momentum change greater than 100% of the predicted momentum change was attributed to continuing gasdynamic expansion of the accelerator gas, the fusing transient, and the electrothermal acceleration during the fusing transient. The fusing transient acceleration was due to vaporization of the aluminum fuse in an explosive manner on the back surface of the projectile resulting from the current pulse which passed through it. Electrothermal acceleration took place as the bore gas behind the armature was heated by the

Table 2.1. Summary of UTSI 2.4 m Transaugmented Railgun Experiments.

Shot	Peak Rail Current (kA)	Peak Augmented Rail Current (kA)	Mass of projectile (g)	Muzzle Velocity (km/s)	Δv_E Measured (km/s)	$\frac{\Delta v_E}{\Delta v_{elect}}$ (%)
Conventional						
8/16	67	0	.980	1.669	.630	116
10/24	105	0	.979	2.258	1.162	101
6/17	106	0	.984	2.476	1.365	115
11/20*	109	0	1.06	2.008	.988	79
9/19	120	0	.992	2.379	1.299	84
9/6	134	0	.994	2.655	1.602	85
7/30	138	0	.996	2.493	1.469	73
Augmented						
9/25	68	30	.980	1.966	.886	99
1/14	67	71	.985	2.333	1.203	87
1/10	64	103	.994	2.36	1.305	78
1/16*	65	138	1.008	2.418	1.366	66
4/15	65	140	1.008	2.788	1.692	87
1/17	104	49	.992	2.620	1.539	76
10/29	105	107	.995	3.085	1.990	72
6/28	104	108	.968	3.046	1.950	63
7/10	102	142	.969	3.135	2.055	60

* Secondary developed
L' = 0.274 (μH/m), M' = 0.249 (μH/m)
Values of L' and M' were obtained from 2D MEGA calculations with a frequency of 10 kHz.

armature and the rails. Table 2.1 demonstrates that as the electromagnetic impulse increased the efficiency decreased.

A railgun performance model was constructed which included the accelerating effects of the continued expansion of the helium accelerating gas, the electrothermal acceleration due to the vaporization and heating of the aluminum foil fuse, and the fluid mechanical drag mechanisms discussed in the introduction. It also included the drag effects due to compression, acceleration and viscous drag of the residual bore gas ahead of the projectile [19]. Full details of this model are given in Refs. [2,3,4,9,15,19].

The fusing transient, the helium expansion from the light gas gun, and the electrothermal heating of the bore gas were modeled with the empirical formula,

$$p = [\, p_o + (\gamma\, t)^{\eta}\,]\, e^{-\beta t} \,, \tag{2.2}$$

where p is the total pressure of the gas on the projectile, p_o is the initial pressure of the helium, and γ, η, and β are adjustable parameters. Values of the parameters used in Equation 2.2 and the ablation drag coefficient in Equation 1.4 were obtained from the conventional baseline shots, or shots with no augmentation, with armature currents of 70 kA and 100 kA. Inclusion of the accelerating gasdynamics and electrothermal effects removed the greater than 100% momentum efficiency observed at the lowest values of electromagnetic momentum. The inclusion of the various drag effects improved the prediction at higher values of electromagnetic momentum, but there was still a significant deficit in performance, as shown in Figure 2.2. Note that the effects of primary separation, primary separation being the actual separation of the armature from the projectile as discussed in the introduction, were not included in the

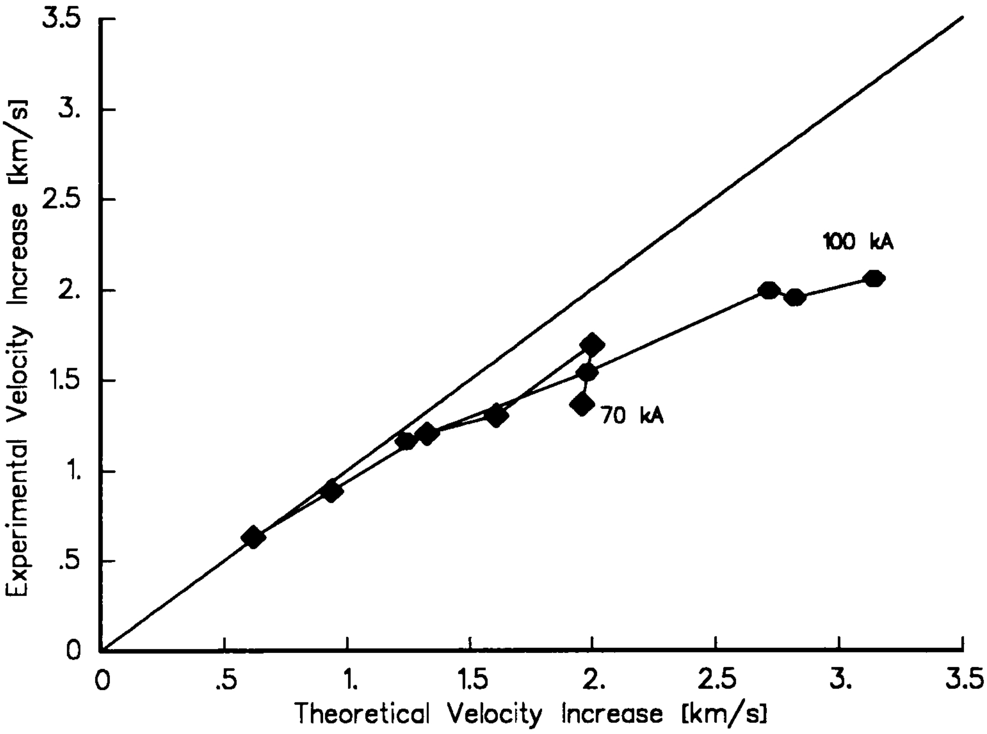

Figure 2.2. Comparison between experimentally observed velocity increase and performance model predictions for augmented railgun.

performance model. Primary separation was observed near muzzle exit on nearly every shot.

2.1.3. Conclusions from the Transaugmented Railgun Experiments.

Conclusions drawn from the UTSI transaugmented railgun experiments were given by Dr. Dennis Keefer in Reference 10, and are reproduced here.

> "The failure to predict accurately the railgun performance with the performance model led to the conclusion that one or more of the simple lumped parameter models used was wrong! For a given series of experiments with fixed armature current the ablation rate remains essentially constant as the augmentation is increased. Therefore, the electrothermal acceleration and the ablation drag is also essentially constant. The predicted increase in velocity with increasing augmentation is essentially due only to the increased electromagnetic force provided by the augmented turn, less the increased viscous drag due to the higher velocity. Therefore, since the observed increase in velocity with increasing augmentation was less than predicted, the electromagnetic force model was suspected to be inaccurate [15]."

2.2. The UTSI Muzzle-Fed Railgun Experiments.

The muzzle fed configuration, reportedly first operated in the former Soviet Union, is a railgun in which the current is fed into the breech and along an outer rail to the muzzle, then back along an inner rail to the armature [20]. * The configuration of a muzzle-fed railgun with the current path is shown in Figure 2.3. The driving

* Portions of this dissertation are excerpts from an article entitled "Muzzle-Fed Railgun Experiments with 3-D Electromagnetic Simulations," written by J. Taylor, R. Crawford and D. Keefer, and published in the *IEEE Transaction on Magnetics*, Vol. 31, No. 1, pp. 360-364, January 1995.

force in a muzzle-fed railgun is supplied by the augmenting rail behind the armature. In front of the armature the field produced by the inner rails is mostly cancelled by the field produced by the outer augmenting rails. Extending the conservation of power at the breech argument used to derive Equation 1.1 for the conventional railgun to the muzzle-fed configuration, the electromagnetic force for the muzzle fed case is,

$$F = \frac{1}{2} M' I^2 + \frac{1}{2} (M' - L') I^2 . \tag{2.3}$$

The derivation for Equation 2.3 is given in Appendix A.

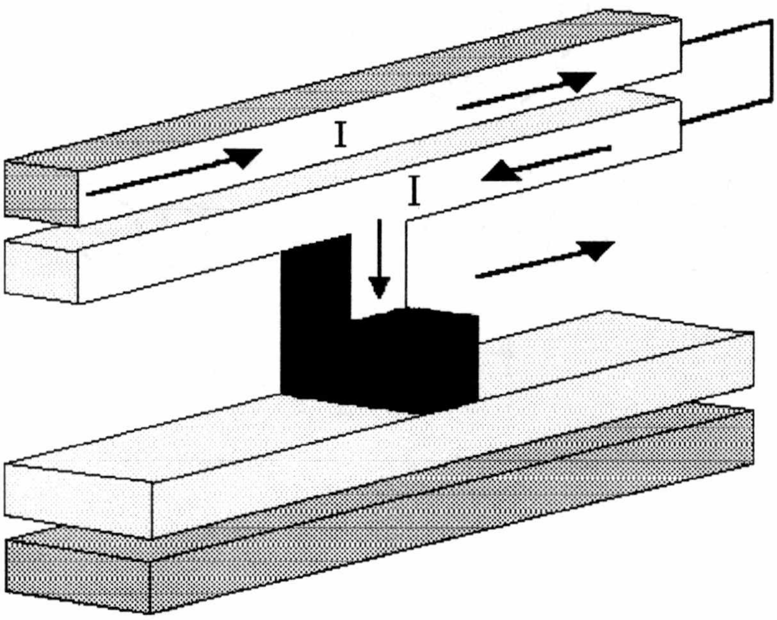

Figure 2.3. Muzzle-fed railgun configuration with current paths.

Written in this form it is easy to see that as the rails become more tightly coupled and the value of M' approaches that of L', Equation 2.3 approaches the force equation for a conventional railgun, 1/2 $L' I^2$, with M' replacing L'. The first expression in Equation 2.3 is the force due to the magnetic field produced by the augmenting rail behind the armature and the second expression demonstrates the field cancellation in front of the armature.

2.2.1. Experimental Setup.

The UTSI 2.4 m long, 1.0 cm round bore, transaugmented railgun was converted to a muzzle-fed configuration. This was done by inserting a short at the muzzle between the inner and outer rails. The inner rail power supply current feeds were removed from the railgun. The power supply current feeds for the outer rails remained attached, so that the current path was identical to that shown in Figure 2.3.

Other than the change in electrical configuration, all hardware and diagnostic equipment, such as the light gas gun and the twenty-three rail B-dot probes, remained the same as it was for the transaugmented railgun described in Section 2.1.1. Since the same rails were used, the values of L' and M' were again 0.274 μH/m and 0.249 μH/m respectively. The experimental procedure, in which the bore was lapped between each shot, was also the same as described in Section 2.1.1.

2.2.2. Experimental Results.

Four experiments were performed on the muzzle fed railgun, one at a peak current of 70 kA and three at a peak current of 100 kA. The experimental results are given in Table 2.2, together with results for similar experiments in the conventional configuration for comparison. The muzzle velocity was obtained from MAVIS, and the rail entrance velocity was obtained from the two pressure transducers located near the breech of the rails. The experimental change in velocity, column 6, was the difference between the measured exit velocity and the measured entrance velocity.

In the last column of Table 2.2 the experimental change in velocity was divided by the change in velocity predicted by

$$v_{electromagnetic} = \frac{1}{m_p} \left(M' - \frac{1}{2} L' \right) \int_0^{t_m} I^2 \, dt \ , \qquad (2.4)$$

using the measured current. The muzzle exit time, t_m , was determined by subtracting the time the projectile was in flight from the time that the projectile entered MAVIS. The time the projectile was in flight was calculated from the MAVIS muzzle exit velocity measurement and the distance MAVIS was located from the muzzle [9].

The increase in velocity for the 100 kA muzzle fed experiments achieved less than 50% of the expected change in velocity calculated from Equation 2.4. Most of the acceleration seen in the experiment could be accounted for by thermal forces exerted during the fusing transient. Taking this into consideration, the experiments achieved well below 50% of the expected change in velocity calculated from

Table 2.2. Summary of UTSI 2.4 m Muzzle Fed Railgun Experiments.

Shot	Type	Peak Rail Current (kA)	Mass of projectile (g)	Muzzle Velocity (km/s)	Δv_E Measured (km/s)	$\frac{\Delta v_E}{\Delta v_{electromagnetic}}$ (%)
8/16/91	Conven	67	.980	1.669	.630	116
10/24/91	Conven	105	.979	2.258	1.162	101
6/17/91	Conven	106	.984	2.476	1.365	115
11/20/92*	Conven	109	1.06	2.008	.988	79
11/11/92	Muz Fed	70	1.03	1.292	.279	67
11/18/92	Muz Fed	106	1.05	1.470	.457	48
12/14/92✡	Muz Fed	106	1.06	1.350	<.400	<41
1/27/93	Muz Fed	108	1.06	1.496	.429	41

* Secondary developed

✡ Entrance velocity could not be determined from data. Nominal entrance velocity for this railgun has been 1.0 ± 0.05 (km/s). There was nothing to suggest this was not a nominal shot.

Equation 2.4. Since the initial experimental results differed so much from prediction, three experiments were performed at 100 kA to establish repeatability.

The B-dot signals indicated a compact well-formed plasma armature with no evidence of secondary arc formation. Figures 2.4 and 2.5 show the armature velocity obtained from the B-dot probes, together with the exit velocity of the projectile obtained from MAVIS for 70 kA and 100 kA peak current shots. Notice the severe primary separation of the primary arc from the projectile as shown by the difference between the projectile exit velocity and the final armature velocity. Results for similar experiments in the conventional railgun configuration are also shown in Figures 2.4 and 2.5 for comparison.

The armature velocity for the muzzle-fed shots scarcely exceeded the initial velocity. It is likely that most of the increase in projectile velocity was due to the electrothermal "kick" which accompanied the fusing transient.

Equation 2.3 can be rearranged in the form $1/2\ L'_{eff} I^2$ where L'_{eff} is equal to $(2M' - L')$ and has a value of 0.224 μH/m. This is 82% of the value of L'. From the simple electromagnetic force models, the force for the muzzle fed shots should have been 82% of that for the conventional shots. However, as can be seen in Table 2.2, and Figures 2.4 and 2.5, the change in velocity measured for the muzzle fed configuration was less than half of that measured for the conventional case. There were no secondary arcs observed for the muzzle fed experiments.

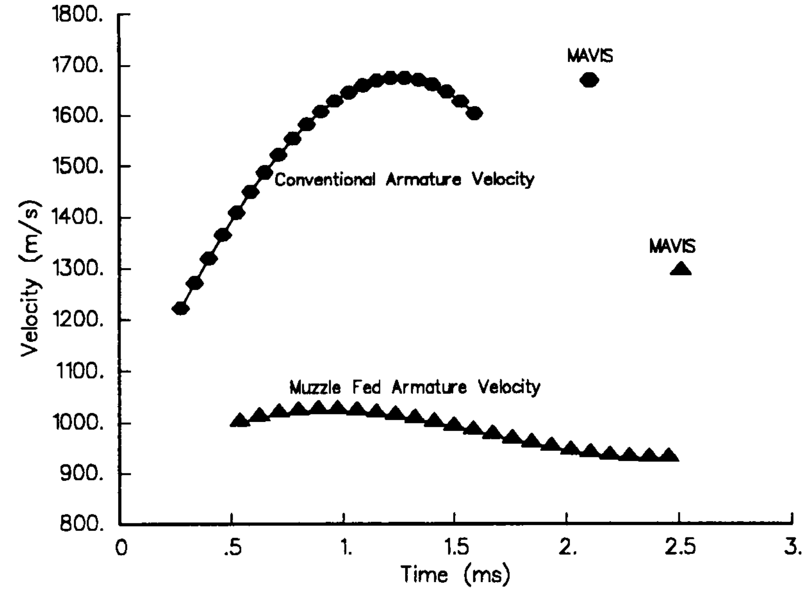

Figure 2.4. Comparison of conventional and muzzle-fed railgun shots with 70 kA peak current.

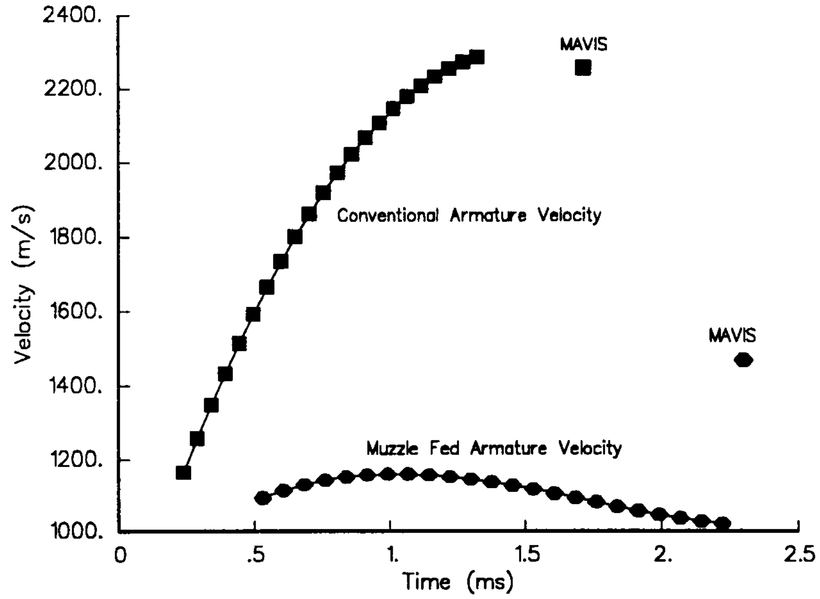

Figure 2.5. Comparison of conventional and muzzle-fed railgun shots with 100 kA peak current.

2.2.3. Conclusions from the Muzzle-Fed Railgun Experiments.

These experiments again raised questions about simple railgun theory. The armature velocities for the muzzle-fed shots were significantly less than the corresponding conventional railgun shots. These experiments were run under identical conditions so the mechanical drag parameters, whatever they were, should have remained constant. Since the drag models are velocity dependent the drag should have been less for the muzzle-fed railgun shots than for the conventional railgun shots. From these arguments it was concluded that it was the simple electromagnetic force model, Equation 2.3, that was insufficient.

2.3. Derivation of the Simple Electromagnetic Force Equations.

The armature force in a railgun can be calculated directly by integrating

$$\mathbf{F} = \mathbf{J} \times \mathbf{B} \ , \tag{2.5}$$

over the volume of the armature, where **J** is the current density and **B** is the magnetic induction in the armature. However, the current density in the rails and armature are complicated functions of space and time, and until recently could not be modeled for 3-D railguns. Instead, the electromagnetic force equation was obtained from simple models, and the values of L' and M' must be determined for the particular railgun of interest. The term "simple models" is used here to refer to different methods used to obtain Equations 1.1 and 1.6. Two methods are presented for obtaining the simple electromagnetic force equation. By pointing out limitations and assumptions made with each method it is shown that neither method correctly models a "real railgun".

2.3.1. Filament Circuit Wire Method.

Equation 1.1 can be derived in many ways. Dr. Montgomery Smith [21] and Dr. Hugh Calvin [22] obtained Equation 1.1 directly for a filament wire circuit shown in Figure 2.6. This was done by evaluating,

$$\mathbf{F} = \int \mathbf{I}\, \mathbf{dl} \times \mathbf{B} \,, \tag{2.6}$$

over the movable current filament, which acted as the armature, obtaining an expression for the armature force. This expression was then compared to Equation 1.1 where L' was calculated by calculating the flux produced by a unit length of the rails and setting this flux equal to $L'I$. The force on the armature obtained directly, with the use of Equation 2.5, was that given by Equation 1.1.

In the derivation L' was defined as the inductance per unit length of the rails only. The flux produced by the breech and armature currents were not included, since the breech was assumed to be far away, and the armature cannot produce a self force. By definition a filament wire has no current distribution. The L' obtained from the filament wire railgun was the same as that obtained from two infinitely long filament wires located the same distance apart.

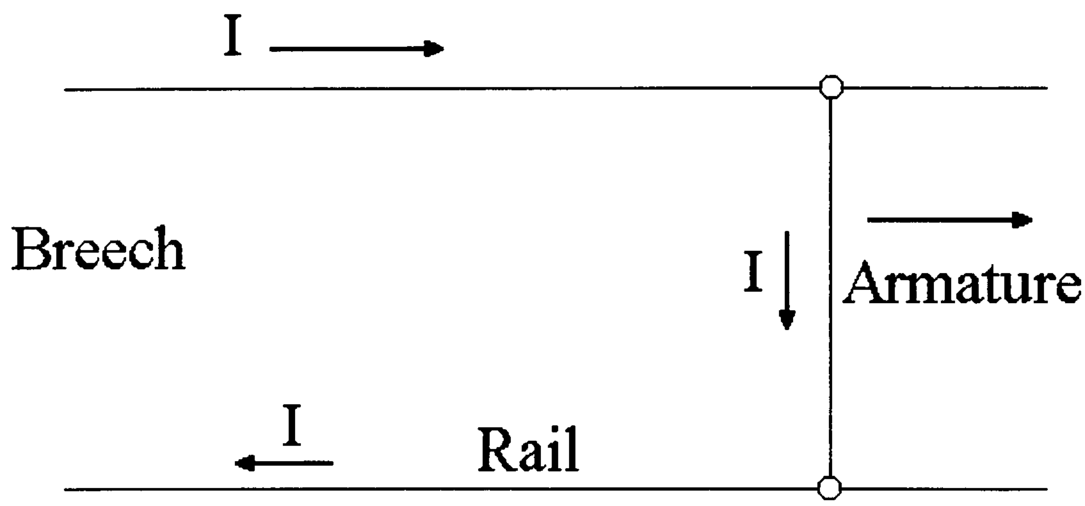

Figure 2.6. Filament wire circuit model of railgun.

The limitations of this derivation come from the fact that there was no current distribution in the rails. A filament wire is a line of current and the current makes a perfect 90° degree turn into the armature from the rails. In this ideal case there were no axial forces exerted in the rails, since there was not a transverse component of **J** in the rails, and there were no eddy currents in the rails.

2.3.2 Conservation of Power Method.

Another way to derive Equation 1.1 is with conservation of instantaneous energy (power) arguments [23]. Consider an arbitrary conventional railgun with power connections at the breech and an armature moving in the x-direction. The total power input to the railgun is the current multiplied by the breech voltage,

$$P = I\left(I\frac{dL}{dt} + L\frac{dI}{dt} + IR\right) \ , \tag{2.7}$$

where R is the resistance of the rails and armature, L is the total self inductance of the system, and I is the total current input to the breech. A point should be made here about the I^2R , ohmic heating, term. A portion of the energy from the ohmic heating can go into acceleration of the armature through the fusing transient and thermal heating of the bore gas. In this derivation, however, we are only interested in the electromagnetic force.

In moving the armature, power is required to change the stored magnetic field energy represented by W_f , and is given by,

$$\frac{dW_f}{dt} = \frac{d}{dt}\left(\frac{1}{2}LI^2\right) = LI\frac{dI}{dt} + \frac{1}{2}I^2\frac{dL}{dt} \ . \tag{2.8}$$

In Equation 2.7 two forms of power are immediately accounted for, the I^2R term and the changing stored magnetic field energy. Power is always conserved, so subtracting Equation 2.8 (changing stored magnetic field energy) and I^2R from Equation 2.7, one is left with

$$\frac{dW_a}{dt} = \frac{1}{2}I^2\frac{dL}{dt} \ . \tag{2.9}$$

Equation 2.9 represents the power supplied to the circuit above that goes into stored magnetic field energy and ohmic heating. One chosen name for this quantity, W_a , is the "associated energy" of the inductance change, since it appears anytime the inductance of a circuit is changed [24]. At this point no critical assumptions have been made. Problems arise with the assumptions made as to what form of power Equation 2.9 represents and how to express dL/dt as something other than the time rate of change of the total self inductance of the circuit.

There are two typical assumptions made at this point. The first assumption is that the change in inductance can be written as L' times the velocity of the armature. With this assumption Equation 2.9 becomes,

$$\frac{dW_a}{dt} = \frac{1}{2} I^2 L' v \quad . \tag{2.10}$$

Note that Equation 2.10 is a representation of the change in associated energy, and no assumptions have been made as to what form that energy takes. With Equation 2.10 comes the question as to what value of L' to use. A detailed discussion of this is given in Chapter III.

For at least two cases the change in associated energy is known. The first case is the filament wire railgun where there is no field diffusion in the rails. (I.e. no eddy currents due to armature motion.) The second case is for a "real railgun" with the armature located far enough away from the breech so that the field has fully diffused into the rails there. In this case the value of L', obtained from the fully diffused field for the 2-D cross section, would yield the correct change in associated energy as given by Equation 2.10.

The second assumption typically made is that all the change in energy given by Equation 2.10 goes into mechanical energy of the armature. Since mechanical power is equal to force times velocity, if we divide both sides of Equation 2.10 by velocity we obtain

$$F = \frac{1}{2} L' I^2 \ . \tag{1.1}$$

2.3.3. Invalid Assumptions.

For the filament wire railgun, Equation 2.10 does correctly represent the change in associated energy. Furthermore, all the associated energy does go into mechanical energy of the armature, thus Equation 1.1 represents the correct armature force for that idealized case.

In a "real railgun" Equation 2.10 is questionable, but with care it can be closely approximated. The assumption that all the associated energy goes into mechanical work is wrong! A "real railgun" has eddy currents and a transverse component of **J** in the rails, unlike the filament wire railgun. The transverse component of **J** in the rails produces forces in the rails and an associated strain energy in the structure. This acts to reduce the force available to the armature. The eddy current part is more complicated.

Eddy currents are generated anytime a conductor moves through a magnetic field gradient, or the magnetic field in a conductor changes in time. To illustrate this we will examine some examples. Consider a conductor moving through a constant magnetic field. In this case there would be no eddy currents in the conductor, but there would be a potential difference induced on the conductor. If the conductor were connected to an external circuit, current would flow. This illustrates the case of the armature which does not see a change in the magnetic field due to motion. The armature does have a $\mathbf{v} \times \mathbf{B}$ term that produces an electric field in the armature, but no eddy currents.

If a conductor is moving from a region where there is no magnetic field into a region where there is a magnetic field, then eddy currents are induced in the conductor. For a railgun the rails can be thought of as moving by the armature. The rails are moving through a magnetic field gradient and eddy currents are induced in the rails. From Lenz's law the direction of the eddy currents is such to produce a magnetic field that opposes the change in magnetic field. The magnetic field produced by the eddy currents in the rails interact with the magnetic field of the armature to oppose the armature motion, Figure 2.7.

In a "real railgun" around the armature all three components of the magnetic field exist. Each component of the magnetic field produces an eddy current in the rails to oppose it. As an example, the axial component of a magnetic field is in the opposite direction on opposite sides of the armature. Thus, the eddy currents produced by the axial component of **B** around the armature is in opposite directions in each half of the rail, Figure 2.8.

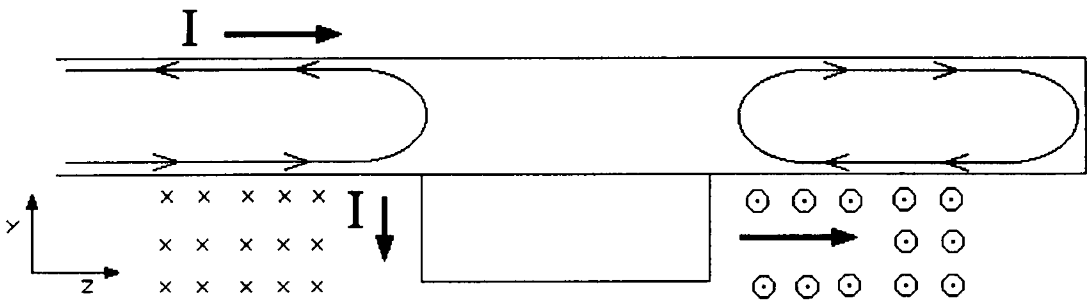

Figure 2.7. Induced eddy currents in the yz-plane due to armature motion.

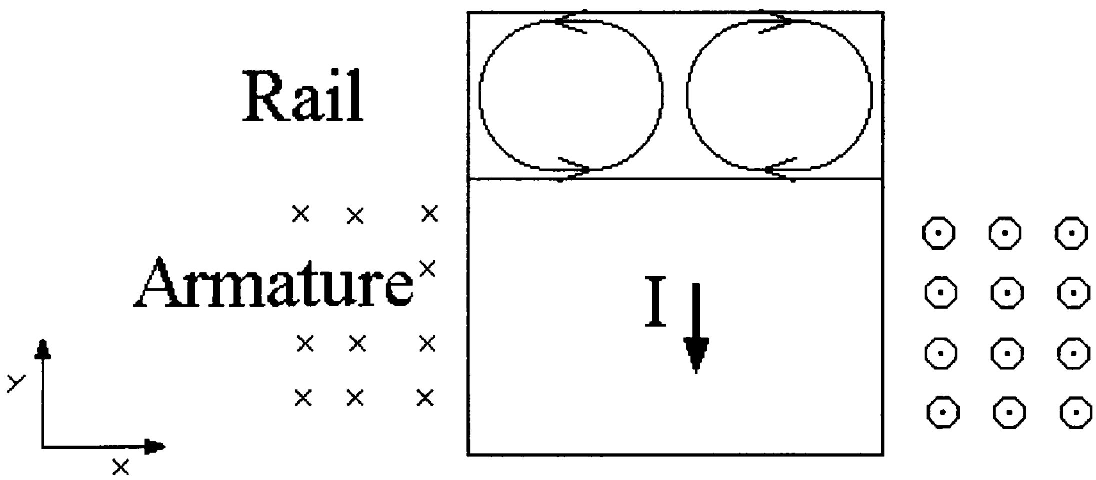

Figure 2.8. Induced eddy currents in the xz-plane due to armature motion.

The B_y component produced by the armature is small compared to the B_x and B_z components. For this reason the eddy currents generated in the xz-plane of the rails are small in comparison to the ones generated in the xy and yz-planes.

What do eddy currents mean in terms of the power argument? The eddy currents in the rails produce a magnetic field which interacts with the magnetic field of the armature to oppose the armature motion. Eddy currents dissipate heat giving a form of power that was not accounted for in the power argument where it was assumed all the change in energy is translated to mechanical energy of the armature.

Using the same derivation methods used to derive the simple electromagnetic force model for the conventional railgun, expressions are obtained for a transaugmented (Equation 1.6) and a muzzle fed railgun in Appendix A [25]. In each case the assumptions made are invalid for the same reasons discussed above.

III. WHAT ARE L' AND M' ?

In order to use Equation 1.1 in a performance model one must obtain a value of L'. To obtain a value for L' one must first know the definition for L'. One can either run experiments on a shunted railgun, or variations of this, or calculate the current distribution of the 2-D cross section of the rails. The current distribution, however, is dependent upon the diffusion time of the field (frequency) and the boundary conditions imposed on the problem.

In this chapter the dependencies of L' and M' on boundaries and frequency are examined. The finite element method was applied to a 2-D cross section of a railgun where the boundaries were varied. With one of the boundaries a time dependent solution was calculated. Another method capable of solving for L' in the high frequency limit was used to give confidence in the finite element calculations.

The following convention is used to clarify what computational planes the 2-D cross sections and the 2-D railgun are in. This convention is used throughout the rest of this dissertation. The axial direction of the rails, or the direction of armature motion is chosen to be in the z-direction. The rail width is in the x-direction and the rail height is in the y-direction. The 2-D cross section, used to evaluate L' and M', is then in the xy-plane and the 2-D railgun calculations are in the yz-plane.

L and M, self inductance and mutual inductance, are geometrical factors used to describe the flux linking a circuit. For simple linear circuits Neumann's formula

$$L_{ik} = \frac{\mu_o}{4\pi} \oint \oint \frac{dl_i \cdot dl_k}{r_{ik}} , \tag{3.1}$$

gives the geometrical quantities, L_{ii} - self inductance of the i^{th} circuit and L_{ik}- the mutual inductance between the i^{th} and k^{th} circuits [26]. Equation 3.1 assumes that there are no boundaries on the system and that the circuits consist of filament wires [27].

Another way of obtaining the inductances, which works with all circuits, is with the expression

$$W_f = \frac{1}{2\mu_o} \int_\infty B^2 dV = \frac{1}{2} L I^2 , \tag{3.2}$$

where the volume integral extends over all space. If two circuits are involved Equation 3.2 is modified to

$$W_f = \frac{1}{2\mu_o} \int_\infty B^2 dV = \frac{1}{2} L_1 I_1^2 + \frac{1}{2} L_2 I_2^2 + M_{12} I_1 I_2 . \tag{3.3}$$

Equations 3.2 and 3.3 hold for any 2-D or 3-D circuit. The quantities L' and M' are defined as the self and mutual inductance per unit length for a 2-D cross section of the rails (similar to Figure 2.1), where there is no gradient in the **B** field distribution down the length of the rails.

The values of L' and M' can be determined experimentally or computationally. Experimentally one would put a shunt in the muzzle of a railgun, apply a high frequency current source to the breech and measure the total self inductance of the system. The value of L', at the applied frequency, would then be given by the total inductance measured divided by the rail length, assuming that L' is independent of position and that one took precautions to avoid stray inductances. The value of L' increases as the frequency decreases [27]. The maximum value of L' occurs when the field has time between each cycle to fully diffuse into the structure.

Another experimental method would be to again apply a high frequency current source at the breech and to put a conducting slug in the bore. One would than move the conducting slug and measure the inductance of the circuit. The difference in inductance due to moving the conducting slug divided by the distance the slug was moved equals L'.

Numerical techniques can also be used to obtain the inductance gradients. Applying one of several numerical techniques to the 2-D cross section of the rails one obtains the **B** field distribution over the whole computational domain. With numerical techniques one typically uses the magnetic vector potential, **A**, since only the axial component of **A**, A_z, is needed. The relationship between **B** and **A** is,

$$\mathbf{B} = \nabla \times \mathbf{A} \ . \tag{3.4}$$

From the relationship,

$$\mathbf{J} = \frac{1}{\mu} \nabla \times \mathbf{B} \ , \tag{3.5}$$

and the fact that **B** does not vary in the z-direction, one is left with only the J_z component of **J**. In MEGA boundary conditions are applied such that the magnetic field is tangent to the outer boundary surface. This is the boundary condition for a superconducting surface.

Once **B** is obtained everywhere, Equation 3.2 is used, with L' replacing L, to obtain L_1' and L_2' by powering each circuit individually with the other circuit present but zero current flow. Once these are obtained, both circuits are given a current flow and M_{12}' is obtained from Equation 3.3. Since we do not need L_2' to calculate the armature force, and M_{12}' equals M_{21}', from here on L_1' is referred to as L' and M_{12}' is referred to as M'.

To gain an understanding of how L' and M' vary with different geometries, field diffusion time and applied boundary conditions, several examples are presented. Two numerical techniques were used to solve for the **B** field distribution. The finite element method (see reference 28 for a general description of this technique) was used to solve the equation,

$$-\nabla \cdot \frac{1}{\mu_o} \nabla A_z + \sigma \frac{\partial A_z}{\partial t} = J_z \ , \tag{3.6}$$

from which the **B** field distribution was obtained. This method was implemented in MEGA, a 3D finite element electromagnetic code, and can be used for arbitrary geometries with time dependent current wave forms or specified frequencies [18].

The second set of solutions was performed at Los Alamos National Laboratory. The solutions were obtained from the limiting case of a rapidly pulsed source, which is equivalent to the conductors being superconductors in which no magnetic field diffusion occurs. For this limiting case Equation 3.6 reduced to

$$\nabla^2 A_z = -\mu_o J_z \tag{3.7}$$

The method consisted of solving for the current distribution that gave constant values of the magnetic vector component A_z on the conductor surface. A method for solving this type of problem and a computer code had been developed by Crandall and was applied to this problem [29]. The method approximated the current density on the surface of the conductor with a sequence of cubic splines, where the conductor could have been of arbitrary shape. Once the current distribution on the surface of the rails was known, the value of L' was calculated analytically [30].

In the paper by Kerrisk (Reference 30) the general problem pictured in Figure 3.1 was examined , with no boundaries (i.e. the magnetic field extended to

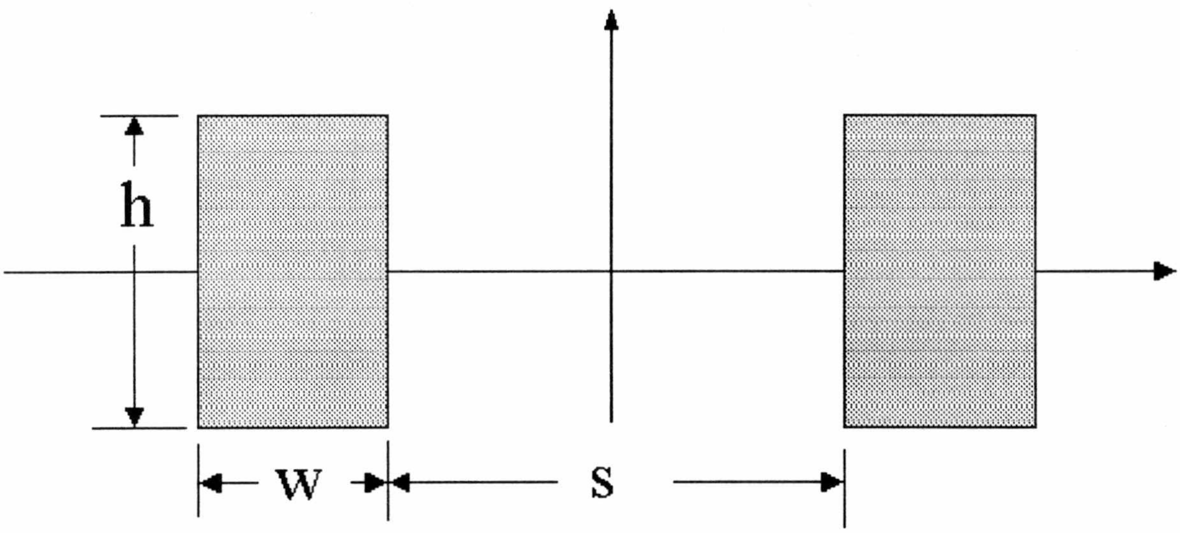

Figure 3.1. Cross section of two rectangular conductors.

infinity), and the current was restricted to the rail surface. It is possible to solve a problem of this type with Crandall's method, since Crandall's method only solves for the current distribution on the rail surface. The finite element method solves for the A_z over all of the computational domain, making the solution of a problem with boundaries at infinity impossible.

It was found for this geometry that L' was strictly a function of the two parameters w/h and s/h (refer to Figure 3.1). A table of values for L' was calculated for s/h ranging from 0.08 to 12.0, and w/h from 0.1 to 10.0. As s/h increased the value of L' increased. As w/h increased the value of L' decreased. The values of inductance per length ranged from 0.07416 μH/m for w/h = 10.0 and s/h = 0.08, to 1.48283 μH/m for w/h = 0.1 and s/h = 12.0. From this elementary understanding, to increase the armature force, the rails should be as far apart as possible and as narrow as possible.

If the magnetic field is not allowed to extend to infinity (i.e there are boundaries on the problem) then the value of L' is reduced. The case where w/h = 0.5 and s/h = 1.0 was examined in more detail to determine the dependence on the boundaries. The value of L' with boundaries at infinity was 0.49073 μH/m using Crandall's method.

The computation of a 2-D cross section performed with MEGA takes advantage of symmetry relationships. On the center line of the rails there is no tangent component of magnetic flux, only a normal component. A normal flux (NF) condition was applied to this boundary. The NF condition is implemented by setting the partial derivative of A_z with respect to the normal direction of the surface equal to zero. From Equation 3.4 it is readily shown that this sets the component of **B** tangent to the surface equal to zero. Setting the partial derivative of the variable with respect to the normal direction of the surface is the natural boundary condition used in the finite element method.

On the center line between rails there is no normal component of magnetic flux, only a tangential component. On this boundary a tangent flux (TF) condition was applied. This condition is set by setting the partial derivative of A_z with respect to the tangential direction of the surface equal to zero. Using Equation 3.4 it is shown that this sets the normal component of **B** equal to zero. The computational domain limited to some finite region. At the limits of the computational domain a TF boundary condition was applied. The limits of the computational domain was will be referred to as the outer boundaries. The boundary conditions are identified in Figure 3.2.

MEGA calculations were also performed to approximate the case where $w/h = 0.5$ and $s/h = 1.0$. For these calculations the outer boundaries were continually moved further away from the rails until the energy stored in the field ceased to change. Copper rails with a 1.0 MHz sinusoidal current waveform were used to simulate the superconducting case. The skin depth for 1.0 MHz was calculated to be $\delta = 0.068$ mm, and the smallest elements used on the surface of the conductor where 0.218 mm. The MEGA simulation did not quite resolve this skin depth. MEGA calculations gave $L' = 0.49033$ μH/m, 0.08% smaller than the L' calculated by

Crandall's method showing good agreement between MEGA and Crandall's method. The actual geometry used in the MEGA calculation is shown in Figure 3.2. The infinite boundary case actually had a TF boundary condition applied at 0.3 m.

The outer rectangular boundary was then gradually reduced giving L' as a function of the boundary distance. In Figure 3.3, the value of L' decreased to 0.35843 μH/m at the boundary location of 0.016 m. This was a 27% reduction in the value of L' by simply applying a boundary. Why does the energy stored in the field decrease as the boundary is moved in?

To answer this question consider the case of a railgun enclosed in a metallic tube, the actual geometry of which is shown in Figure 3.4. The tube is described as a general metallic tube since it is never actually modeled, but used only for the purpose of discussion. Without the presence of the metallic tube, and the outer boundary moved far enough away from the rails to have minimal effect on the solution, L' calculated with MEGA at a frequency of 1 MHz, was found to be 0.5369 μH/m. This is the same value of L' that would be obtained in the presence of the metallic tube, if the rails were superconductors, and the fields fully diffused through the metallic tube.

At the high frequency limit the metallic tube and rails behave like superconductors. The value of L' dropped to 0.1402 μH/m for this case, as calculated with MEGA. The high frequency limit of L' was reduced by 74% by placing it in the metallic conductor. The reason the value of L' was reduced can be thought of in terms of the eddy currents produced in the metallic structure. In the high frequency limit the

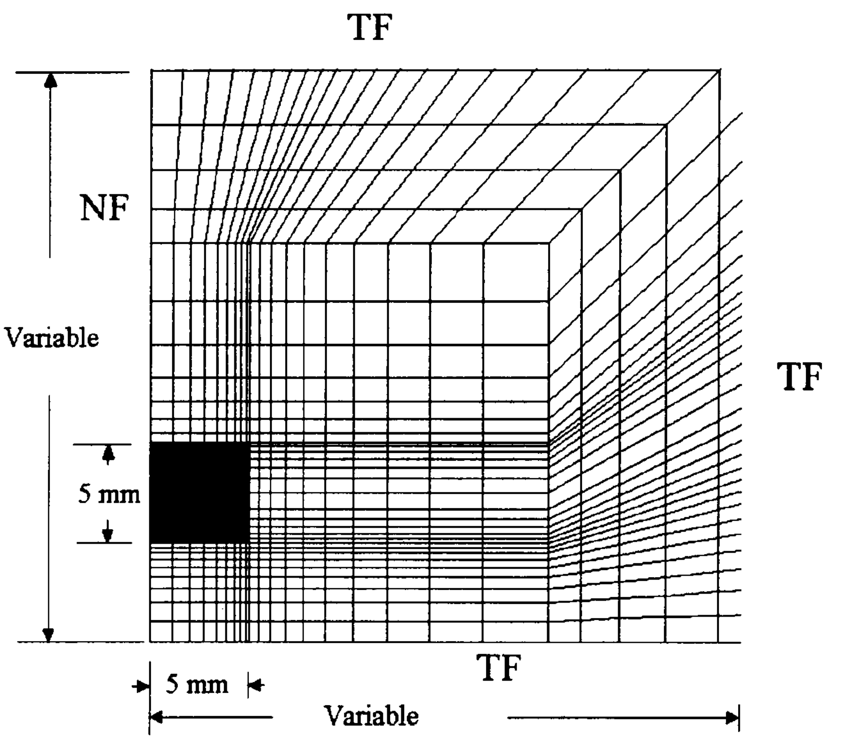

Figure 3.2. Model used in MEGA calculations of two rectangular conductors.

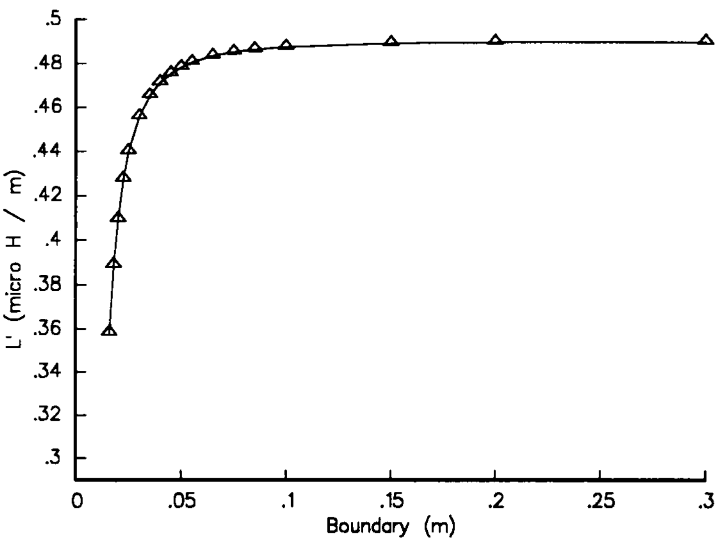

Figure 3.3. L' for two rectangular conductors as a function of the boundary location.

eddy currents exclude all magnetic flux from the metallic tube. This reduces the energy stored in the magnetic field and thus reduces the value of L'. Crandall's method produced a value of $L' = 0.1412$ μH/m, again showing good agreement between it and MEGA.

The diffusion of the **B** field (redistribution of current) also affects the value of L'. As the magnetic field diffuses into the metallic structure, the energy loss due to eddy current generation decreases, and the stored magnetic field energy increases. Similarly, as the magnetic field diffuses into the rails the stored magnetic field energy increases and the value of L' increases.

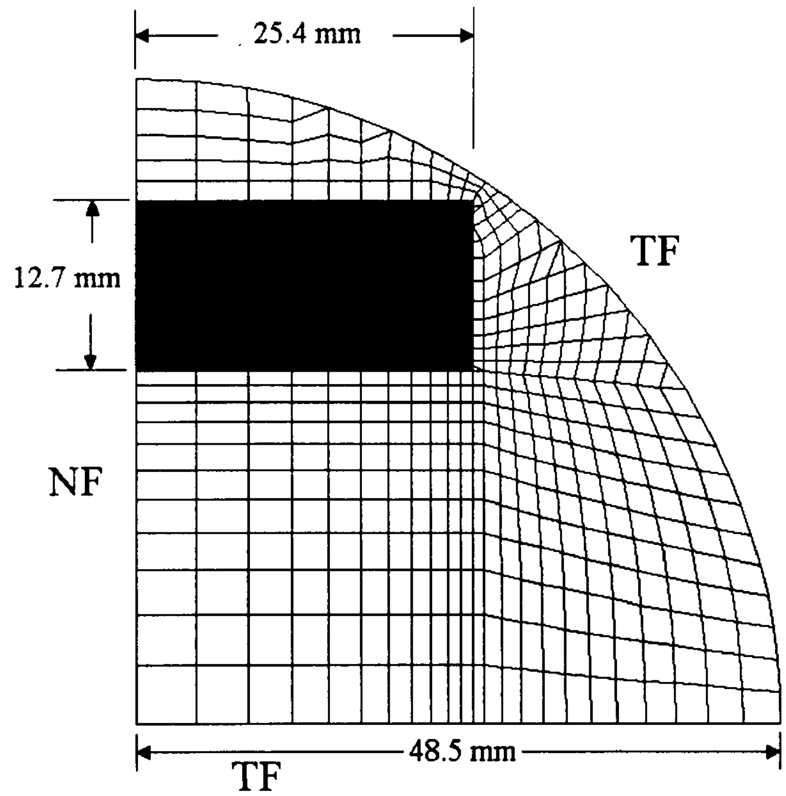

Figure 3.4. MEGA model of two rectangular conductors in a tube.

If one starts with a step input of current, a time dependent value of L' is obtained. The cross section of the generic square bore railgun geometry used for the 3-D MEGA simulations in Chapter V is shown in Figure 3.5. Using this cross section with MEGA and employing Equations 3.2 and 3.3, time dependent values of L' and M' were obtained and plotted in Figure 3.6. As the field diffused into the rails the values L' and M' increased. Conventionally the high frequency (early time) values of L' and M' are used to analyze experimental results. The justification for using the high frequency value of L' in Equation 1.1 is that for the 2-D railgun the high frequency limit of L' gives the correct armature force. This is discussed in the next chapter.

The high frequency value of L' has not been used by all railgun researchers for experimental performance evaluation. Hugh Calvin used the value of L' given at the breech of the gun the 2-D time dependent value of L' for experimental evaluation of the Thunderbolt experiments [22]. This resulted in using the low frequency value of L' for the majority of the shot evaluation. The justification was that by using the low frequency value of L' one correctly estimated the change in associated energy given by Equation 2.10.

The fundamental understanding of the dependencies of L' that has been presented here was used to design a higher inductance gradient railgun which, from Equation 1.6, should increase the armature force. The original transaugmented railgun design (now known as the low inductance gradient railgun), shown in Figure 2.1, was primarily designed for structural considerations. From the improved understanding of

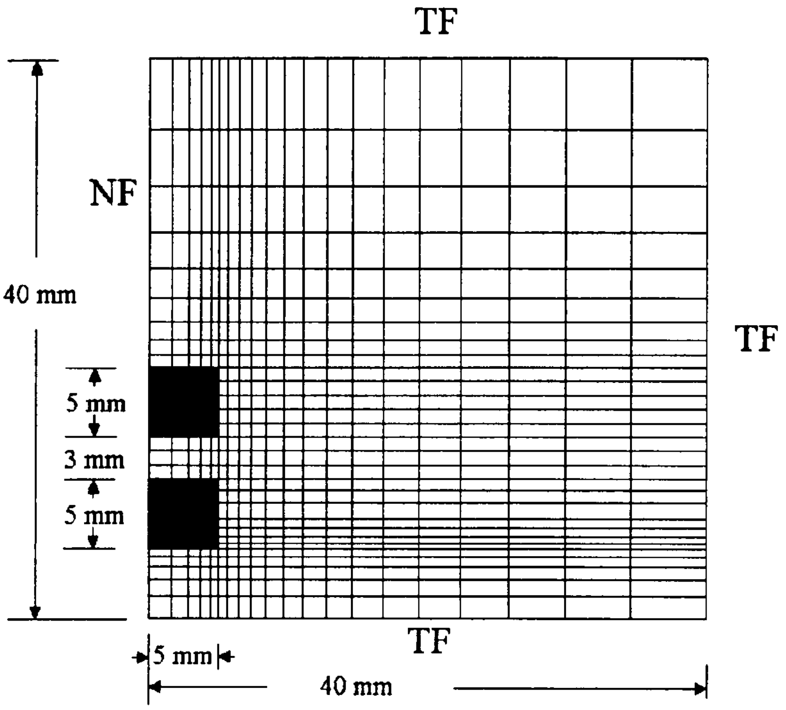

Figure 3.5. Cross section of generic square bore model.

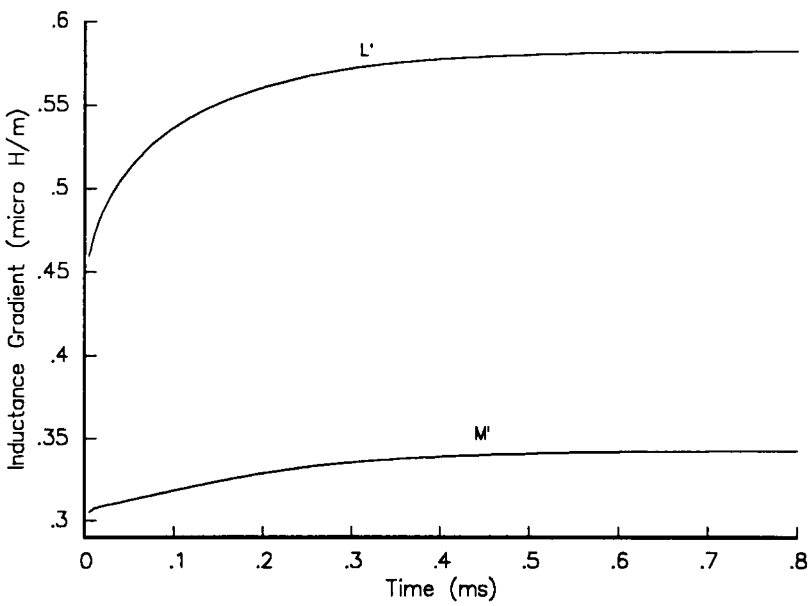

Figure 3.6. Time dependence of L' and M' for the generic square bore model.

L' Dr. Roger Crawford designed the UTSI high inductance transaugmented railgun shown in Figure 3.7. The value of L' and M' for the low inductance railgun was 0.274 and 0.249 μH/m respectively. For the high inductance railgun L' and M' were increased to 0.425 and 0.35 μH/m respectively. This gave an increase of approximately 50% in inductance gradients.

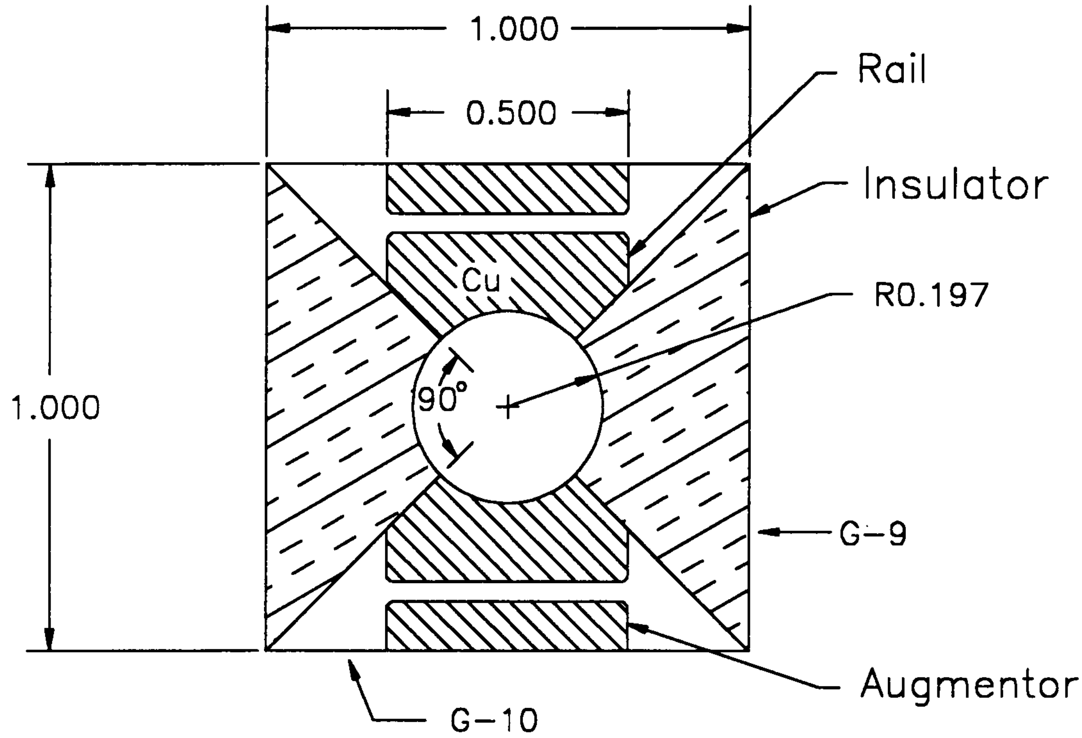

Figure 3.7. Cross section of the UTSI high inductance gradient railgun.

IV. 2-D RAILGUN SIMULATIONS

The primary reason for examining the 2-D railgun, as opposed to going directly to 3-D simulations, is that the armature force is known analytically and an infinite series solution has been obtained for the current distribution for both the moving and stationary armature case for a 2-D railgun. Since we have these known solutions the 2-D railgun is used to validate the 3-D MAP3 and MEGA formulations. (i.e. formulations that solve for the magnetic vector potential **A**, as opposed to the 2-D formulation which uses H_x.)

The 2-D railgun is also used to show how the inadequacies of the simple force model depend on the rail thickness, and that the simple electromagnetic force model does predict the total (armature plus rails) axial force. Good agreement between the simple electromagnetic force model and the total force can be achieved for the 2-D railgun since much finer meshing can be used in 2-D than in 3-D. This is due to computer memory limitations.

In the first half of this chapter 2-D railgun simulations are used to show that Equation 1.1 does not give the correct armature force when the rails have a finite thickness. Two 2-D railguns were analyzed with MEGA were each had a different rail thickness. The axial armature force and total force were then calculated by integrating **JxB** separately over the armature and the rails. The time dependent total axial force was then compared with Equation 1.1 where L' was calculated from a 2-D cross section of the rails. The known analytical armature force for the 2-D railgun was also used for comparison.

As noted in the previous chapter, 2-D railgun simulations take place in the yz-plane and 2-D cross section simulations take place in the xy-plane. The 2-D cross section simulations are performed using the variable A_z, as discussed in Chapter III, and the 2-D railgun simulations are performed using the variable H_x. The equations used in MEGA's 2-D **H** formulation are given in this chapter.

In the second half of this chapter results from MEGA and MAP3's simulation of a 2-D railgun are compared. MAP3 is a 3-D electromagnetic finite difference code developed by Dimitri Kondrashov at UTSI [31]. MEGA and MAP3's 3-D formulations were used to model a 2-D railgun, since there is a known analytical expression for the armature force in this case. The magnetic field and current distributions are also known as a function of time for the 2-D railgun. This serves as a standard to determine the accuracy of the 3-D numerical simulations.

4.1. 2-D Railgun Investigation Using MEGA's 2D H Model.

A 2-D railgun consists of infinitely wide rails and armature. All the **H** field is trapped inside the bore with a single component into the page, H_x , that is constant throughout the bore. The **H** decreases to zero outside the rails and armature as shown in Figure 4.1.

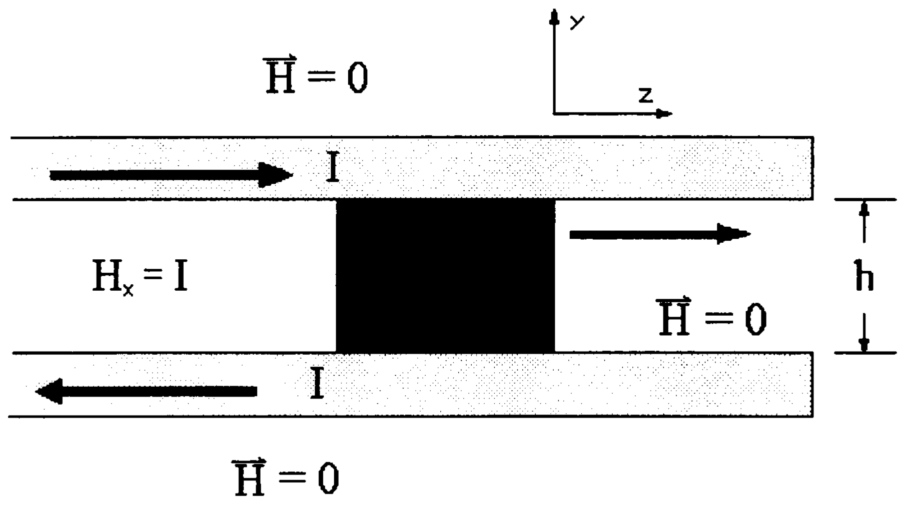

Figure 4.1. Diagram of a 2-D railgun.

Using,

$$\mathbf{J} = \nabla \times \mathbf{H} \quad , \tag{4.1}$$

the integral of **J** over a cross section of the rail or armature yields I per unit width. To find the current passing through the armature one would take the integral of J_y over the surface of the armature with the unit normal **y**. For this restricted 2-D case Equation 4.1 gives, $J_y = \partial H_x/\partial z$, and the current per unit width is,

$$I = \int_0^l \frac{\partial H_x}{\partial z}\, dz = H_x \, , \tag{4.2}$$

where the integral is taken from the back surface of the armature, 0, to the front surface of the armature, *l*, where *l* is the armature length.

The Maxwell stress tensor gives the stress transmitted across an element of area whose positive normal is **n**. To find the force on a given volume, the integral of the Maxwell stress tensor over the surface bounding the volume,

$$\oint_S \left[\frac{1}{\mu_o} (\mathbf{B} \cdot \mathbf{n}) \mathbf{B} - \frac{1}{2\mu_o} \mathbf{B}^2 \mathbf{n} \right] dS = \int_V \mathbf{J} \times \mathbf{B} \, dV , \tag{4.3}$$

can be used [32]. For the 2-D railgun we are interested in the force in the **n** = **z** direction. This requires evaluating the first term over all sides of the volume and the second term over the front and back of the armature, since these two surfaces are the only ones with a unit normal **z**. Since there is only a B_x component of magnetic field, the first term in Equation 4.3 goes to zero. The second term evaluated over the front of the armature is zero, since B_x is zero, and over the back surface it changes sign since the unit normal there is **-z**. Equation 4.3 is reduced to,

$$F_z = \frac{1}{2\mu_o} \int_S B_x^2 \, dS , \tag{4.4}$$

for a 2-D railgun where the integral is taken over the rear surface of the armature. Taking the integral over a unit width and using $B_x = \mu_o H_x$, and the result of Equation 4.2, $H_x = I$, one obtains,

$$F_z = \frac{1}{2} (\mu_o h) I^2 , \tag{4.5}$$

where h is the height of the bore, Figure 4.1. Equation 4.5 gives an analytical expression for the armature force. For the 2-D railgun the armature force is independent of the rail thickness, current distribution, armature velocity, etc.. It is only dependent upon the bore height and total rail current.

For Equation 4.5 to equal Equation 1.1, L' would have to be equal to $\mu_o h$. In Chapter III L' was obtained from

$$\frac{1}{2} L I^2 = \frac{1}{2\mu_o} \int_\infty B^2 \, d\tau \ , \tag{3.2}$$

where the volume integral is taken over all space. If there is no magnetic field in the rails $\mathbf{B}^2$ can be taken outside the integral since it is constant inside the bore. Again using $B_x = \mu_o H_x$, and taking only the integral of a unit width gives

$$\frac{1}{2} L I^2 = \frac{1}{2} \mu_o H_x^2 \int dy \, dz \ . \tag{4.6}$$

The integral of dy yields h, the height of the bore, and the integral of dz is taken over a unit length in the z-direction. Using the result of Equation 4.2, $H_x = I$, and taking the integral of Equation 4.6 and dividing by the unit length in the z-direction yields,

$$\frac{1}{2} L' I^2 = \frac{1}{2} \mu_o h I^2 \ , \tag{4.7}$$

where L' is the self inductance per unit length in the z-direction. So Equation 4.5 equals Equation 1.1 for the case where the magnetic field is confined to the bore of the railgun. This occurs at early time before the magnetic field can diffuse into the rails or for the high frequency limit.

The magnetic field diffusion into the rails does not affect the magnetic field inside the bore, thus it does not affect the armature force. However, due to the definition of L', Equation 3.2, the value of L' increases since the integral on the left side of Equation 3.2 must increase. It must increase since the part due to **B** inside the bore remains the same, and there is an additional part due to **B** inside the rails. Equation 1.1 overpredicts the armature force when the field diffuses into the rails, since L' increases as the magnetic field diffuses, while the armature force remains constant.

In MEGA's 2-D **H** formulation for a 2-D railgun with a stationary armature the equation,

$$-\frac{\partial^2 H_x}{\partial x^2} + \frac{\partial \mu H_x}{\partial t} = 0 , \tag{4.8}$$

is solved. If the armature is in motion Equation 4.8 is modified to include a velocity dependent term

$$-\frac{\partial^2 H_x}{\partial x^2} + \frac{\partial \mu H_x}{\partial t} + v_z \mu \frac{\partial H_x}{\partial z} = 0 . \tag{4.9}$$

In this formulation the boundary conditions are set at the rail and armature surfaces. From Figure 4.1, one would set the value of $H_x = I$ on the rail and armature surfaces inside the bore, and $H_x = 0$ on the surfaces outside the bore.

Two specific 2-D railguns were solved with MEGA's 2-D **H** formulation. Each had an armature length of 0.5 cm, a bore height of 1 cm, and a current per unit width of 100 kA/m. One had a rail thickness of 0.3 cm. The other had a rail thickness of 2.5 cm.

In each case MEGA was used to determine the time dependent value of L'. This was done by solving the 2-D field diffusion in the cross section of each railgun. As stated in Chapter II, this is done using the variable A_z. A time dependent plot of Equation 1.1 for each case is given in Figure 4.2. As the field diffused into the structure there was more magnetic flux in the domain for the thicker rails. Therefore for the thicker rails the fully diffused value of L' was greater than for the thin rails.

For the thinner rails the value of the force as calculated with Equation 1.1, was 19% greater for the fully diffused case than the true armature force given by Equation 4.5. For the thicker rails the difference between Equation 1.1 and Equation 4.5 continues to grow as the field diffuses into the rail.

The armature force calculated by integrating **JxB** over the armature volume in MEGA's 2-D **H** model is exactly equal to the analytical force given by Equation 4.5. Unfortunately this is strictly due to the way the boundary conditions are applied to the problem and the fact that linear finite elements are used. The H_x distribution could be in complete error and the armature force would still be calculated exactly.

From the 2-D railgun calculations it was found that the total axial force, as calculated from **JxB** over the rails and armature, was equal to Equation 1.1. In Figure 4.3 the time dependent value of Equation 1.1 (Figure 4.2) is plotted with the total force from the 2-D railgun calculations. For the rail thickness of 0.3 cm the total calculated axial force was 0.047% larger than that predicted by Equation 1.1 at 1 ms, where L' was also calculated by MEGA. This difference is quite small and can be attributed to roundoff errors, so that the two values are essentially the same. For the

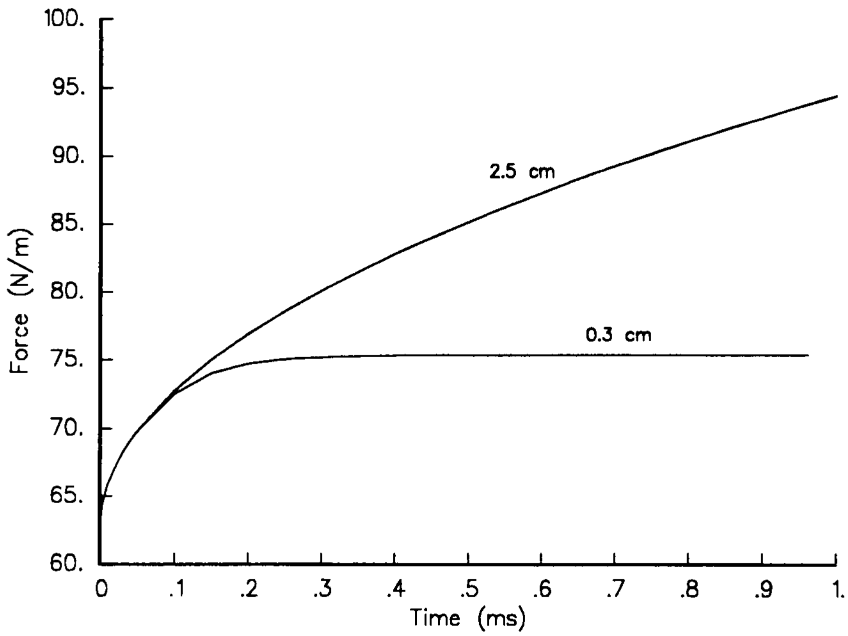

Figure 4.2. Equation 1.1 evaluated with time dependent value of L'.

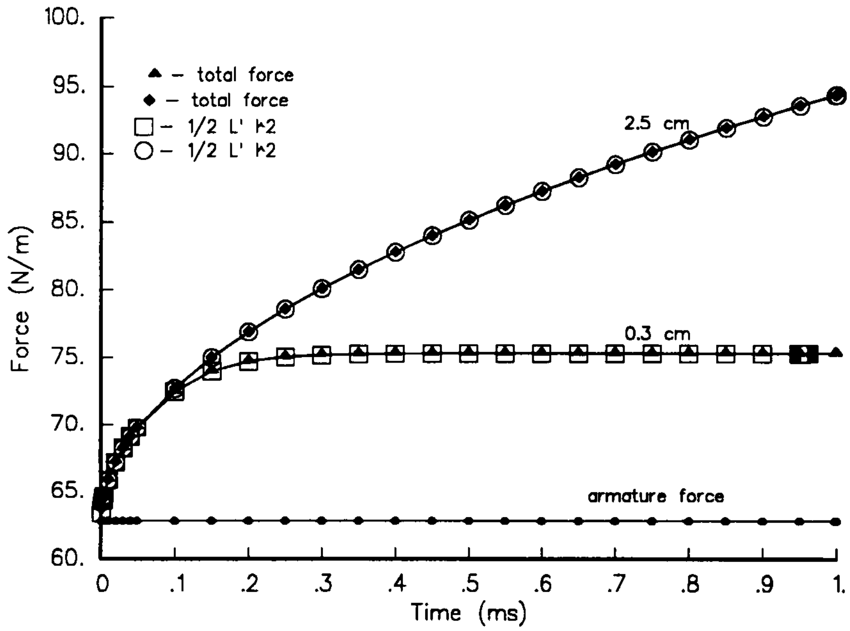

Figure 4.3. Equation 1.1 compared with the total force in the 2-D railgun.

rail thickness of 2.5 cm the total calculated axial force was 0.053% larger than that predicted by Equation 1.1 at 1 ms, where L' was also calculated by MEGA. Again, the difference is quite small, and Equation 1.1 is essentially equal to the total calculated axial force. The differences were the same for a stationary armature and for one moving at 20 m/s. An armature velocity of 20 m/s was used since for this velocity the field diffusion at the breech is essentially the same as it is for a 2-D cross section. (i.e. for 20 m/s the velocity skin effect does not keep the magnetic field from diffusing at the breech.)

In summary, with the 2-D railgun the high frequency value of L', $[L'(t \to 0)]$, used in Equation 1.1 predicts the correct armature force. In the high frequency limit there is no magnetic field diffusion into the rails. This implies that in Equation 4.5 $\mu_o h$ is equal to the high frequency value of L'. This is the justification many researchers give for using the high frequency value of L' in Equation 1.1.

For the fully diffused case with thicker rails Equation 1.1 becomes more inaccurate. For the 2-D railgun Equation 1.1 predicts the total axial force. This is significant, since even in the 2-D railgun eddy currents exist due to the motion of the armature. The fact that Equation 1.1 predicts the total axial force does not answer all the questions about its derivation with the use of power conservation arguments. Knowing the amount of axial force exerted in the rails does not tell us how much energy is dissipated due to eddy current generation or how much goes into strain energy in the structure. This is still an unresolved question.

4.2. Evaluation of MEGA's and MAP3's 3D Formulations.

The armature force for a 2-D railgun is known analytically as was shown in the previous section in Equation 4.5. An infinite series solution for the magnetic field intensity in a 2-D railgun with constant velocity has also been obtained by G. C. Long [33]. These results are used in this section to evaluate MEGA and MAP3's 3-D formulations. In the 3-D formulations the armature force is not directly dependent upon the boundary conditions as it was for MEGA's 2-D **H** model. The 3-D formulations are evaluated by solving a 2-D slice with appropriate boundary conditions so that the model is identical to a 2-D railgun. These results are then compared to the known solutions for the 2-D railgun.

In both MEGA and MAP3 the magnetic vector potential **A** is used instead of the magnetic induction **B**. MAP3 also solves for the electric scalar potential V. MEGA has numerous formulations for the stationary armature case. Some of the formulations solve for **A** and V, others use a penalty term to assure the divergence of **A** is zero, etc.. Only one of these formulations has been extended to the case of a moving armature. It is this formulation that is presented here and used throughout the dissertation.

To obtain the formulations used in the two codes one starts with a subset of Maxwell's equations:

$$\nabla \times \mathbf{H} = \mathbf{J} \tag{4.1}$$

$$\nabla \times \mathbf{E} = -\frac{\partial \mathbf{B}}{\partial t} \tag{4.12}$$

$$\nabla \cdot \mathbf{B} = 0 \tag{4.13}$$

$$\nabla \cdot \mathbf{E} = 0 \, . \tag{4.14}$$

In Equation 4.1 the displacement current has been assumed zero, and in Equation 4.14 charge neutrality has been assumed. Both codes solve for the magnetic vector potential **A** which is related to **B** by

$$\mathbf{B} = \nabla \times \mathbf{A} \, . \tag{3.4}$$

Any **B** found from **A**, as defined by Equation 3.4, will have zero divergence from the vector identity $\nabla \bullet \nabla \times \mathbf{A} = 0$, satisfying Equation 4.13. Equation 4.12 and Equation 3.4 are combined to obtain

$$\nabla \times \mathbf{E} = -\frac{\partial}{\partial t} \nabla \times \mathbf{A} \, ,$$

or

$$\nabla \times \left(\mathbf{E} + \frac{\partial \mathbf{A}}{\partial t} \right) = 0 \tag{4.15}$$

This means that the quantity in parentheses can be written as the gradient of some scalar function,

$$\mathbf{E} + \frac{\partial \mathbf{A}}{\partial t} = -\nabla V$$

or (4.16)

$$\mathbf{E} = -\frac{\partial \mathbf{A}}{\partial t} - \nabla V ,$$

where V is the electric scalar potential [34]. An equation involving the curl of **A** is now derived. First Equation 3.4, and the relation $\mathbf{B} = \mu\mathbf{H}$, is used to express **H** in terms of **A**, $\mathbf{H} = 1/\mu \; \nabla \times \mathbf{A}$. Ohm's law, $\mathbf{J} = \sigma\mathbf{E}$, is then used in conjunction with Equation 4.16 to express **J** in terms **A** and V. The expressions for **H** and **J** in terms of **A** and V are then substituted into Equation 4.1 to yield

$$\nabla \times \frac{1}{\mu} \nabla \times \mathbf{A} + \sigma \left(\frac{\partial \mathbf{A}}{\partial t} + \nabla V \right) = 0 . \tag{4.17}$$

The divergence of **J** ,

$$\nabla \cdot \mathbf{J} = \nabla \cdot \sigma \left(\frac{\partial \mathbf{A}}{\partial t} + \nabla V \right) = 0 . \tag{4.18}$$

is solved simultaneously with Equation 4.17 in MAP3 to obtain values for **A** and V.

In the case where there is velocity the term in parentheses in Equations 4.17 and 4.18 is modified to

$$\frac{\partial \mathbf{A}}{\partial t} + \nabla V + v \times \nabla \times \mathbf{A} . \tag{4.19}$$

MAP3 also has the capability to solve directly for the steady state case for both moving and non moving parts. This is a different formulation of the problem and is used as a check to the long time, steady-state, solution of Equations 4.17 and 4.18.

The steady-state formulation involves setting the partial derivative of **A** with respect to *t* equal to zero in Equations 4.17, 4.18 and 4.19 for the case with moving parts.

Once **A** and V are obtained from Equations 3.4 and 4.16 **E** and **B** can be obtained. The boundary conditions used in MAP3 are the same as those used in MEGA and are given after the MEGA formulation is presented.

For the time dependent stationary armature case MEGA solves the single equation,

$$\nabla \times \frac{1}{\mu} \nabla \times \mathbf{A} + \sigma \frac{\partial \mathbf{A}}{\partial t} = 0 \,. \tag{4.20}$$

Equation 4.20 is similar to Equation 4.17 except that ∇V has been assumed to be zero. Equation 4.20 has several limitations. It cannot handle the jump in V at the interface between two materials of different conductivity, since ∇V has been assumed to be zero [35]. For this reason all simulations performed with MEGA in this dissertation use a constant conductivity throughout the computational domain. The conductivity of copper was chosen for the simulations. Note that the magnitude of the conductivity only changes the diffusion rate, it does not change the physics.

Equation 4.20 is also incapable of solving for the steady-state solution. To demonstrate this consider a railgun where a constant current has been applied to the breech. Once the fields have fully diffused than the $\partial \mathbf{A}/\partial t$ will be equal to zero. From Equation 4.20 the $\partial \mathbf{A}/\partial t$ equal to zero would imply that the first term must equal to zero. However, the first term is equal to **J** implying the current density is equal to zero. This is not the correct solution. The current is being force at the breech, so **J** is not zero. This implies Equation 4.20 cannot solve for the steady-state case. In the MEGA formulation Equation 4.18, the divergence of **J** equal to zero is not solved directly. Therefore current continuity is not ensured in the MEGA formulation.

For the case with moving parts Equation 4.20 is modified to

$$\nabla \times \frac{1}{\mu} \nabla \times \mathbf{A} + \sigma \left(\frac{\partial \mathbf{A}}{\partial t} + \mathbf{v} \times \nabla \times \mathbf{A} \right) = 0 \,. \tag{4.23}$$

In regions with no current sources, $\sigma = 0$, MEGA uses the magnetic scalar potential. In these regions Equation 4.10 reduces to $\nabla \times \mathbf{H} = 0$ and **H** can be expressed as $\nabla\psi$. A set of conditions are then applied at the interface between the conducting and non-conducting material. A complete discussion of these conditions is out of the scope of this dissertation. The interested reader is referred to Reference 29.

The boundary conditions for MEGA and MAP3 are identical. In general, on each boundary each component of **A** is either set to zero or its derivative with respect to the normal of that boundary is set to zero. As an example consider the boundary with the unit normal **z**. If tangent flux is specified, $B_z = 0$, then A_x and A_y are set to zero, and the partial derivative of A_z with respect to z is set to zero. If normal flux is specified, B_x and $B_y = 0$, then A_z is set to zero and the partial derivatives of A_x and A_y with respect to z are set to zero. These conditions were obtained from Equation 3.4.

Other than the differences in formulation and the basic difference that MEGA uses the finite element technique and MAP3 uses the finite difference technique for their formulations, MAP3 also uses a staggered grid to specify **E** and **B**. This is of extreme importance in determining how upwinding is done in the case of moving parts. Details of the staggered grid method, and MAP3 in general, will be presented in a paper by Dimitri Kondrashov at a later date [31].

MEGA and MAP3 were both used to solve a 2-D slice using their 3-D formulations. The 2-D slice was similar to Figure 4.1 with a width of 1 cm. The armature length was 1 cm with a height of 1 cm. The rail thickness was 0.5 cm. Exact coordinates of the nodes are given in Appendix B.

The two yz-plane boundaries were set to have normal flux, so that there was no current flow in the x-direction. The other four boundaries were set with the tangent flux boundary condition. A step current input of 50 kA was then applied to the breech end of the rails.

In MAP3 the steady state formulation was used and the armature force was calculated by integrating **JxB** over the armature volume. The analytic solution of the 2-D railgun armature force of Equation 4.5 was scaled for a unit width of 1 cm. A time dependent armature force was then obtained by MEGA. The results for a stationary armature are shown in Figure 4.4. MAP3 underpredicted the true armature force by 1.6%. At steady state MEGA underpredicted the armature force by 2.2%. At early time MEGA's predictions are even more in error. This has to do with inaccuracies encountered before the field has diffused completely through the first element on the back surface of the armature. The finite element method assumes a linear solution in the each element and until the field fully diffuses through the element this is a not a good approximation.

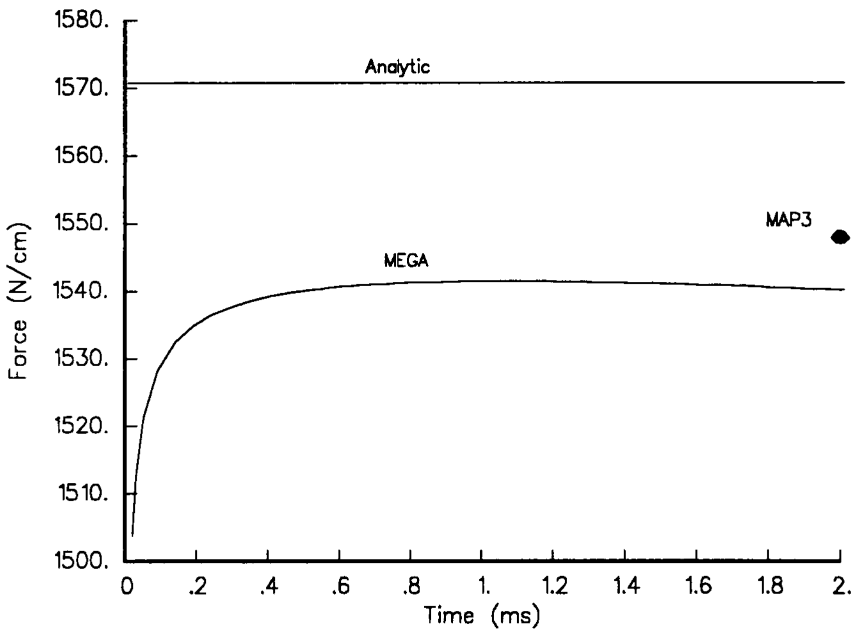

Figure 4.4. The 2-D railgun stationary armature force from the analytic expression, MEGA's **A**-ψ formulation, and MAP3's **AV** steady state formulation.

With velocity effects included the armature force predicted by MEGA at 2.0 ms was identical to the steady state solution of MAP3, see Figure 4.5. As previously noted, the particular solution method MEGA uses has difficulty reaching an absolute steady state. The solution after the field has been known to fully diffuse into the breech of the rails cannot be trusted. So the comparison of MEGA and MAP3 at steady-state is not completely appropriate. Both MEGA and MAP3 underpredicted the armature force at this time by 3.5%.

Comparisons of the armature forces did not reveal whether one code gave more accurate results than the other. The current distributions of MAP3, however, appear to be more accurate than those of MEGA. Figure 4.6 is a vector plot of the current density. In the rails at the rear of the armature, circled and labeled region 1 in Figure 4.6, the circulating current is incorrect. Also there should be nearly zero current flow in the rails in front of the armature and no negative flow of current in the armature itself, see region 2 in Figure 4.6 [33]. MAP3 does not predict these anomalous current densities, Figure 4.7.

The comparison between MAP3 and MEGA did not fully resolve whether one code was more accurate than the other in predicting the armature force. From an examination of the current densities it was determined that MAP3 did a better job of predicting current densities. Since MAP3 does more accurately model the magnetic field and current distributions, when there are discrepancies between the codes preference will be given to the MAP3 predictions.

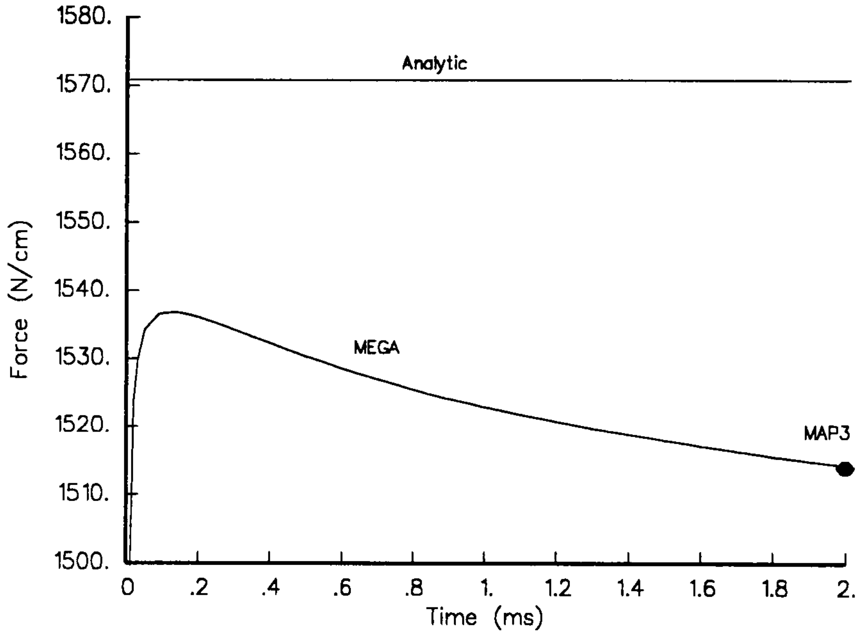

Figure 4.5. The 2-D railgun armature force from the analytic expression, MEGA's **A**-ψ formulation, and MAP3's **A**V steady state formulation with an armature velocity of 500 m/s.

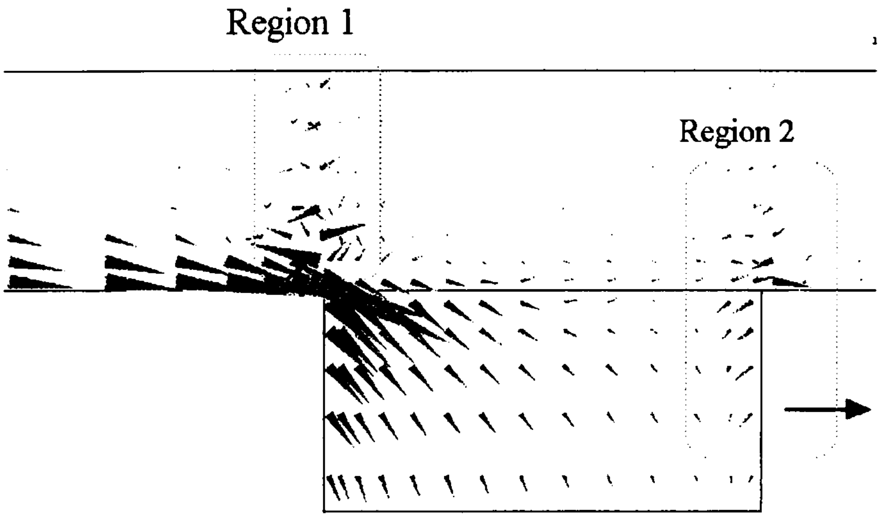

Figure 4.6. Plot of current density for the 2-D railgun with moving armature using MEGA's 3D **A**-ψ formulation.

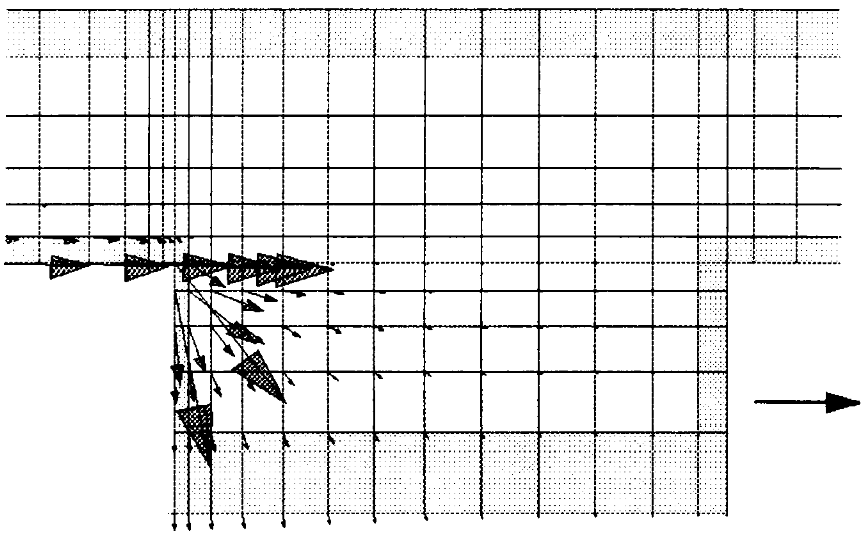

Figure 4.7. Plot of current density for 2-D railgun with moving armature using MAP3's 3D **AV** formulation.

V. INVESTIGATION OF A GENERIC SQUARE BORE RAILGUN WITH MEGA AND MAP3.

Assumptions made for the derivation of the simple electromagnetic force model have been examined along with the dependencies of L' and M'. It has also been shown that for a 2-D railgun the high frequency value of L' in Equation 1.1 provides a good estimate for the axial armature force. In 3-D this is not the case. The question still remains as to how accurate are the assumptions that were made in the power argument. To examine these assumptions it will first be shown that one must use full 3-D simulations.

Simulations were performed with MEGA for a 3-D generic square bore railgun, in conventional, transaugmented and muzzle-fed configurations. A square bore geometry was chosen to accommodate the limited gridding capabilities of MAP3. MAP3 was used to simulate the conventional railgun with both stationary and moving armature on the same grid as MEGA. This was done to help validate the 3-D results.

The armature force for each configuration, calculated with the integral of **JxB** over the armature region, was compared with the appropriate electromagnetic force model. For the muzzle-fed case current and magnetic field distributions were examined to explain the large deviation in calculated armature force.

A modification of the simple electromagnetic force equations for the muzzle-fed and transaugmented configurations is proposed. Parameters needed for the modification are obtained from the muzzle-fed and transaugmented simulations with inner and outer rail currents equal. They are then validated with simulations where the inner and outer rail currents are not equal.

5.1. Differences Between the 2-D and 3-D Railguns.

Results from the 2-D railgun simulations show that using the high frequency value of L' in Equation 1.1 would yield the correct axial armature force. For the 2-D railgun the magnetic field remains constant in the bore and zero outside the bore no matter what the current distribution is in the rails and armature, as shown in Figure 4.1. In a 3-D railgun the magnetic field outside the rails and armature change as the current distribution changes. If the force is expressed in terms of the Maxwell stress tensor, Equation 4.3, then the value of **B** is required only on the surfaces of the armature. Even in the case of high velocity, where the velocity skin effect would limit the current to the surfaces of the rails in the vicinity of the armature, the magnetic field around the armature would be different than for the case of a stationary armature at early time for a step current input.

In 3-D there is also the possibility for eddy currents in the xy-plane, the cross section of the rails, and in the xz-plane. In the 2-D railgun there was only the possibility of eddy currents in the yz-plane. Eddy currents in the yz-plane act to redistribute the current, thereby increasing the total resistance as seen from the breech. It is important to think in terms of what happens to the power at the breech, since in the power argument, power was conserved at the breech of the gun. It is conceivable that eddy currents which circulate in the xy and xz-planes dissipate energy that is not accounted for at the breech. It was previously noted that the axial force exerted in the rails cause strain energy in the structure that is not accounted for at the breech in the power argument.

One also has the possibility of railguns with multiple rails. It is for the multiple rail railguns, transaugmented and muzzle-fed, that the most significant deviation from the simple electromagnetic force model occurs. These configurations cannot be modeled in 2-D. In a 2-D model the magnetic field produced by the outer rail would have to diffuse through the inner rail before it could interact with the armature. In 3-D the magnetic field produced by the outer rail diffuses into and around the inner rail and immediately interacts with the armature.

For these reasons it was necessary to use 3-D models to investigate fully the assumptions made in the derivation of the simple electromagnetic force models.

5.2. Description of the 3-D Generic Square Bore Railgun.

The 3-D generic railgun consisted of a 1 cm square bore with a 1 cm long solid armature. A square bore was chosen since MAP3 is unable to model complex geometries. Conductivity of copper was used for the rails and armature. As shown in Chapter IV, MEGA cannot adequately handle a jump in conductivity. The rail thickness for both inner and outer rails was 5 mm. An air gap of 3 mm was set between the inner and outer rails for the transaugmented and muzzle-fed railgun. A complete description of the geometry and nodal coordinates are given in Appendix B. This is a different square bore railgun geometry than previously reported in Reference 10. The previous square bore grid had rail thicknesses of 3 mm and an air gap of 1.5 mm. It was important to make comparisons between MEGA and MAP3, since there were no analytical solutions to a 3-D problem similar to a railgun to validate MEGA's formulation.

In the process of making these comparisons an effort was made to accommodate MAP3 since it did not have a user-friendly gridding scheme. The square bore geometry and the resulting grid are presented here. (This was not a one step process, but evolved into the grid presented here.) The muzzle-fed and transaugmented railgun simulations were performed on the same grid for consistency.

The simulations were performed in the first quadrant using quarter symmetry. The symmetry boundary conditions applied were for tangent flux in the symmetry plane between rails, and normal flux in the symmetry plane between insulators. A description of the boundary conditions and how they were applied was given in Chapter IV.

Each of the MEGA simulations were carried out to a time of 600 μs. All the simulations used a timestep of 10 μs. To separate the effects of the transient current pulse and the armature motion, simulations were performed using a Helmholtz step function with an amplitude of 100 kA for the input current. Both stationary and constant velocity moving armature calculations were performed with the same input current. For the transaugmented railgun the same current input was used for both the armature and augmenting rail. Values of L' and M' were calculated from the 2-D cross section of the model using the same input current [15]. The time dependent values of L' and M' were given in Figure 3.6 and the geometry of the 2-D cross section in Figure 3.5. The values of L' and M' at 10 kHz were $L' = 0.49$ μH/m and $M' = 0.31$ μH/m. These are the typical high frequency values used for performance evaluation.

Simulations were also performed on a muzzle-fed railgun. The input current for inner and outer rails again had an amplitude of 100 kA and was a Helmholtz step function input. The time dependent values of L' and M' were the same as for the transaugmented railgun, since these values come from 2-D cross section simulations and are independent of the direction of current flow in the rails.

The value of L' for the conventional railgun, $L' = 0.51$ μH/m, was slightly higher than for the transaugmented case. This is because for the 3-D conventional railgun simulations an outer rail was not present. Without the presence of the outer rail the stored magnetic field energy over all space is greater at early time (high frequency) than when the rail is present.

A second set of simulations were performed on the muzzle-fed and transaugmented railguns with a stationary armature. For these simulations the inner rail current was 70 kA and the outer 140 kA. For the UTSI muzzle-fed railgun the inner and outer rail currents must be equal, since they are electrically connected, Figure 2.3. However it would be possible to have a muzzle-fed railgun where the inner and outer rails were powered separately as is the transaugmented railgun. These simulations were performed to validate the parameters found for the modified simple electromagnetic force equations.

5.3. The 3-D Generic Square Bore Simulations.

For the conventional railgun MEGA and MAP3 were both used to simulate the stationary and moving armature case. The axial armature force calculated by integrating **JxB** over the armature and how it compares to the simple electromagnetic force equation is the most important thing to examine in these simulations. The axial armature force is the armature force in the z-direction. The cross section of the 3-D railgun is in the xy-plane. The axial direction and rails are in the yz-plane. For each simulation with a constant velocity moving armature the armature force at steady state was compared to the simple electromagnetic force equation with L' and M' calculated at 10 kHz. These values of L' and M' were chosen since most researchers use the high frequency values of inductance gradients for their experimental performance evaluations.

A comparison of the total axial force, the integral of **JxB** over the entire computational domain, to the simple electromagnetic force is also of interest. In the 2-D railgun simulations these two quantities were equal. If they are equal in 3-D it explains where the force predicted by the simple electromagnetic force equations is exerted. It does not, however, determine what happens to the "associated energy" that does not go into mechanical work moving the armature.

Table 5.1 gives a summary of the electromagnetic armature force and total force calculated from the 3-D simulations of the conventional, transaugmented and muzzle-fed railguns. It also includes the force predicted by the respective simple force model for each configuration at 600 μs, and for L' and M' at 10 kHz. Column 8 is a comparison of the 3-D armature force at 600 μs to the simple force model with the 10 kHz values of L' and M'. Column 9 is a comparison of the 3-D armature force to the simple force model where both are obtained at 600 μs. Column 10 is a comparison of the 3-D total force to the simple force model where both are obtained at 600 μs. Table 5.1 is used as a reference as plots are presented for each railgun configuration of the time dependent 3-D armature force, the total force and the force calculated from the simple electromagnetic model.

The axial component of the **JxB** force was integrated over the armature and then over the total computational domain. Figure 5.1 shows the time dependent axial force for the armature and for the total computational domain, for both MEGA and MAP3, together with the force predicted by Equation 1.1. The total force calculated by MEGA and MAP3 closely approximated the force predicted by the simple electromagnetic force model. This result demonstrates that Equation 1.1 provides a good estimate for the total axial force, but not all of that force acts to accelerate the armature. It does not explain how the "associated energy", not going into the mechanical work of moving the armature, gets dissipated.

The armature force predicted by MAP3 at 600 μs, Table 5.1 column 6, was less than 1% greater than the armature force predicted by MEGA. MEGA and MAP3

Table 5.1. Summary of Electromagnetic Armature and Total Forces.

Railgun Type	Simple Elec 10 kHz (N)	Simple Elec 600μs (N)	Code	Arm. velocity (m/s)	3D Arm. Force 600μs (N)	3D Tot. Force 600μs (N)	3D Arm. 600μs / Sim elec 10 kHz (%)	3D Arm. 600μs / Sim elec 600μs (%)	3D Tot. 600μs / Sim elec 600μs (%)
conv	2550	2912	MEGA	0	2281	2872	89	78	99
				500	2573	2802	101	88	96
			MAP3	0	2296	2856	90	79	98
				500	2277	2749	89	78	94
trans	5550	6328	MEGA	0	4438	6290	80	70	99
				1000	4668	5812	84	74	92
muzzle	650.0	510.8	MEGA	0	-170.0	484.4	N/A	N/A	95
				1000	134.9	511.2	21	26	100

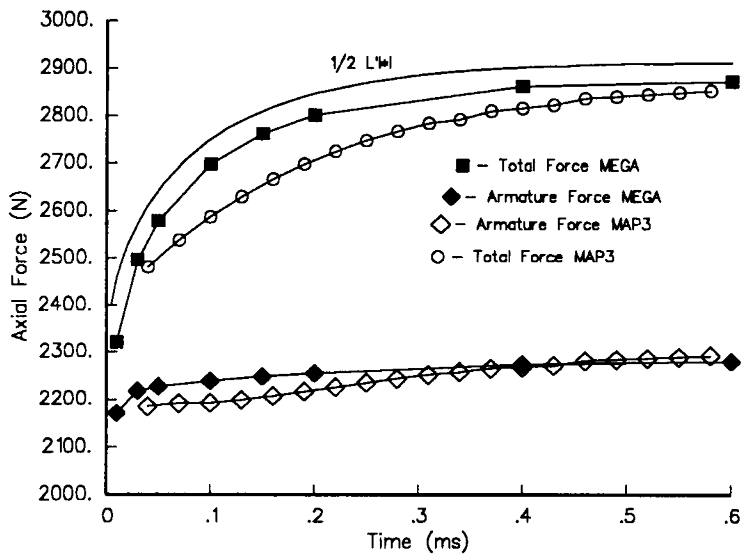

Figure 5.1. Comparison of MEGA and MAP3's predictions for the armature and total railgun axial forces for a conventional railgun with a stationary armature.

essentially predicted the same armature force as a function of time for the stationary armature simulation. This gives some confirmation that the codes are predicting the correct results, at least for non-moving parts.

The armature force predicted by MEGA at 600 μs was 78%, Table 5.1 column 9, of that predicted by Equation 1.1. If the value of L' at 10 kHz, 0.51 μH/m with no outer rail present, was used in Equation 1.1 the difference was reduced to 11%.

Figure 5.2 is a plot of the same forces from MEGA and MAP3 simulations of a conventional railgun with an armature velocity of 500 m/s. The steady state formulation of MAP3 was also used to solve this problem. The steady-state formulation was discussed in Chapter IV. The axial armature force predicted by the steady state formulation was the same as that obtained at 200 μs for MAP3, and was 2.5% below the armature force given by MAP3 with a stationary armature. (The solution using the steady-state formulation of MAP3 is not shown in Figure 5.2.)

The armature force predicted by MEGA with velocity at 600 μs was 12% greater than that predicted by MAP3 at steady state. MEGA did not conserve current in the rails directly behind the armature for the moving armature simulation. In Chapter IV several inadequacies of MEGA's velocity formulation were pointed out. Since MAP3 uses the current continuity equation in its formulation, Equation 4.18, it does conserve current for both the stationary and moving armature case. This was the only major difference in the comparisons between MEGA and MAP3.

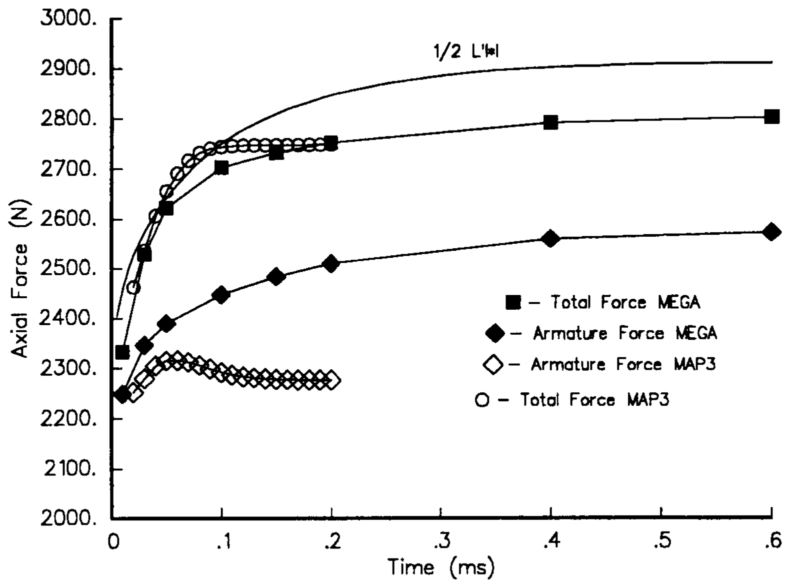

Figure 5.2. Comparison of MEGA and MAP3's predictions for the armature and total railgun axial forces for a conventional railgun with an armature velocity of 500 m/s.

To examine this difference, the current densities in the midplane between the insulators were plotted. Figure 5.3 shows the plane in which the current densities are plotted.

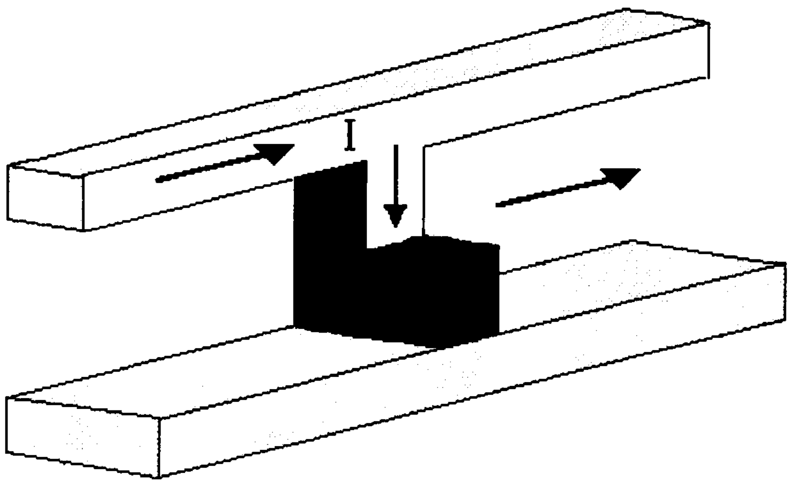

Figure 5.3. Conventional railgun showing the plane for which the current densities are plotted.

The current densities for the 3-D railgun from MAP3 and MEGA are similar to the predictions each gave for the 2-D railgun. Again, MEGA predicts what seems to be anomalous current densities in regions 1 and 2 of Figure 5.4. Figure 5.5 shows the current densities predicted by MAP3. It should be noted that before using the staggered grid method in MAP3, it also predicted these anomalous current densities and an armature force which increased with velocity. Since the current distribution predicted without the staggered grid is not correct, it is reasonable to conclude that the armature force for this case is also not correct.

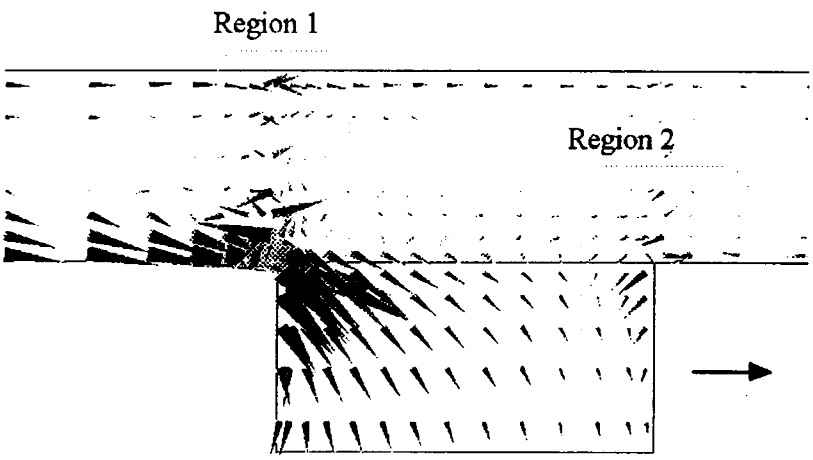

Figure 5.4. Current density for a conventional railgun at an armature velocity of 500 m/s at a time of 600 μs using a 3-D MEGA simulation.

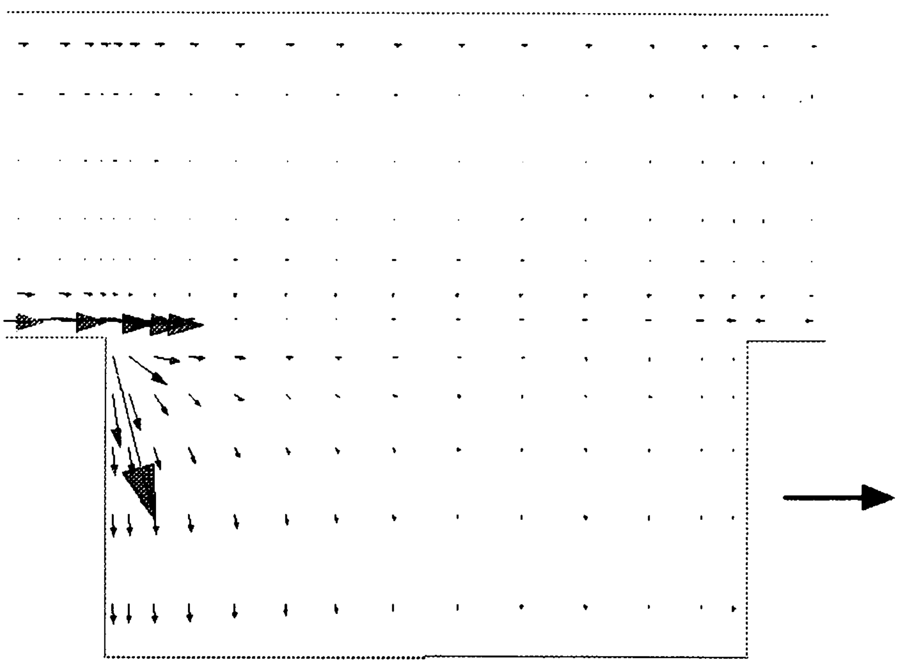

Figure 5.5. Current density for a conventional railgun at an armature velocity of 500 m/s at steady state using a 3-D MAP3 simulation.

The transaugmented railgun was simulated with MEGA on the same grid as was used for the conventional railgun simulations, Appendix B. The axial component of **J**x**B**, F_z, was again integrated over the armature and then over all the conducting material in the computational domain. This provided both the driving force on the armature and the total axial force in the computational domain. Figure 5.6 shows a plot of these forces along with the simple electromagnetic force for the transaugmented railgun, Equation 1.6. The forces in Figure 5.6 were for a stationary armature. The total force in the computational domain is in relatively good agreement with the simple electromagnetic force, as it was for the conventional railgun with a stationary armature.

The predicted armature force for the transaugmented railgun shows a much larger discrepancy with the simple electromagnetic force equation than it did in the conventional railgun. The armature force is 30% below that predicted by Equation 1.6 at 600 μs, Table 5.1 column 9. For the case of an armature moving at a fixed velocity of 1 km/s, Figure 5.7, the armature force is 26% below Equation 1.6 at 600 μs. The armature force for this case at 600 μs is 16% below that predicted using the 10 kHz values of L' and M' in Equation 1.6, Table 5.1 column 8.

Figure 5.8 and 5.9 show the armature and total axial forces for the muzzle-fed railgun for the stationary and 1 km/s fixed velocity armature cases respectively, together with the force predicted by Equation 2.3. For the stationary armature case the axial armature force predicted by MEGA is actually of the opposite sign of that predicted by the simple electromagnetic force model! The armature force at 600 μs is

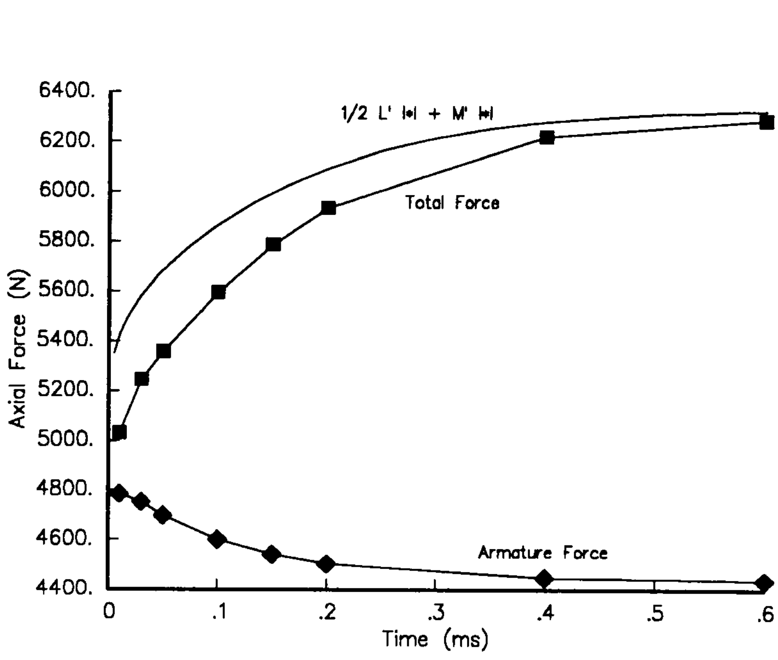

Figure 5.6. Armature and total railgun axial forces for a transaugmented railgun with a stationary armature using 3-D MEGA simulation.

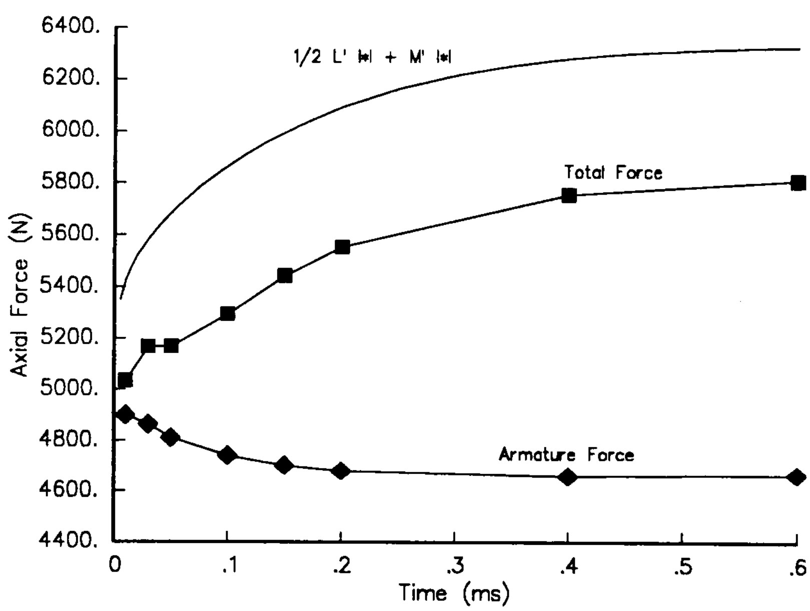

Figure 5.7. Armature and total railgun axial forces for a transaugmented railgun with an armature velocity of 1 km/s using 3-D MEGA simulation.

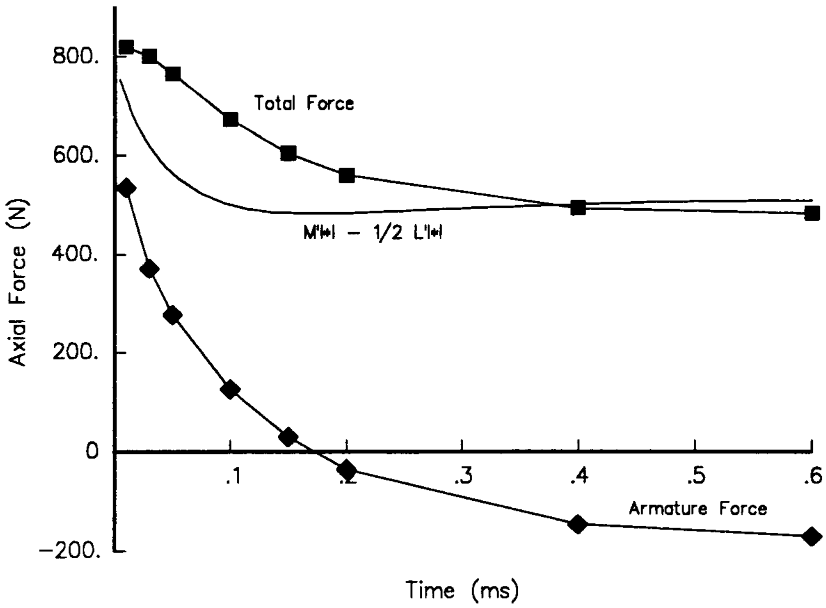

Figure 5.8. Armature and total railgun axial forces for a muzzle-fed railgun with a stationary armature using 3-D MEGA simulation.

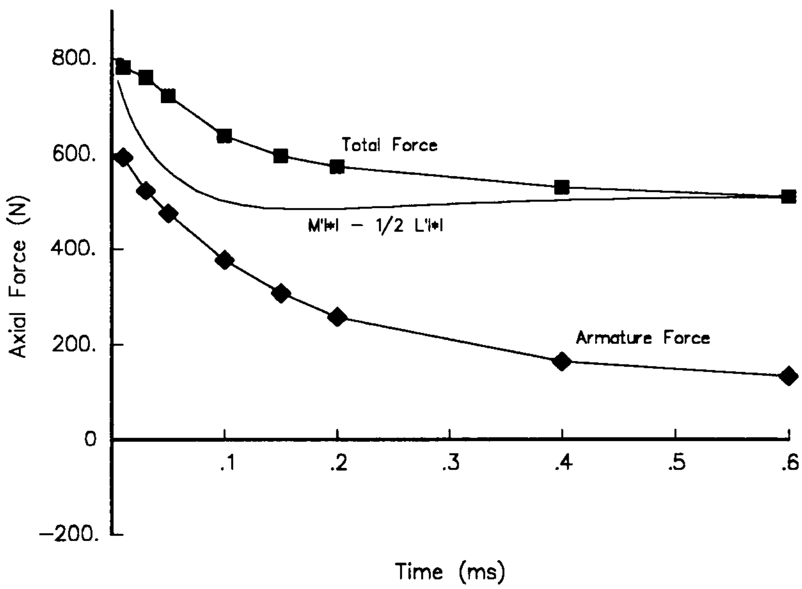

Figure 5.9. Armature and total railgun axial forces for a muzzle-fed railgun with an armature velocity of 1 km/s using 3-D MEGA simulation.

-170 N while the simple electromagnetic force equation predicts 510 N. This discrepancy is only made worse by using the high frequency values of L' and M', the early time value of Equation 2.3. These results are significantly worse than those predicted for the square bore muzzle-fed railgun with rail thicknesses of 3 mm [15], instead of the 5 mm used here. This gives some insight into the role that the rail thickness plays in determining the true armature force. The muzzle-fed railgun results are discussed in more detail in the following section.

5.4. Conclusions.

The 3-D generic square bore simulations show that the simple electromagnetic force models for each railgun configuration overestimate the true armature force. The overestimation is greater for the transaugmented railgun than for the conventional railgun. For the muzzle-fed railgun the simple electromagnetic force model actually predicts the force to be in the wrong direction. The magnitude of the force predicted by the simple electromagnetic force model was more than twice that predicted by the 3-D simulation. This shows Equation 2.3, the simple electromagnetic force model for the muzzle-fed railgun, cannot be used for experimental performance evaluation.

As time progresses, for the transaugmented railgun the magnetic field from the outer rails diffuse into the inner rails. This magnetic field interacts with the transverse component of current in the inner rails to produce an axial component of force in the rails significantly greater than in the conventional railgun case.

The total force for both the conventional and transaugmented railgun, predicted by MEGA for the stationary armature, is in relatively good agreement with the simple electromagnetic force model predictions. However, there is a discrepancy for the cases with a moving armature. This was examined in the 2-D railgun and it was found to be dependent upon the field diffusion at the breech of the railgun. The magnetic field does not fully diffuse at the breech of the railgun for the velocities examined, due to the velocity skin effect. Only for the case when the field at the breech of the railgun can fully diffuse (i.e. the breech approaches the behavior of a 2-D cross section simulation, with no variation in the z-direction) should the total force and simple electromagnetic force be in agreement.

The large error in the prediction of armature force in the muzzle-fed railgun using Equation 2.3 is again due to the diffusion of the outer rail field into the inner rail. At early time, Figure 5.10, the magnetic field from the outer rail has not diffused into the inner rail, and there is not a significant component of transverse current in the inner rail. As the fields diffuse, Figure 5.11, there is then a large transverse component of current, and the field produced by the outer rail can interact with this component. Taking the difference between the total force and armature force for the stationary muzzle-fed case, Figure 5.8, one finds that there is more axial force in the rails, 680 N, than force predicted by Equation 2.3, 510 N.

To understand why the armature force in the muzzle-fed railgun went negative, it is useful to examine the magnetic field at the center of the bore. Figure 5.12 shows the primary component of magnetic field, B_x, at different times as a function of the

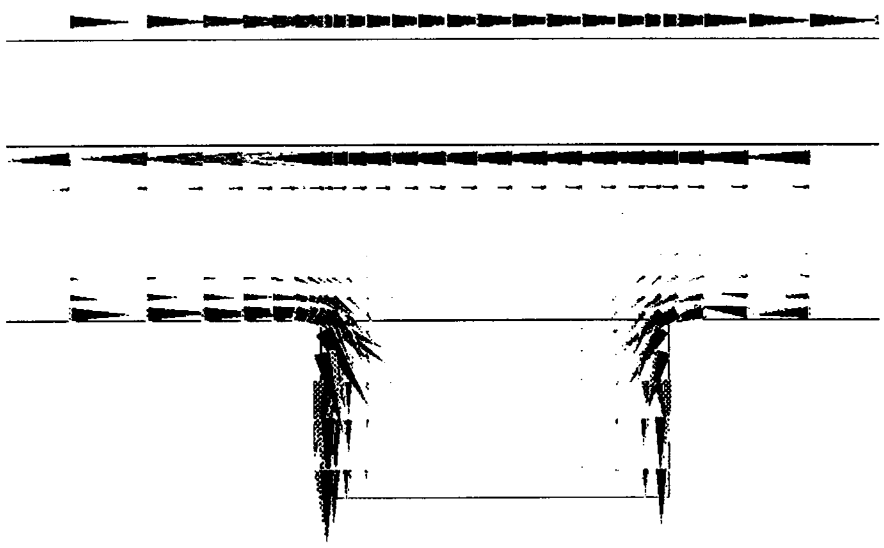

Figure 5.10. Current density for a muzzle-fed railgun with a stationary armature at a time of 10 μs using a 3-D MEGA simulation.

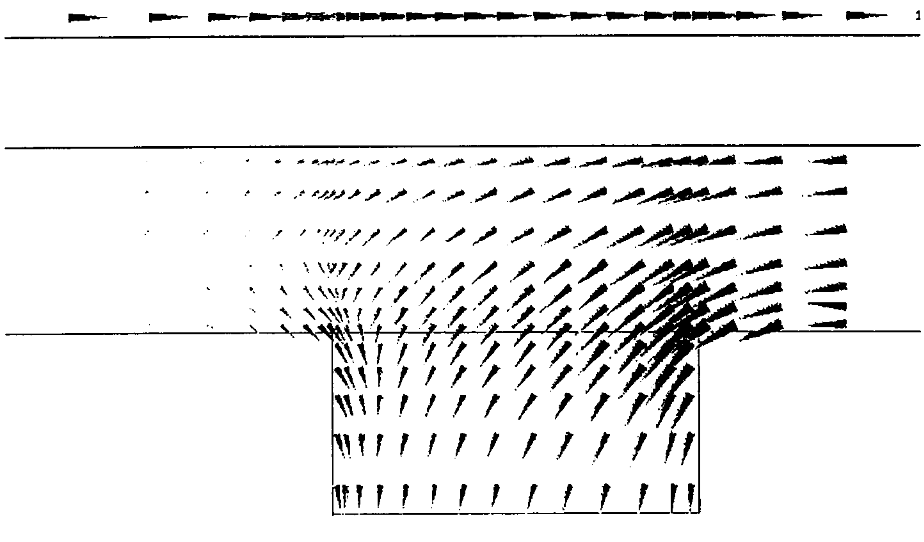

Figure 5.11. Current density for a muzzle-fed railgun with a stationary armature at a time of 600 μs using a 3-D MAP3 simulation.

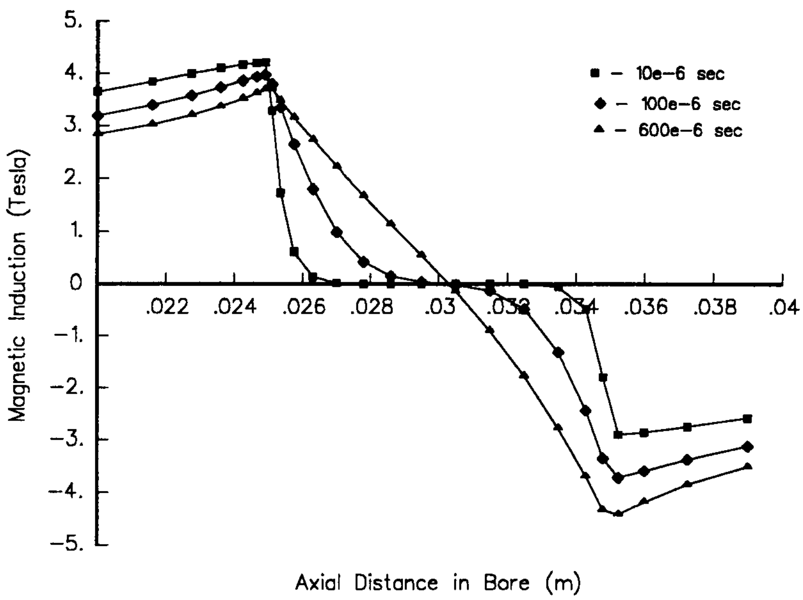

Figure 5.12. Magnetic induction at the center of the bore down the length of the gun.

axial distance down the center of the bore. As time progresses B_x in the rear of the armature, where the forward acceleration takes place, decreases by 8%. In front of the armature B_x increases negatively by 50% of its original value. The front of the armature is at 0.035 m in Figure 5.12.

The reason the magnetic field decreases at the rear of the armature and increases negatively in front of the armature can be explained in terms of eddy current generation due to field diffusion. At early time, Figure 5.10, the current density at the rear of the armature, on the inner surface of the rail and armature surface, is greater than at the front of the armature. This is due to the eddy current generated to oppose field diffusion into the rails. Since the current density on the inner surface of the rail is greater at early time than it is at late time, B_x is greater at earlier time. In front of the armature the same explanation is used but the effect is larger since both the inner and outer rail fields must diffuse in front of the armature, as opposed to only the outer rail field diffusion behind the armature.

The fact that B_x decreases by 8% behind the armature and increases negatively by 50% in front of the armature does not seem too significant until the current densities are also taken into account, which determine how the **JxB** force behaves. At early time, 10 μs, Figure 5.10 shows that the current density is greater at the rear of the armature. At late time, 600 μs, Figure 5.11 shows that the current density is greater towards the front of the armature where the field is negative. The armature force, **JxB** in the axial direction, at the center of the bore is plotted in Figure 5.13 as a function of axial distance in the armature. At the rear of the armature the positive

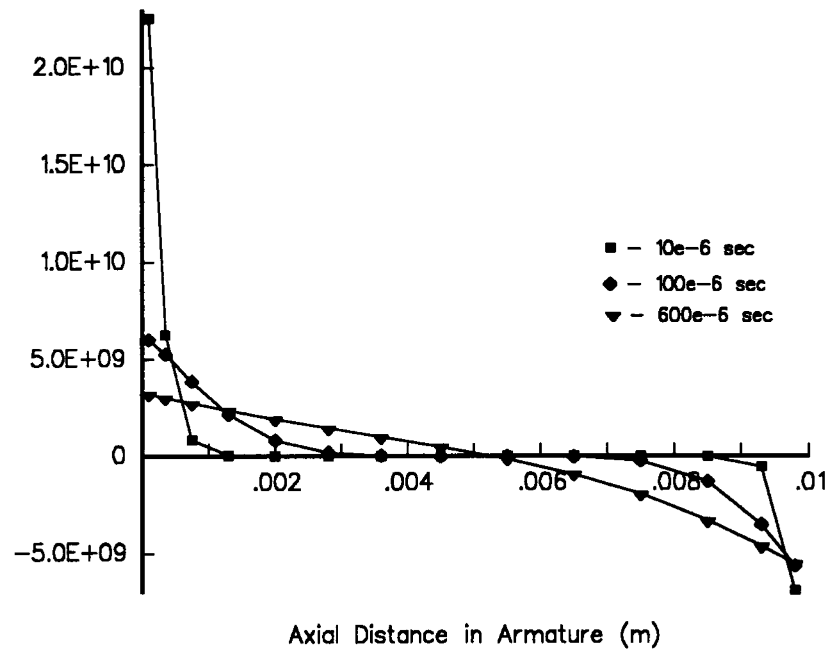

Figure 5.13. **JxB** at the center of the bore down the length of the armature.

force decreases by almost an order of magnitude from 10 μs to 600 μs. At the front of the armature it remains relatively constant. Integrating the force at 600 μs at this location over the length of the armature yields a negative force.

Figure 5.13 showed **JxB** at the center of the bore only. Figure 5.14 shows the average value of **JxB** in the xy-plane as a function of the axial distance in the armature. Figure 5.15 shows the integral of **JxB** as a function of the axial distance in the armature. (i.e. at the axial center of the armature, 0.005 m, the force plotted is the integral of **JxB** from the rear of the armature to the axial center of the armature. At 0.01 m the total armature force of -170 N is plotted.)

With a moving armature the muzzle-fed case produces a current density that is greater at the rear of the armature. Magnetic field must be diffused out of the rails in the region behind the armature as the armature moves. The current density is also greater at the rear of the armature for a conventional railgun with a moving armature. In the conventional case the field must be diffused into the rails which generates an eddy current that also increases the current density at the rear of the armature. Figure 5.16 shows the current density at 600 μs for an armature velocity of 1 km/s. Note the large eddy current in the region behind the armature. The current density is greatest in the rear of the armature at the armature rail interface. The moving armature case is different than the early time case with a stationary armature, Figure 5.10. With the moving armature there is a significant amount of transverse component of current in the rails. This explains why with the moving armature, at 600 μs, the armature force

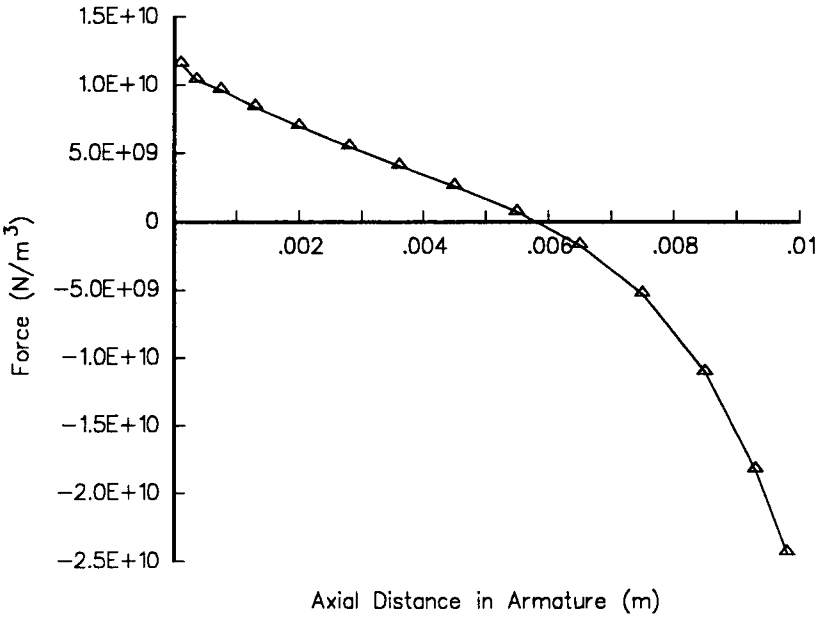

Figure 5.14. The average value of **JxB** in the xy-plane as a function of the axial distance in the armature.

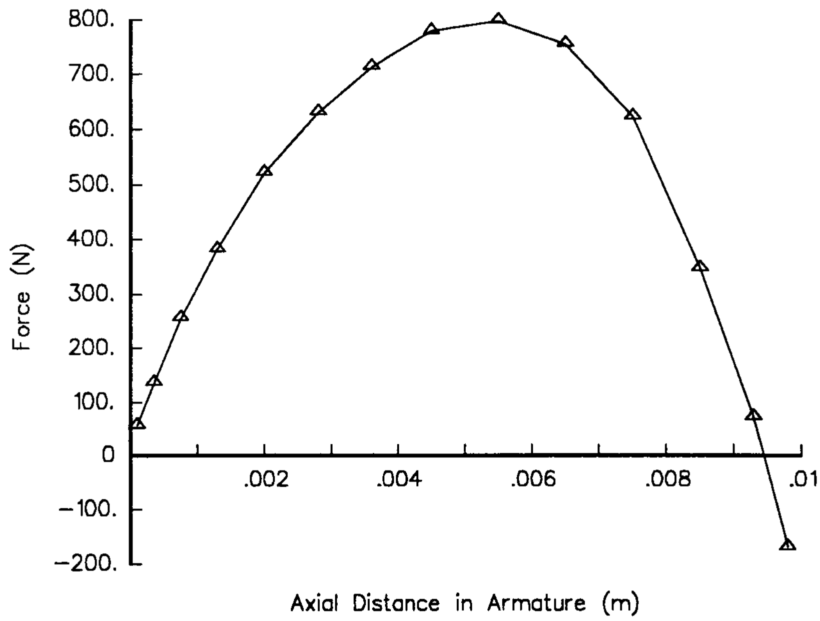

Figure 5.15. The axial force in the region from the rear of the armature to the axial distance in the armature indicated on the axis.

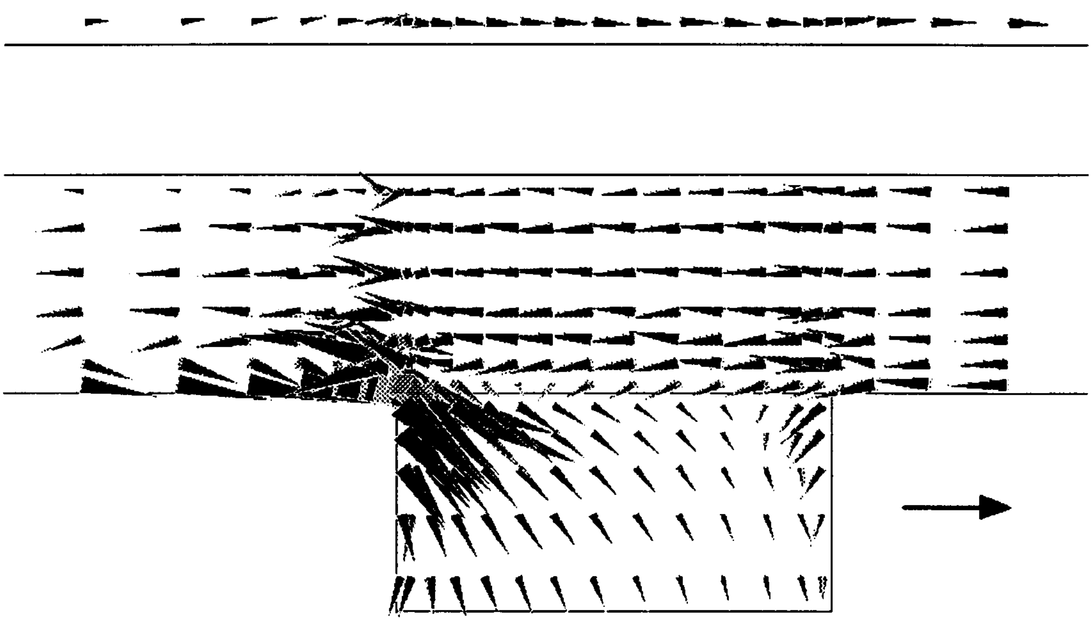

Figure 5.16. Current density for a muzzle-fed railgun with at an armature velocity of 1 km/s at a time of 600 μs using a 3-D MEGA simulation.

is 134 N, while it is over 500 N at early time for the stationary case, Figures 5.8 and 5.9.

5.5. Modification of the Simple Electromagnetic Force Equations.

It has now been shown that the simple electromagnetic force model overpredicts the actual armature force for the conventional, the transaugmented and the muzzle-fed railguns. Unlike the case for the 2-D railgun the error cannot be corrected by using the high frequency values of L' and M'. A modification is proposed to the simple force models to account for the fraction of total axial force that is exerted in the rails. This empirical modification is based on the simulations performed on the generic square bore railgun configurations.

A modification is first given for the conventional, muzzle-fed and transaugmented railguns with stationary armatures. This is done since the physics is much simpler for the stationary case and it is believed the results from the MEGA simulations for the stationary case are accurate to a few percent. Equation 1.1 provides a good estimate of the total axial force when appropriate values of L' are used, and it is a fraction of this force that accelerates the armature. In Figure 5.1 the armature force is relatively constant in time. This suggests multiplying Equation 1.1 by a constant parameter to find the true armature force [24],

$$F = \frac{1}{2} \alpha L' I^2 . \tag{5.1}$$

The value of α is then found to be 0.89 if the high frequency value of L', 0.51 μH/m, is used. Note that the conventional case does not coincide with the transaugmented and muzzle-fed railgun cases, since for the conventional simulations there was no outer rail present.

For the muzzle-fed and transaugmented railguns the modification,

$$F = \pm \frac{1}{2} \alpha L' I_1^2 + \beta M' I_1 I_2 , \tag{5.2}$$

is proposed, where the negative sign would be used for the muzzle-fed railgun and the positive sign for the transaugmented railgun. Note that in general, for the muzzle-fed railgun, the inner and outer rails could be powered separately as the rails were for the UTSI transaugmented railgun. The values of α and β are used here as constants and their values are found from the steady-state values of the armature force, obtained from computer simulations of the muzzle-fed and transaugmented railguns . This will produce some error for early time predictions of the armature force for the muzzle-fed case. The errors associated with using constant values of α and β are small due to the fact that the transient effects become small for the muzzle-fed railgun after about 0.2 ms, and the current level for a typical railgun is low during this time.

For the stationary case the values of α and β should be the same for both transaugmented and muzzle-fed configurations. The values for α and β are found from steady-state values of the armature force. At steady state the current distribution for the inner rail is the same for both the transaugmented and muzzle-fed railguns, except that one is being fed from the breech and the other from the muzzle. This suggest that the value of α should be the same for both configurations. The values of α and β were found from solving two equations, Equation 5.2 with a negative sign for the muzzle-fed railgun and positive sign for the transaugmented railgun, with the appropriate steady-state values of armature force in each equation. The steady-state transaugmented armature force was 4438 N and the muzzle-fed armature force was -170 N. The 10 kHz frequency values of L' and M', 0.49 and 0.31 μH/m respectively, were used. The solution yielded $\alpha = 0.94$ and $\beta = 0.69$. The value of α was essentially the same as that found from the conventional railgun with a stationary armature.

The values of α and β were determined from simulations where the inner and outer rail currents were 100 kA. For the modification to be of practical use, it must work for any combination of inner and outer rail currents. Simulations for the muzzle-fed and transaugmented railgun were performed with an inner rail current of 70 kA and an outer rail current of 140 kA. The steady-state transaugmented armature force was 3038 N and the muzzle-fed armature force was 972 N. Solving the two equations represented by Equation 5.2 with the 10 kHz values of L' and M', yielded $\alpha = 0.94$ and $\beta = 0.69$, identical to that found for $I_1 = I_2 = 100$ kA. The interpretation of these parameters is that α represents the fraction of force acting on the armature from the inner rails, and β represents the fraction of force acting on the armature from the outer rails. The values of α and β are valid up to current levels where the rail conductivity does not change drastically with the rail heating.

The physics is more complicated for the moving armature case. The problem is also complicated by the possible inaccuracy of MEGA for the moving armature case. Using MEGA results for the conventional railgun with a moving armature the value of α would be 1.01. Using MAP3 results the value of α would be 0.89. Since the actual MEGA formulation has been shown to be physically invalid and to yield inaccurate current distributions for the moving armature case, it is reasonable to use the MAP3 result instead of the MEGA result.

For the transaugmented and muzzle-fed configurations MAP3 results were not obtained and we must use the MEGA simulation results. The two equations represented by Equation 5.2 are used to find values for α and β. The equations are solved using the forces obtained at quasi-steady-state for the transaugmented and muzzle-fed railgun simulations. The term quasi-steady-state is used to describe the time at which the field reaches its full diffusion depth in the vicinity of the armature, since there is not a true steady-state condition for the velocity case. Doing this yields $\alpha = 0.93$ and $\beta = 0.77$. Once quasi-steady-state is reached the magnetic field produced by the outer rail becomes uniform in the axial direction. This axially uniform magnetic field is the same for both transaugmented and muzzle-fed railguns. This says that the only change in the integral of $\mathbf{J}_a \times \mathbf{B}_2$, where $\mathbf{B}_2$ is the magnetic field produced by the outer rail and $\mathbf{J}_a$ is the current density distribution in the armature, would have to come from variations of the current distribution in the xy-plane. This argument supports using the same value of β for both the transaugmented and muzzle-fed railguns.

Simulations for the muzzle-fed and transaugmented railgun were also performed using an inner rail current of 70 kA and an outer rail current of 140 kA. Solving the two equations represented by Equation 5.2 with the forces obtained at quasi-steady-state from the simulations, $\alpha = 0.92$ and $\beta = 0.73$ were obtained. These values are relatively close to those obtained for the inner and outer rail currents equal. This gives some confidence to the method used for obtaining the values of α and β.

A modification of the simple electromagnetic force model has been proposed for the conventional railgun, Equation 5.1, and the transaugmented and muzzle-fed railguns, Equation 5.2. A self consistent set of values for the parameters α and β were found for the stationary armature case. They were self consistent in that the values were consistent for the muzzle-fed and transaugmented configurations, for equal currents in each rail, as well as the case for $I_1 = 70$ kA and $I_2 = 140$ kA.

With armature motion a self consistent set of values for α and β were not found. By taking the forces obtained from transaugmented and muzzle-fed simulations at quasi-steady-state and substituting these values into the two equations represented by Equation 5.2, values for α and β are obtained. The values of α and β obtained for equal currents in each rail and for $I_1 = 70$ kA and $I_2 = 140$ kA were relatively close. Having β the same for both muzzle-fed and transaugmented simulations seems physically reasonable.

VI. ANALYSIS OF THE UTSI RAILGUN EXPERIMENTS USING THE MODIFIED ELECTROMAGNETIC FORCE MODEL.

A modification to the simple electromagnetic force model has been proposed. In this chapter the experiments presented in Chapter II for the muzzle-fed and transaugmented railguns are analyzed using this modification in the performance model presented in Chapter II. Values of α and β are obtained from 3-D MEGA simulations of the UTSI railgun geometry in transaugmented and muzzle-fed configurations.

6.1. Analysis of the UTSI Transaugmented Railgun Experiments.

A modification has been proposed for the simple electromagnetic force equation. For the conventional railgun Equation 1.1 was modified to,

$$F = \frac{1}{2}\,\alpha\, L'\, I^2\,. \tag{5.1}$$

For the muzzle-fed and transaugmented railguns the modification,

$$F = \pm\,\frac{1}{2}\,\alpha\, L'\, I_1^2 + \beta\, M'\, I_1\, I_2\,, \tag{5.2}$$

was proposed where the negative sign is used for the muzzle-fed railgun, and the positive sign for the transaugmented railgun.

Values of α and β were obtained from 3-D simulations of the actual UTSI railgun geometry. The boundary conditions, model length, armature length and material properties were identical to those used for the generic square bore railgun. Note that for the generic square bore railgun the conductivity was the same for both the rails and armature. As stated in Chapter IV this is because the formulation used in MEGA does not adequately handle a jump in conductivity. This is of importance since the UTSI railgun experiments were for a plasma armature, meaning the armature in the experiments had a conductivity approximately four orders of magnitude smaller than copper. It is believed by the author, however, that this does not significantly affect the fraction of force predicted by the simple force model exerted on the armature

The cross section was modified to account for the change in rail geometry and to alter the shape of the outer boundary. The outer boundary was adjusted to account for the aluminum structure that contains the bore. The aluminum structure was modeled in a 2-D simulation then replaced with a boundary that produced the same results for a current frequency of 10 kHz. At armature velocities over 1 km/s eddy currents would be produced in the aluminum structure similar to those produced by a current input frequency of 10 kHz. The cross section geometry is shown in Figure 6.1.

The transaugmented and muzzle-fed railguns were then simulated with fixed armature velocities of 2 and 1 km/s respectively. The simulations were performed with Helmholtz step current inputs of 100 kA in each set of rails. The armature force

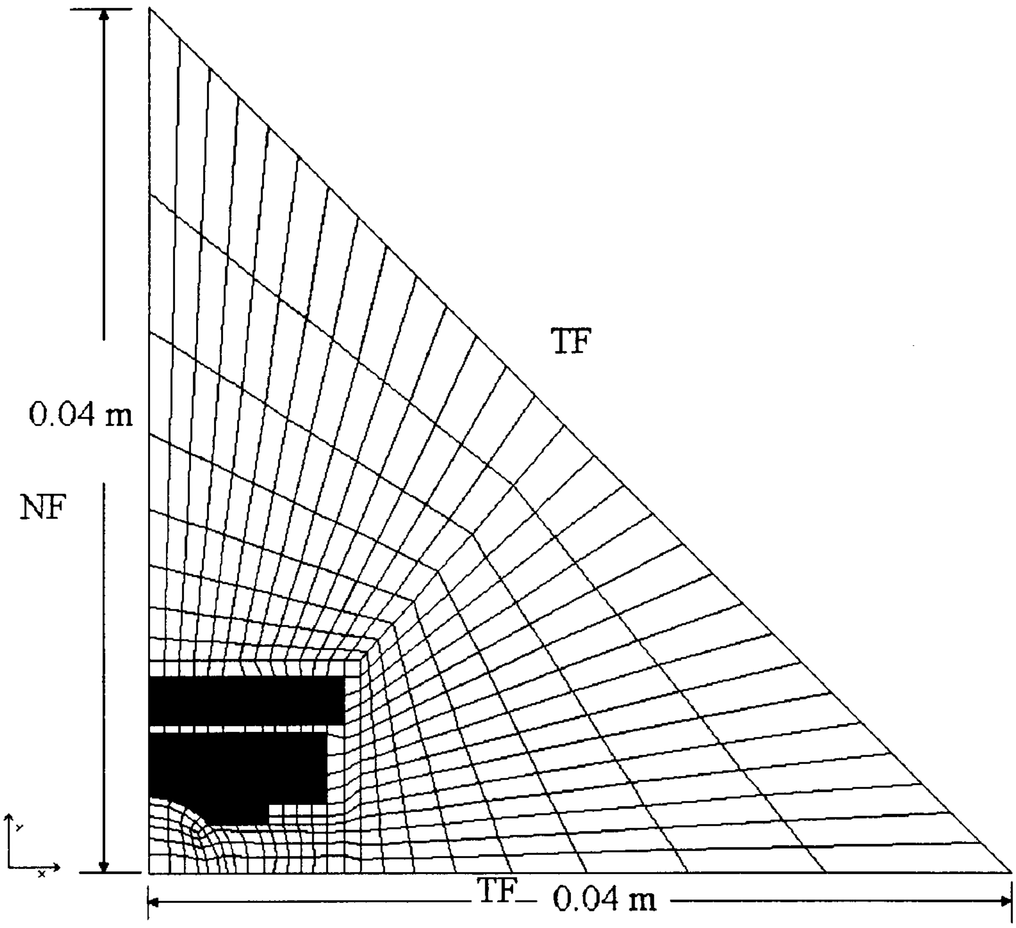

Figure 6.1. MEGA model of cross section of the UTSI transaugmented and muzzle-fed railgun.

at quasi-steady-state was 3065 N and 601 N for the transaugmented and muzzle-fed railgun respectively. The values of the inductance gradients at 10 kHz were $L' = 0.274\ \mu H/m$ and $M' = 0.249\ \mu H/m$. Note that for the UTSI railgun simulations and experiments the outer rail was present for all three configurations, so that L' was the same for the conventional, transaugmented and muzzle-fed railguns. Solving the two force equations represented by Equation 5.2 with their respective forces and the values of L' and M' at 10 kHz yielded $\alpha = 0.90$ and $\beta = 0.74$.

The question of what to do with the conventional railgun case now becomes of considerable importance. No matter what value of α one chooses the conventional baseline experiments can be fit since there are several drag parameters that can be varied. If these parameters are set using the value of $\alpha = 1.0$, as suggested by MEGA moving armature simulations, than the drag is too high in the augmented 70 kA series of shots to fit the experimental data. It was shown earlier in the 2-D railgun simulations that MAP3's predictions using its 3-D formulation were more accurate than MEGA's. It would seem reasonable, then, to use MAP3 instead of MEGA results. MAP3 could not be used directly to model the UTSI railgun geometry. For the generic square bore simulations MAP3 predicted essentially the same result in the steady state case for both moving and stationary armatures. A value of α approximately equal to 0.87 was found using the results of MEGA simulations of a conventional railgun with a stationary armature. The value of $\alpha = 0.90$ found from fitting the fixed armature velocity muzzle-fed and transaugmented railgun simulations will be used for consistency with those experiments.

Using the value of α = 0.90 in the performance model presented in Chapter II, drag parameters were found from the two baseline conventional railgun shots [9]. The performance model consisted of solving,

$$\frac{dv}{dt} = \left(\frac{1}{m_p + \alpha_a I V_a t}\right) \left(\left[\frac{1}{2} L' I_1^2 + M' I_1 I_2 \right] - \alpha_a I V_a v - \frac{C_f \alpha_a I V_a t v^2}{r} \right), \quad (1.5)$$

as a function of time along with Equation 2.2, the empirical formula for the total pressure due to the light gas gun and the fusing transient. The experimental current profiles, obtained from Rogowski coils used on each set of rails, were used in the performance model. In Equation 1.5 α_a is the ablation drag coefficient and C_f is the viscous drag coefficient. Equation 1.5 was discussed in the introductory section. The value of C_f = 0.001, the viscous drag coefficient, was used for both modified and unmodified simulations. This value was reported by Parker [2] and Hawke [3]. The ablation drag parameter was the only parameter changed. The value of 3.0e-9 kg/J was used in Chapter II. The ablation drag parameter used with the modified performance model was 1.0e-11 kg/J, essentially no ablation drag. The ablation drag parameter here represents the amount of ablated material that gets trapped in the armature, not the total amount of ablated material.

The two augmented series of shots were then simulated with the performance model using the new value of the ablation drag coefficient. In Figures 6.2a-d the experimental velocity profiles for the 70 kA series of transaugmented experiments are shown with the modified and unmodified performance model. The experimental

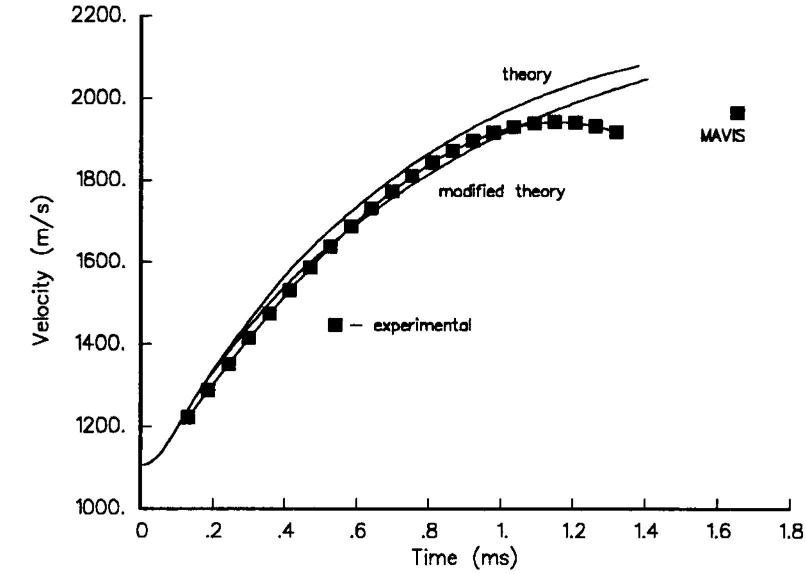

(a) I_1 = 70 kA, I_2 = 30 kA, shot 9/25.

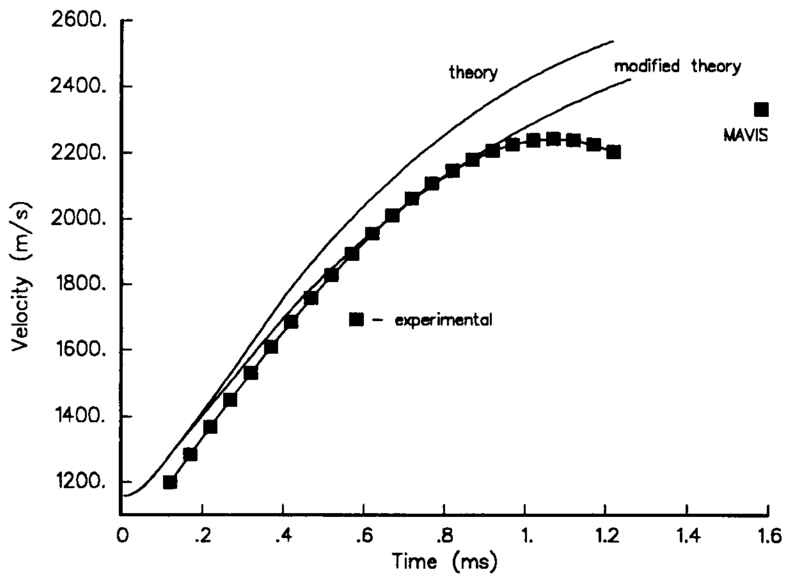

(b) I_1 = 70 kA, I_2 = 70 kA, shot 1/14.

Figure 6.2. Comparison of I_1 = 70 kA transaugmented experimental series velocity profiles with that predicted by the performance model using the unmodified and modified simple electromagnetic force equation.

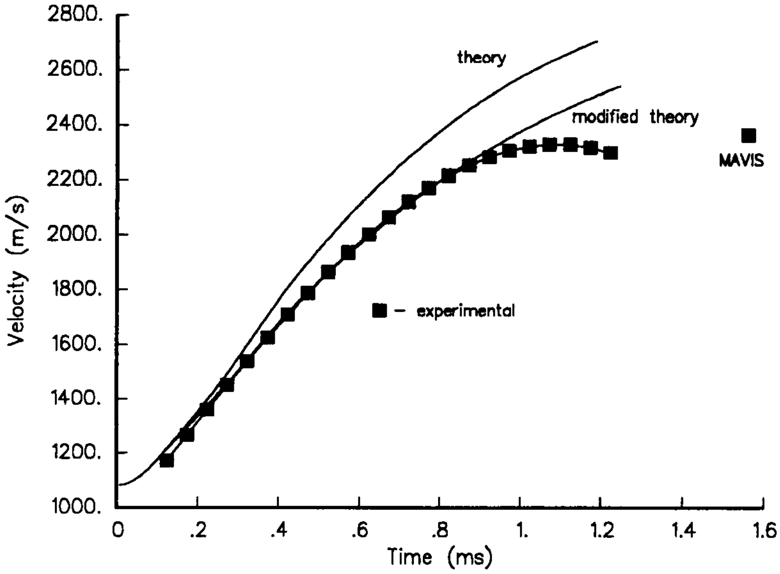

(c) I_1 = 70 kA, I_2 = 100 kA, shot 1/10.

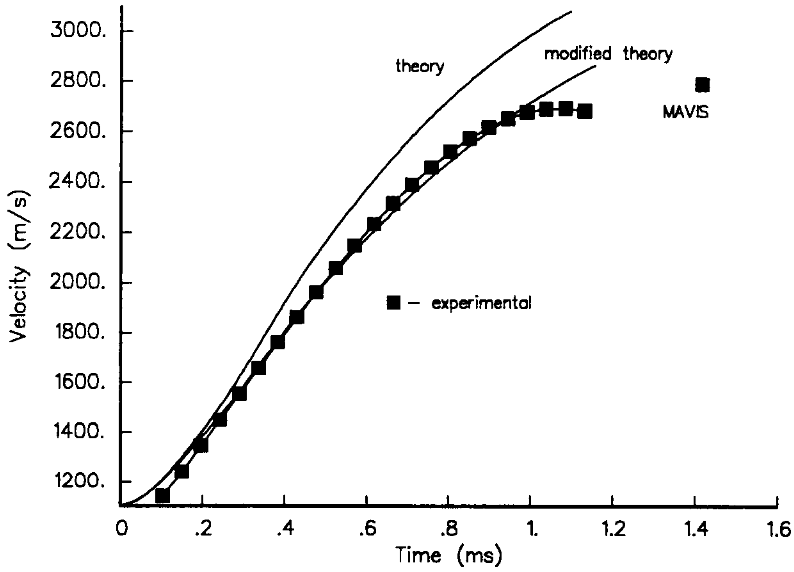

(d) I_1 = 70 kA, I_2 = 140 kA, shot 4/15.

Figure 6.2. Continued.

velocity profile was obtained by differentiating a fourth order curve fit to the armature position profile obtained from the rail B-dot probes. The shot numbers are referenced back to Table 2.1.

In Figure 6.2a there is little difference between the modified and unmodified predictions. This is because the level of augmentation is low, and the ablation parameter was set to fit the baseline, unaugmented shots for both the modified and unmodified case. Shot 1/16 was left out of this analysis since a secondary arc formed during this shot and the performance model does not account for this. Shot 4/15 was a repeat of shot 1/16 and is included in the analysis. With the modification to the simple electromagnetic equation, the performance model predicts the curve shape of the experimental data for the 70 kA series up to the point of primary separation.

Figures 6.3a-c shows the same analysis for the 100 kA series of transaugmented shots. The shot 7/10 shows the most significant deviation from the prediction made with the modified performance model. This was one of the first shots performed on the UTSI transaugmented railgun. It was done before the procedure of flushing the bore with acetone after lapping between each shot was introduced. Therefore, some anomalous behavior could be associated with this shot.

The failure of the modified performance model to predict the performance of shot 10/29 is the most disturbing result. Shot 10/29 had no secondary arc, a compact armature, and appeared to suffer little performance loss due to primary separation. The increase in ablation drag and armature mass needed to model correctly shot 10/29 was calculated to demonstrate the significance of the error in prediction for shot 10/29.

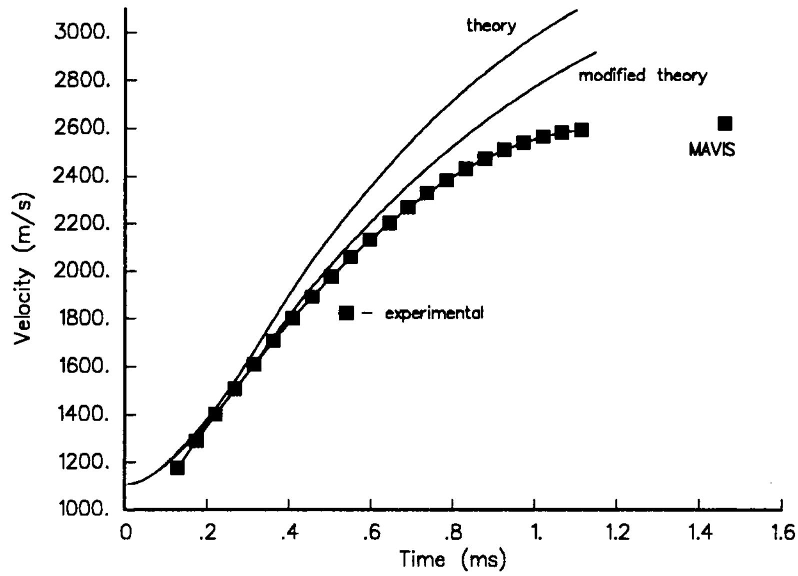

(a) I_1 = 100 kA, I_2 = 49 kA, shot 1/17.

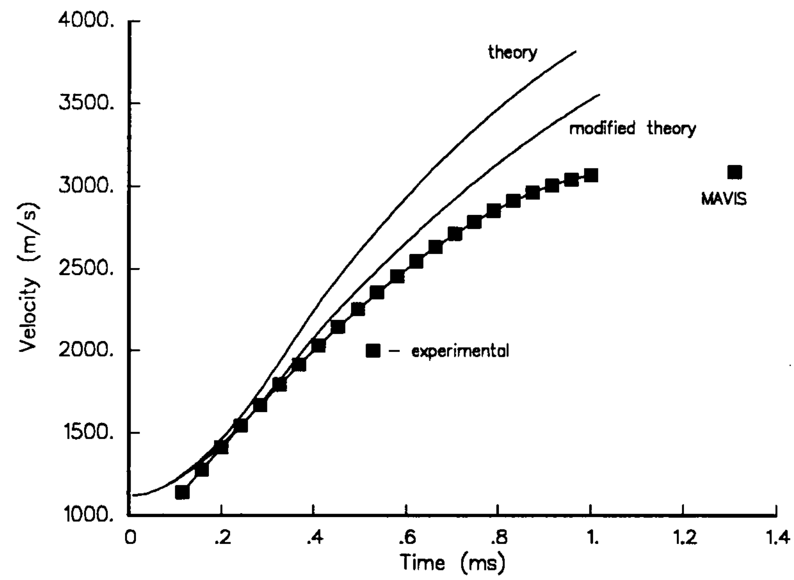

(b) I_1 = 100 kA, I_2 = 100 kA, shot 10/29.

Figure 6.3. Comparison of I_1 = 100 kA transaugmented experimental series velocity profiles with that predicted by the performance model using the unmodified and modified simple electromagnetic force equation.

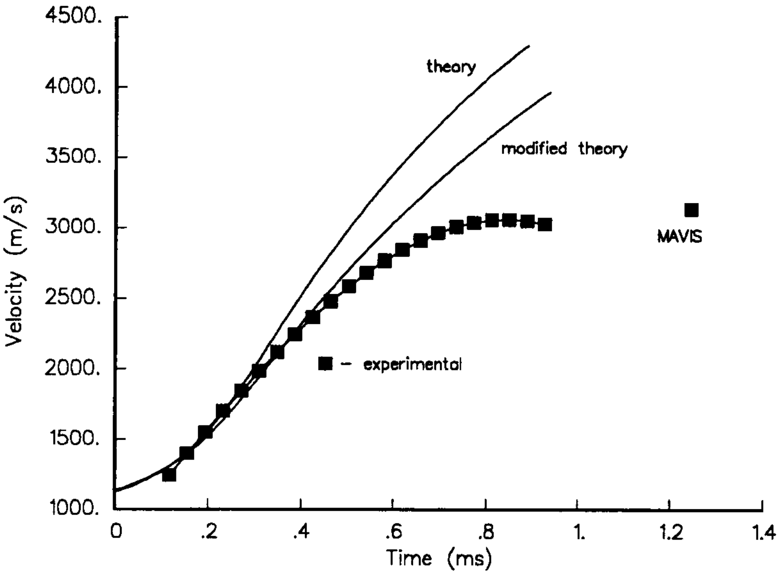

(c) I_1 = 100 kA, I_2 = 140 kA, shot 7/10.

Figure 6.3. Contiuned.

The armature mass was increased by an order of magnitude, 30 mg to 300 mg, and the ablation drag was increased from 1.0e-11 to 3.0e-9 kg/J. This is shown in Figure 6.4. These values of armature mass and ablation drag would produce a significant under-prediction of the experimental velocity profile for the baseline conventional shot.

Figure 6.5a summarizes the 70 kA series of transaugmented railgun experiments and their predictions. The 45 degree line in each plot represents the line for which the theoretical predictions match the experimental velocities. Figure 6.5a shows the significant improvement made by using the modified performance model on the 70 kA series. In Figures 6.1a-d the velocity predictions match the experimental profiles up to primary separation. The error that still remains is accounted for by the primary separation that was not included in the performance model.

Figure 6.5b summarizes the 100 kA series of transaugmented railgun experiments and their predictions. The modified performance model shows a considerable improvement over the old model, but there is still a significant error in the predictions. For the performance model to model shot 10/29 the armature mass would have to be increased by an order of magnitude and the ablation drag would have to be increased to 3.0e-7 kg/J. These parameters were found by "tweaking" parameter values in the model until a fit to the data was found. However, this "game" of "tweaking" the parameters can give some insight into what might be missing in the model.

It was primarily the increase in armature mass that gave the correct curve fit to the experimental data. The increased drag needed for the model to fit the

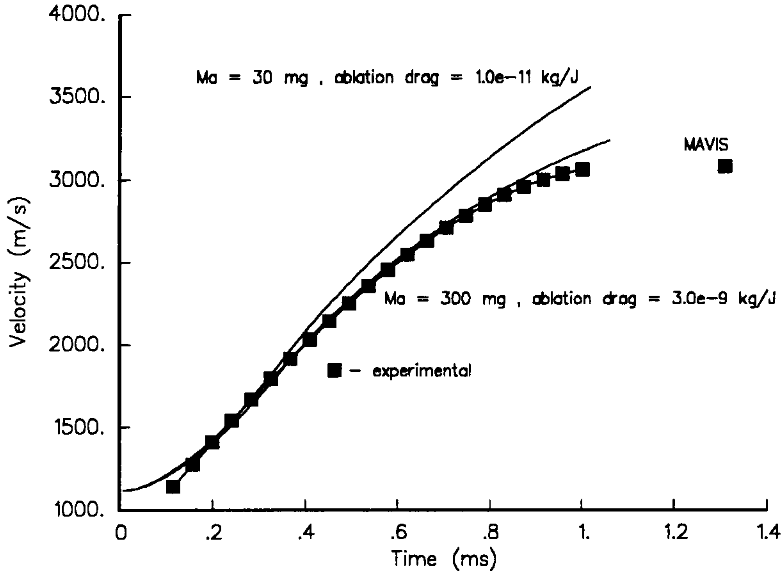

Figure 6.4. Modified perfomance model used to model shot 10/29 with increased armature mass and ablation drag coefficient.

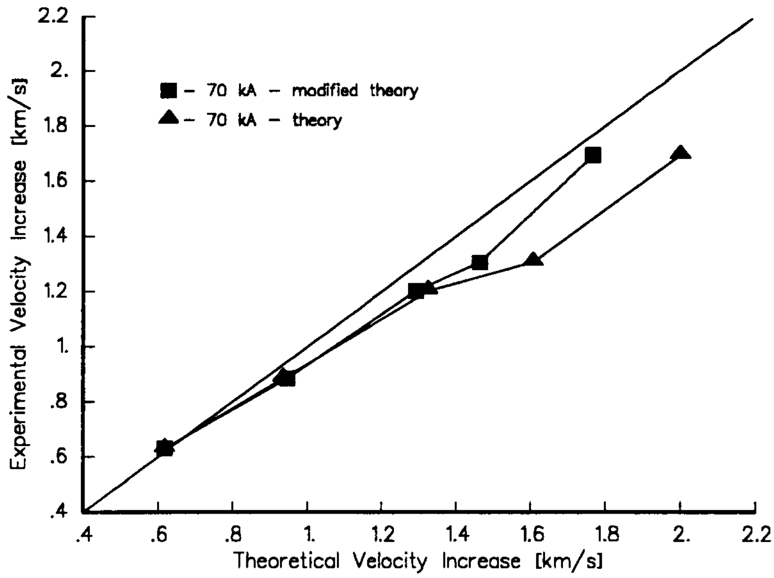

(a) 70 kA transaugmented series.

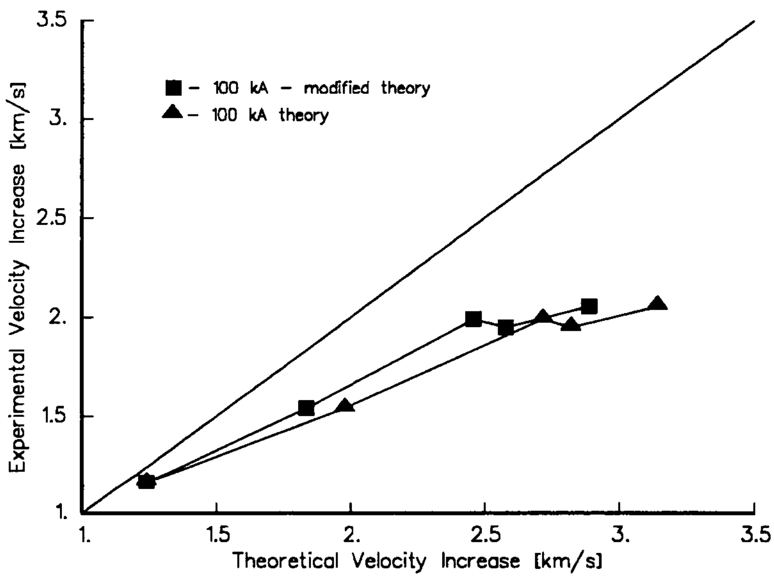

(b) 100 kA transaugmented series.

Figure 6.5. Experimentally observed velocity increase and perfomance model predictions using modified and unmodified simple electromagnetic force models.

experimental data was proportional to the square of the velocity not the velocity itself. This directly leads to the questioning of the viscous drag coefficient and the amount of mass that might be trapped in the cold zone between the projectile and armature. Further discussion of this is given in the conclusions section of Chapter VII.

6.2. Analysis of the UTSI Muzzle-Fed Railgun Experiments.

The same values of the parameters $\alpha = 0.90$ and $\beta = 0.74$ used to analyze the transaugmented railgun experiments were used to analyze the muzzle-fed railgun experiments. The performance model does not include effects associated with primary separation. Since all the muzzle-fed railgun shots experienced primary separation, Figures 2.4 and 2.5, the performance model did not work with the muzzle-fed railgun shots.

The unmodified and modified simple electromagnetic force equations, Equation 2.3 and 5.2 with the negative sign, were compared directly to experimental data to show the improvement made with the modification. A simulation using the actual experimental current profile was also performed to determine if dI/dt played a significant role in the armature force. Figure 6.6 shows the results of this comparison for $L'_{eff} = (M' - 0.5\ L')$ where $L' = 0.274$ and $M' = 0.249$ μH/m. The 0.54 factor for L'_{eff} comes from using α and β in the modified electromagnetic force equation. The MEGA simulation using the experimental current profile compared well with the modified force equation.

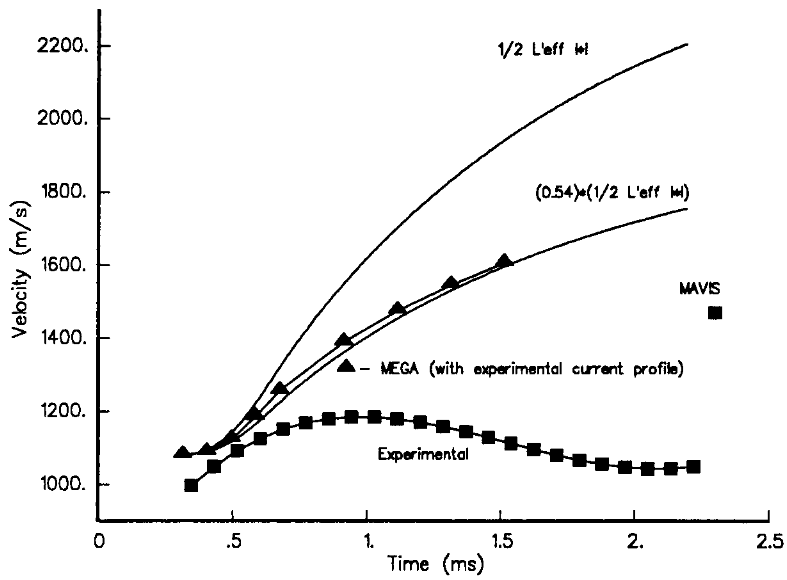

Figure 6.6. Comparison of experimental velocity with that predicted by the inductance gradients and MEGA for the muzzle-fed railgun.

For the comparison shown in Figure 6.6 the complete performance model was not used. At the current levels for which the muzzle-fed railgun shots were performed, the fusing transient was quite significant, and could have accounted for all the experimental projectile acceleration.

The modification to the simple electromagnetic force model did not predict the experimental results of the muzzle-fed railgun experiments. However, by identifying the inadequacy of the simple force model, a large fraction of the velocity deficit that might otherwise have been attributed to fluid mechanical drag effects has been accounted for. The explanation for the remaining experimental velocity deficit is most likely associated with primary separation [15].

VII. SUMMARY AND CONCLUSIONS.

7.1. Summary.

In Chapter II the question was asked "why question the simple electromagnetic force model?" This question was answered by examining the UTSI transaugmented and muzzle-fed railgun experiments, along with an examination of the derivation for the simple electromagnetic force equation. With both the transaugmented and muzzle-fed railgun experiments there was a failure of the performance model to predict experimental results. From the experiments it was argued that it was the electromagnetic force equation that was in error. An examination of the derivation of the simple electromagnetic force showed that the assumption that all the change in "associated energy" goes into mechanical work on the armature was invalid. Energy loss due to eddy current generation in the rails and strain energy from axial forces in the rails had been neglected.

Next the definitions for L' and M' were given, along with their dependencies on time, geometry and boundary distances. These quantities were discussed in some detail since they are central to the evaluation of the simple electromagnetic force equations. At early time, before the magnetic field diffuses into the rails, the inductance gradient is less than at late time when it has fully diffused. It was explained how this could be viewed in terms of losses due to eddy currents generated in the rails to exclude flux from the interior. Similarly, applying tangent flux boundary conditions to the outer boundaries of the model is the same as excluding flux from the exterior. This can again be viewed in terms of eddy current losses.

For a railgun, as the rails get thinner and farther apart, the inductance gradient increases. The UTSI "high" inductance railgun was designed using this simple understanding of the inductance gradient and MEGA to fine tune the design.

Simulations of a 2-D railgun were examined to give some initial insight into the simple electromagnetic force equation. It was found that,

$$F = \frac{1}{2} L' I^2 \ , \tag{1.1}$$

predicted the total axial force in the model. At early time, before any field diffused into the rails, Equation 1.1 predicted the true armature force. At late time, when the field had fully diffused into the rails, only a fraction of this force was exerted on the armature. The fraction of force exerted on the armature at late time decreased as the rail thickness increased.

2-D railgun simulations were then performed with the 3-D formulations of MEGA and MAP3. MEGA and MAP3 predicted very nearly the same armature force for both moving and stationary armatures. The current distribution for the 2-D railgun is known analytically [33]. Comparison of MEGA and MAP3's current distribution to the known analytic solution showed MEGA to have an anomalous current distribution for the moving armature case. It was also shown that MEGA's 3-D formulation was inadequate for models with non-uniform conductivities and/or with a moving armature. For both cases the current is not conserved.

Fully 3-D conventional, transaugmented and muzzle-fed railgun simulations were then performed on a generic square bore railgun. For the conventional railgun MEGA and MAP3 were used for both stationary and moving armature simulations. For the stationary armature MEGA and MAP3 gave very nearly the same results for armature force and total computational domain force. For the moving armature MEGA predicted an armature force 12% greater than MAP3. As with the 2-D railgun only a fraction of the force predicted by Equation 1.1 was exerted as armature force for both moving and non-moving armature simulations. This result suggested a modification to Equation 1.1 of,

$$F = \frac{1}{2} \alpha L' I^2 , \tag{5.1}$$

where α is the fraction of axial force predicted by Equation 1.1 exerted on the armature.

Transaugmented generic square bore simulations were then performed. For these simulations an even smaller fraction of the force predicted by the simple electromagnetic force model was exerted on the armature. Since the magnetic field produced by the outer rail diffuses into the inner rail before the arrival of the armature, it interacts more with the transverse component of **J** in the rails, resulting in a larger axial force in the rails.

The muzzle-fed railgun offered the most conclusive evidence that the simple electromagnetic force model is inadequate even for baseline railgun firings. The force predicted by the simple electromagnetic model was actually of the wrong sign for the generic square bore simulation of the muzzle-fed railgun. This result showed that the simple electromagnetic force model could not be used to predict the performance of a muzzle-fed railgun.

A modification to the simple models for the transaugmented and muzzle-fed railgun was proposed,

$$F = \pm \frac{1}{2} \alpha L' I_1^2 + \beta M' I_1 I_2 , \tag{5.2}$$

where β represented the fraction of axial force produced by the outer rail that acts on the armature. Values of the parameters α and β were found that fit the steady state force predictions for all three configurations with a stationary armature. The parameters were originally found for equal inner and outer rail currents. The values of α and β were shown to be consistent when the inner and outer rail currents were not equal.

A self consistent set of values was not found for α and β for the moving armature case. Solving for α and β using the quasi-steady-state values of the armature force for the transaugmented and muzzle-fed with inner and outer rail currents equal produced one set of values for α and β. At quasi-steady-state the magnetic field produced by the outer rail is uniform in the axial direction. For β to be significantly different for the muzzle-fed and transaugmented railguns, the armature current distribution in the xy-plane of the two railguns would have to be significantly different. Simulations for the transaugmented and muzzle-fed railgun with I_1 = 70 kA and I_2 = 140 kA produced values of α and β relatively close to those found when the rail currents were equal. Until more accurate simulations are done, using the same value of β for each railgun seems physically reasonable.

The modified force model was evaluated by comparison to the UTSI transaugmented and muzzle-fed railgun experiments. MEGA simulations using the UTSI cross section geometry with a moving armature were performed. The simulations used a uniform conductivity of copper in the rails and armature. This was done since MEGA does not adequately handle the case of non-uniform conductivity. The field diffusion through the armature in the model is significantly different than in the plasma armatures used in the experiments. It is believed by the author, however, that this has little effect on the parameters α and β. MAP3 simulations support this believe. MAP3 predicted essentially the same armature force for both the stationary and moving armature case in a conventional railgun. This was true even though the moving armature simulation produced a significantly different current distribution in the rail than did the stationary armature simulation.

The quasi-steady-state values of the force for each railgun were used to find values of α and β. This modification was used in the performance model to re-evaluate the UTSI transaugmented experiments. The performance model was in good agreement with the 70 kA series of experiments. The performance model was unable to predict the 100 kA experimental results. An order of magnitude increase in armature mass used in the performance model was required to explain the deviation of the performance model from the experiments. This has implications that are discussed in the conclusions section.

In the muzzle-fed experiments the armature separated from the projectile near the point of fusing. Primary separation is not yet fully understood, and the performance model does not include this effect. For these reasons it was not possible to determine if the modification in the simple electromagnetic force model worked for these experiments. The modification did account for nearly a 50% reduction of armature force predicted by the simple electromagnetic force model. This accounted for a large fraction of the velocity deficit that might have otherwise been attributed to fluid mechanical drag effects.

7.2. Conclusions.

The 3-D MEGA and MAP3 simulations have shown that the simple electromagnetic force model is inadequate when used to predict the axial armature force. Early researchers picked the smallest possible value of L' to use for experimental performance evaluation. This gave the correct armature force for the conventional railgun, but the correct procedure would be to find the fraction of the force predicted by the simple force model that goes into axial armature force by using 3-D railgun simulations. The fraction is expressed as a value of α in Equation 5.1.

It was shown with the 3-D muzzle-fed railgun simulations that picking the smallest values of L' and M' does not always work. (I.e. using the high frequency values of L' and M' in the simple electromagnetic force model for the muzzle-fed case results in an even larger deviation from the true armature force.) To determine the electromagnetic armature force 3-D electromagnetic simulations must be done!

It is not feasible to perform a 3-D simulation for every experiment, if many experiments at numerous current levels need to be evaluated. For this reason a modification to the simple force model for the conventional, transaugmented and muzzle-fed configurations was proposed. It was proposed that the values of α and β be found from the armature force at quasi-steady-state for the transaugmented and muzzle-fed simulations with a moving armature. In Figure 6.6 it was shown that the armature force using these parameters closely approximated the actual time-dependent armature force found from the 3-D simulation. The values of α and β are valid up to current levels where the rail conductivity does not change drastically with the rail heating.

Agreement between the performance model and the experimental data was improved with the use of the modified electromagnetic force model. However, it was still not possible to match the experimental data from the transaugmented railgun 100 kA series of shots. This leads to the conclusion that some additional fluid-dynamic effects (or effect) have been unaccounted for in the performance model. The increased drag needed for the model to fit the experimental data was proportional to the square of the velocity. This leads to questioning of the viscous drag coefficient and the amount of mass that might be trapped in the currentless buffer zone between the projectile and armature.

In the UTSI transaugmented railgun experiments the armature stayed compact throughout the drive, but it does not seem reasonable that it operated in the current sheath (CS) mode discussed in Chapter I. The armature seemed to operate in a stable plasma dynamic discharge (PDD) mode. It did not produce a secondary or expand considerably which is typical of the instabilities discussed by the Russian authors. A currentless buffer zone was discussed in Chapter I and this existed on all the UTSI railgun shots. Near the end of each shot the armature separated from the projectile indicating that this buffer zone expanded near muzzle exit.

As was pointed out in Chapter VI an increase in armature mass was needed to fit the 100 kA series of shots. The mass in the buffer zone is "cold" so that the material in this region is dense. An increase in the size of the buffer zone could produce an appreciable increase in the total mass that is accelerated by the armature. This could account for the further decrease in performance observed in the experiments.

The viscous drag coefficient is not well known for the plasma conditions in a railgun. The 3-D MHD simulations performed by Kondrashov and Keefer showed that the plasma flow near the insulator surface was in the direction of armature motion [36]. This is in the opposite direction of typical flow in a pipe and was due to the strong **JxB** force near the insulator surface. This increase in the velocity gradient from the flow to the rail surface could yield a larger value of C_f than was used here for railgun performance evaluation. Since the velocity of the flow next to the rail surface could conceivably increase with increased rail current, this could explain why it was not possible to fit the 100 kA series of transaugmented shots.

BIBLIOGRAPHY

BIBLIOGRAPHY

[1] S. C. Rashleigh and R. A. Marshall, "Electromagnetic Acceleration of Macroparticles to High Velocity," J. Appl. Phys., Vol 49, pp. 2540-2542, April 1978.

[2] J. V. Parker, "Why Plasma Armature Railguns Don't Work (And What Can Be Done About It)," IEEE Trans. on Magn., vol. 25, no. 1, pp. 418-424, Jan. 1989.

[3] R. S. Hawke, W.J. Nellis, G. H. Newman, J. Rego and A. R. Susoeff, "Summary of EM Launcher Experiments Performed at LLNL," IEEE Trans. Mag., MAG-22 (6), pp. 1510-1515, 1986.

[4] J. V. Parker, W. M. Parsons, C. E. Cummings and W. E. Fox, "Performance Loss Due to Wall Ablation in Plasma Armature Railguns," Conference Title: AIAA 18th Fluid Dynamics and Plasma Dynamics and Lasers Conference, pp. 1-9, July 1985.

[5] R.F. Askew, B.A. Chin, B.J. Tatarchuk, J.L. Brown, and D.B. Jensen, "Rail and Insulator Erosion in Rail Guns," IEEE Trans. Mag., MAG-22 (6), pp. 1380-1385, November 1986.

[6] L. E. Thurmond, B. K. Ahrens, and J. P. Barber, "Measurements of the Velocity Skin Effect," IEEE Trans. Mag., Vol. 27, No. 1, pp. 326-328, January 1991.

[7] F. Stefani, M. B. Schulman, R. E. Wootton, D. A. Fikse, "Zero-Ablation Tests on the HART Augmented Launcher," IEEE Trans. Mag., Vol 29, No. 1, pp. 1207-1212, Jan. 1993.

[8] M. B. Schulman, R. E. Wootton, F. Stefani, D. A. Fikse, E. F. Docherty, and V. F. DeMarchi, "HART Hypervelocity Augmented Railgun Test Facility," IEEE Trans. Mag., Vol 29, No. 1, pp. 505-510, Jan. 1993.

[9] J. Taylor, R. Crawford, and D. Keefer, "Experimental Comparison of Conventional and Trans-augmented Railguns," IEEE Trans. on Magn., vol. 29, no. 1, pp. 523-529, Jan. 1993.

[10] A. Yamori, N. Kawashima, and M. Kohno, "Characteristics of High Efficiency 300 kJ Railgun," IEEE Trans. Mag., Vol. 31, No. 1, pp. 377-381, January 1995.

[11] J. V. Parker, J. H. Batteh, J. R. Greig, D. Keefer, I. R. McNab, and Z. Zabar. "Non-US Electrodynamic Launchers Research and Development," FASAC Technical Assessment Report (November 1994).

[12] V. B. Zheleznyi, M. F. Zhukov, A. D. Ledebev, and A. V. Plekhanov, "The Effect of the Initial Dynamics of the Formation of a Plasma Conductor on the Efficiency of an Electrodynamic Accelerator," Sov. Phys.-Tech. Phys., 37, pp. 303-308, March 1992.

[13] V. E. Ostashev, E. F. Lebedev, and V. E. Fortov, "The Problems of Realization of Electrodynamic Acceleration Regime in Railgun with Plasma Armature," Megagauss VI: Oral Session OH-Launchers, 11 Nov. 1992, Albuquerque, NM.

[14] E. M. Drobyshevski, S. I. Rozov, B. G. Zhukov, R. O. Kurakin, and V. M. Sokolov, "Experiments on Simple Railgun with Compacted Plasma Armature", IEEE Trans. Mag., Vol. 31, No. 1, pp. 251-298, January 1995.

[15] D. Keefer, J. Taylor and R. Crawford, "The Electromagnetic Force in Railguns," Fourth European Symposium on Electromagnetic Launch Technology, May 2-6, 1993, Celle, Germany.

[16] J. V. Parker, "Magnetic-Probe Diagnostics for Railgun Plasma Armatures," IEEE Trans. on Plasma Science, vol.17, no. 3, pp. 487-500, June 1989

[17] Allen R. Susoeff, Personal Document With Sketches of Magnetic Induction Device, Nuclear Explosives Engineering Div., Lawrence Livermore Laboratory, October 1990.

[18] D. Rodger and P. J. Leonard, "Modelling the Electromagnetic Performance of Moving Railgun Launchers Using Finite Elements", IEEE Trans. Mag., Vol 29, No. 1, pp. 496-498, Jan. 1993.

[19] G. E. Rolader and J. H. Batteh, "Effects of In-Bore Gas on Railgun Performance," IEEE Trans. on Magn., Vol. 27, No. 1, pp. 120-125, Jan. 1991.

[20] J. Taylor, R. Crawford, and D. Keefer, "Muzzle-Fed Railgun Experiments with 3-D Electromagnetic Simulations," IEEE Trans. Mag., Vol. 31, No. 1, pp. 360-364, January 1995.

[21] L. M. Smith, Assistant Professor of Electrical Engineering, The University of Tennessee Space Institute, private communications.

[22] H. A. Calvin, "The Railgun Force in the Presence of Secondary Arcs," IEEE Trans. on Magn., Vol. 27, No. 1, pp. 116-119, Jan. 1991.

[23] P. Lorrain and D. Corson. Electromagnetic Fields and Waves. Second Edition. San Francisco: W. H. Freeman and Company, p. 365, 379, 1970.

[24] D. R. Sagedin and W. J. Bonwick, "The Railgun and its Power Source," Department of Defense Materials Research Laboratories report MRL-R-1058, Commonwealth of Australia 1987.

[25] J. Taylor, "A Study of the UTSI Transaugmented and Classical Railgun," UTSI Thesis, December 1991.

[26] W. Panofsky and M. Phillips. Classical Electricity and Magnetism. Second Printing. Massachusetts: Addison-Wesley Publishing Company, Inc. p. 156, 1956.

[27] F. E. Terman. Radio Engineers Handbook. New York: McGraw-Hill, 1943, p. 47 ff.

[28] J. N. Reddy. An Introduction to the Finite Element Method. Second Edition. McGraw-Hill, Inc. 1993.

[29] K. R. Crandall, "Computation of Charge Distribution on or Near Equipotential Surfaces," Los Alamos Scientific Laboratory report LA-3512 (December 1966).

[30] J. F. Kerrisk, "Current Distribution and Inductance Calculations for Rail-Gun Conductors," Los Alamos Scientific Laboratory report LA-9092-MS (November 1981).

[31] D. Kondrashov, Graduate Research Assistant, The University of Tennessee Space Institute, private communications.

[32] J. A. Stratton, Electromagnetic Theory. McGraw-Hill, Inc. p. 103, 1941.

[33] G. C. Long, "Railgun Current Density Distributions," IEEE Trans. Mag., MAG-22 (6), pp. 1597-1601, 1986.

[34] J. D. Jackson, Classical Electrodynamics. Second Edition. John Wiley & Sons, p. 219, 1975.

[35] D. Rodger, "Finite-Element Method for Calculating Power Frequency 3-D Electromagnetic Field Distributions," IEE Proceedings., Vol 130, No. 5, pp. 233-238.

[36] D. Kondrashov and D. Keefer, "3-D Plasma Armature Railgun Simulations," IEEE Trans. Mag., Vol. 31, No. 1, pp. 634-639, January 1995.

APPENDICES

APPENDIX A

SIMPLE ELECTROMAGNETIC FORCE MODELS FOR THE TRANSAUGMENTED AND MUZZLE-FED RAILGUNS

In Section 2.3.2 the simple electromagnetic force equation for the conventional railgun was derived using the conservation of power at the breech of the railgun. The simple electromagnetic force equations for the transaugmented and muzzle-fed railgun, given in Equations 1.6 and 2.3 respectively, are now derived using this same method.

Before deriving the equations one first needs to express the energy stored in the magnetic field and the potential drop across the circuit in terms of the inductances. For a conventional railgun the energy stored in the magnetic field is defined as W_f = 1/2 $L' I^2$. This is a standard definition for L, the self-inductance of a circuit. For a transaugmented railgun the energy stored in the magnetic field is given by,

$$W_f = \frac{1}{2} L_1 I_1^2 + \frac{1}{2} L_2 I_2^2 + M I_1 I_2 \ . \tag{A.1}$$

where L_2 is the self inductance of the outer rails and M is the mutual inductance between the inner and outer rails. This expression can serve as a definition for M, although M is usually defined in terms of the magnetic flux linking two circuits [23].

The potential drop in the circuit consists of two parts. One part is due to the resistivity of the rails and is given by Ohms law. The other is the induced electromotance of the circuit and is obtained by taking the integral of the differential form of Faraday's induction law. The differential form of Faraday's induction law is,

$$\nabla \times \mathbf{E} = -\frac{\partial \mathbf{B}}{\partial t}. \tag{4.11}$$

Taking the surface integral of Equation 4.11 and applying Stokes Theorem to convert the left side to a line integral, the induced electromotance is,

$$\oint \mathbf{E} \cdot \mathbf{dl} = -\frac{d\Phi}{dt}, \tag{A.2}$$

where Φ is the magnetic flux and is given by,

$$\Phi = \int_S \mathbf{B} \cdot \mathbf{da}. \tag{A.3}$$

The magnetic flux for the transaugmented railgun, expressed in terms of L_1 , L_2 and M is,

$$\Phi = \Phi_1 + \Phi_2 = (L_1 I_1 + M I_2) + (L_2 I_2 + M I_1), \tag{A.4}$$

where Φ_1 and Φ_2 are the magnetic fluxes associated with the inner and outer rails respectively. Note that Φ_1 is dependent upon I_2 through the mutual inductance and Φ_2 is dependent upon I_1 through the mutual inductance.

The simple electromagnetic force is obtained by conserving power at the breech of the railgun. The power input to the breech is the input current of each rail times the associated potential drop of each rail,

$$P = I_1 \left(\frac{d\Phi_1}{dt} + I_1 R_1 \right) + I_2 \left(\frac{d\Phi_2}{dt} + I_2 R_2 \right). \tag{A.5}$$

Substituting the derivatives with respect to time of Φ_1 and Φ_2 into Equation A.5 yields,

$$P = I_1 \left(I_1 \frac{dL_1}{dt} + L_1 \frac{dI_1}{dt} + I_2 \frac{dM}{dt} + M \frac{dI_2}{dt} \right) + I_2 \left(I_1 \frac{dM}{dt} + M \frac{dI_1}{dt} + L_2 \frac{dI_2}{dt} \right) \tag{A.6}$$
$$+ I_2^2 R_2 + I_1^2 R_1 .$$

In Equation A.6 it was assumed that L_2 is a constant, which neglects the effects of field diffusion into the outer rail.

The power associated with the change in magnetic field energy is obtained by taking the derivative with respect to time of Equation A.1. Again assuming that L_2 is constant,

$$\frac{dW_f}{dt} = \frac{1}{2} I_1^2 \frac{dL_1}{dt} + L_1 I_1 \frac{dI_1}{dt} + L_2 I_2 \frac{dI_2}{dt} + M I_1 \frac{dI_2}{dt} + M I_2 \frac{dI_1}{dt} + I_1 I_2 \frac{dM}{dt} . \tag{A.7}$$

Subtracting the ohmic heating terms and the change in magnetic field energy, given by Equation A.7, from Equation A.6 yields,

$$\frac{dW_a}{dt} = \frac{1}{2} I_1^2 \frac{dL}{dt} + I_1 I_2 \frac{dM}{dt} , \tag{A.8}$$

where W_a is the "associated energy" [24]. The same inadequate assumption, as was made for the conventional railgun, that the change in inductances can be written as $L'v$ and $M'v$ yields,

$$\frac{dW_a}{dt} = \frac{1}{2} I_1^2 L' v + I_1 I_2 M' v , \tag{A.9}$$

where L' is the inductance gradient of the inner rail. All the change in energy given by Equation A.9 is assumed to go into mechanical work. This assumption is wrong, as it was for the conventional railgun. Since mechanical power is equal to force times velocity, if we divide both sides of Equation A.9 by velocity we obtain,

$$F = \frac{1}{2} L' I_1^2 + M' I_1 I_2 \ . \tag{1.6}$$

The derivation for the muzzle-fed railgun is not only similar, but involves all the same terms with a few having a different sign. This is because there is still an inner and an outer rail and the coupling between the rails is the same, thus one has all the same terms. However, the current in the inner rail is in the opposite direction, thus the sign of I_1 must be changed. Changing the sign of I_1 in Equations A.6 and A.7, and again subtracting the ohmic heating terms and the change in magnetic field energy, given by Equation A.7, from Equation A.6 yields,

$$\frac{dW_a}{dt} = \frac{1}{2} I_1^2 \frac{dL}{dt} - I_1 I_2 \frac{dM}{dt} \ . \tag{A.10}$$

Assuming that the change in inductances can be written as $L'v$ and $M'v$, and assuming that all the change in energy goes into mechanical work, one obtains,

$$F = \frac{1}{2} L' I_1^2 - M' I_1 I_2 \ . \tag{A.11}$$

If instead of choosing I_1 to be of negative sign, one had chosen I_2 to be of negative sign, then one would have ended up with the same equation. This is because Equation A.11 represents the magnitude of the force but does not specify the direction of the force.

For the muzzle-fed railgun the magnitude of I_1 and I_2 are the same. Substituting I for I_1 and I_2 in Equation A.11 and rearranging terms yields,

$$F = \frac{1}{2} M' I^2 + \frac{1}{2} (M' - L') I^2 . \tag{2.3}$$

Equation 2.3 represents the armature force in the direction from breech to muzzle. The first term represents the force supplied by the magnetic field behind the armature. The second term represents the force supplied by the magnetic field in front of the armature. L' is always greater than M', so the second term will always be negative. As the value of M' approaches that of L', Equation 2.3 approaches,

$$F = \frac{1}{2} L' I^2 . \tag{1.1}$$

The simple electromagnetic force equations for the transaugmented railgun and muzzle-fed railguns have been derived using the conservation of power at the breech. The assumptions are equivalent to those made for a conventional railgun in Section 2.3.2. The assumptions are again invalid for the same reasons given in Section 2.3.3.

APPENDIX B

THE GENERIC SQUARE BORE RAILGUN GRID

The same grid was used for the 3-D generic square bore conventional, transaugmented and muzzle-fed railgun simulations. The grid was the same for both MEGA and MAP3 simulations of the conventional railgun. A slice of this grid in the yz-plane was used for the 2-D railgun simulations with the 3-D formulations of MEGA and MAP3.

The grid was chosen for its simplicity, only rectangular elements were used, and to resolve the high current densities at the rear of the armature for the moving armature case. Since the grid is simple and has been used for simulations with two different 3-D electromagnetic codes, it would serve as an ideal test case for other 3-D electromagnetic codes. For this reason the geometry used in the simulations and the nodal coordinates are presented here.

The geometry of the generic square bore model is given in Figures B.1 and B.2. These Figures give all necessary dimensions. For the conventional railgun the outer rail was modeled as air. The boundary conditions applied to the problems were presented in Chapter V.

Table B.1 gives the coordinates x, y, z for all nodes. These numbers are not nice round numbers since an attempt was made to make this an efficient grid.

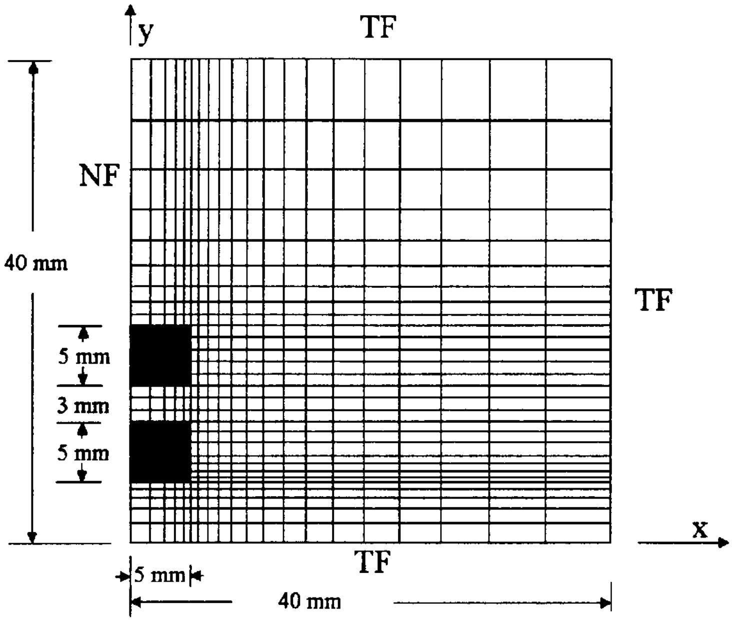

Figure B.1. Cross section (xy-plane) of generic square bore model.

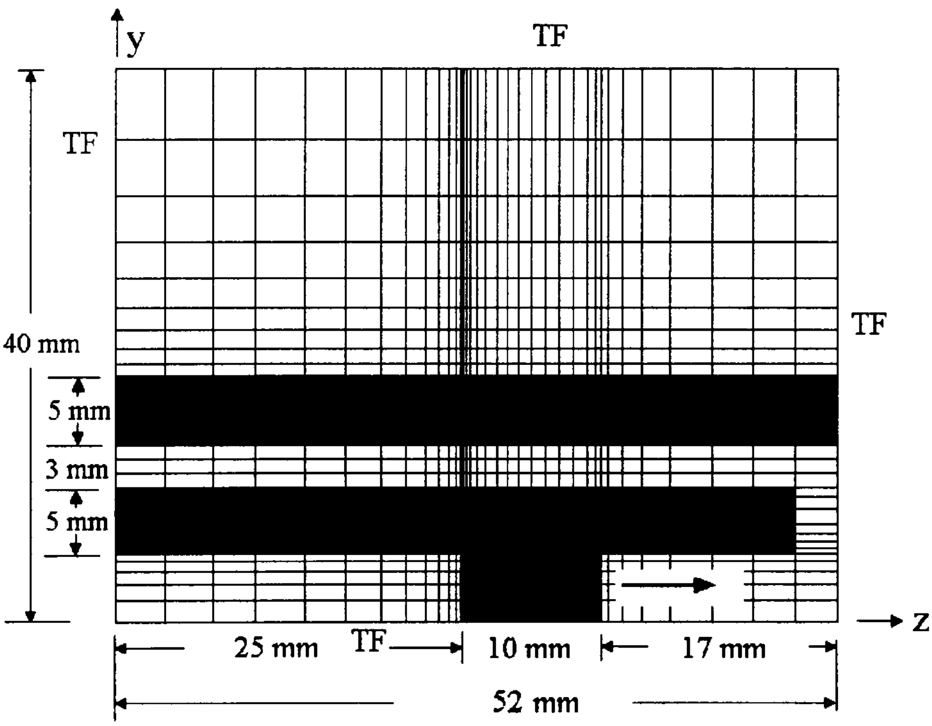

Figure B.2. Grid for generic square bore model in the yz-plane.

Table B.1. Nodal coordinates for generic square bore railgun.

#	x	y	z	#	x	y	z
1	0.0	0.0	0.0	20	3.4586e-2	1.7000e-2	2.82e-2
2	1.6081e-3	1.6081e-3	3.5e-3	21	4.0e-2	1.8000e-2	2.90e-2
3	2.8300e-3	2.8300e-3	7.0e-3	22		1.8849e-2	3.00e-2
4	3.7585e-3	3.7585e-3	1.0e-2	23		1.9911e-2	3.10e-2
5	4.4640e-3	4.4640e-3	1.35e-2	24		2.1239e-2	3.20e-2
6	5.0000e-3	5.0000e-3	1.65e-2	25		2.2901e-2	3.30e-2
7	5.6768e-3	5.4314e-3	1.91e-2	26		2.4981e-2	3.40e-2
8	6.4620e-3	5.9339e-3	2.09e-2	27		2.7582e-2	3.46e-2
9	7.3728e-3	6.5193e-3	2.23e-2	28		3.0836e-2	3.50e-2
10	8.4296e-3	7.2014e-3	2.32e-2	29		3.4907e-2	3.55e-2
11	9.6556e-3	8.3284e-3	2.40e-2	30		4.0000e-2	3.65e-2
12	1.1078e-2	9.2486e-3	2.45e-2	31			3.80e-2
13	1.2728e-2	1.0000e-2	2.48e-2	32			4.00e-2
14	1.4642e-2	1.1000e-2	2.50e-2	33			4.30e-2
15	1.6863e-2	1.2000e-2	2.52e-2	34			4.60e-2
16	1.9439e-2	1.3000e-2	2.55e-2	35			4.90e-2
17	2.2428e-2	1.4000e-2	2.60e-2	36			5.20e-2
18	2.5896e-2	1.5000e-2	2.66e-2	37			
19	2.9919e-2	1.6000e-2	2.74e-2				

VITA

Jaime R. Taylor was born in Rota Naval Base, Spain, on April 12, 1966. He graduated from Montgomery Central high school in Clarksville, TN in 1984. He then went to Nashville State Technical Institute receiving his Associate Degree in Industrial Engineering Technology in 1986.

While working part-time in statistical process control at International Label Company from 1986 to 1990 he attended Austin Peay State University where he obtained a Bachelor of Science in Physics and Mathematics with a minor in Chemistry. He then enrolled as a full-time student at the University of Tennessee Space Institute (UTSI) where he worked as a graduate research assistant. He received his Masters of Science degree in Engineering Science in December of 1991.

Continuing his studies at UTSI he received his Doctor of Philosophy degree with a major in Engineering Science in May of 1995.

Jaime R. Taylor and his wife, Stacy, reside in Hillsboro, TN with their two children Makenzie and Jordan.